Flow structure detection using a numerical lidar measurement model

M.N.X.Y Pellé

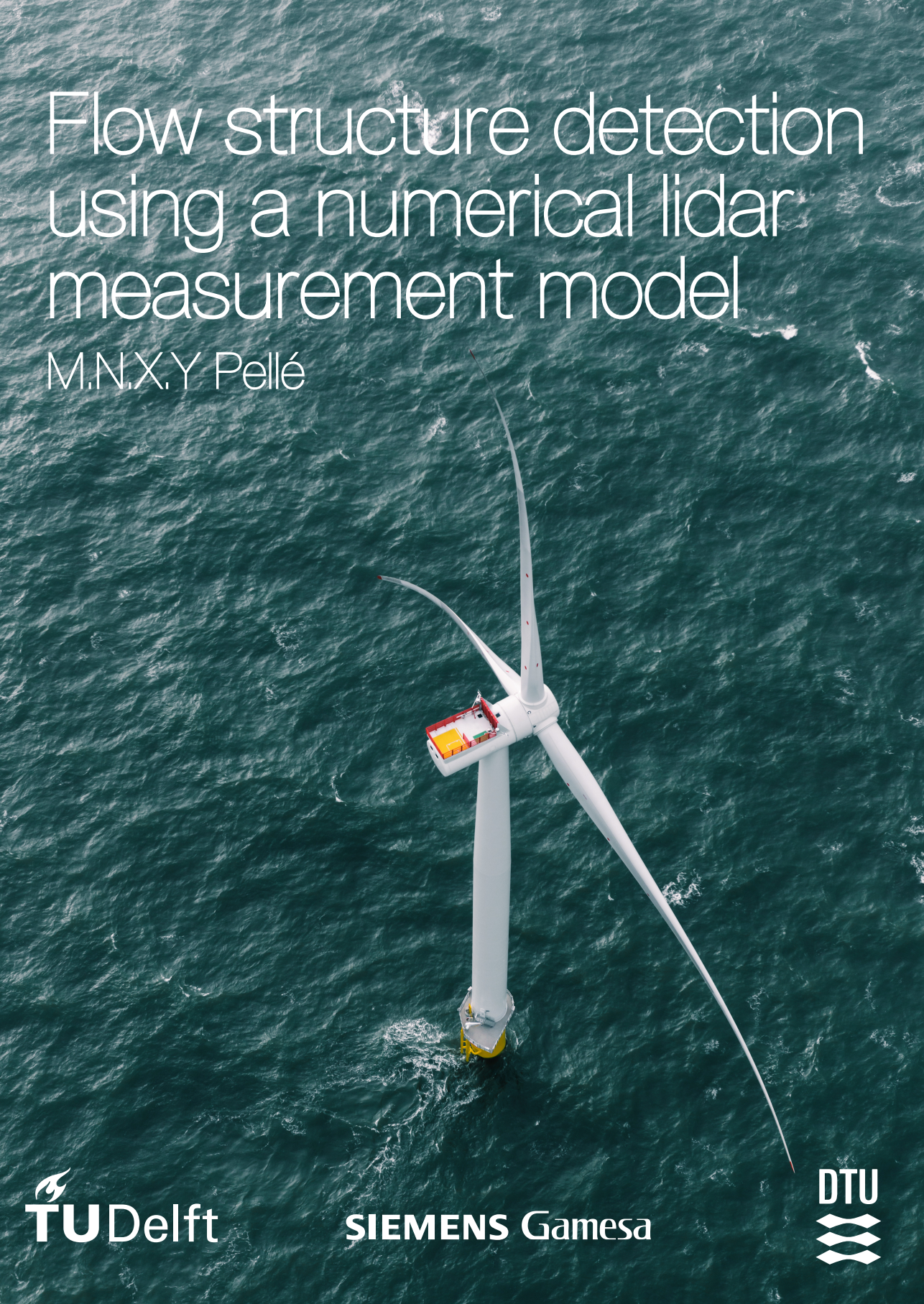

TU Delft
SIEMENS Gamesa
DTU

Flow structure detection using a numerical lidar measurement model

by

M.N.X.Y Pellé

to obtain the degrees of

Master of Science
in Aerospace Engineering at
Delft University of Technology

Master of Science
in Engineering (European Wind Energy)
at Technical University of Denmark

To be defended on August the 18th, 2022

Supervisors:	Dr. ir. W.A.A.M. Bierbooms	TU Delft
	Dr. M. Sjöholm	DTU
	Dr. N.G.W. Warncke	SGRE
Thesis committee:	Prof. dr. S.J. Watson	TU Delft
	Dr. ir. E. van Kampen	TU Delft
	Dr. L. Landberg	DNV
Thesis work duration:	November 2021	July 2022
Student number:	TU Delft - 4650077	DTU - s203204

Cover photo by Tristan Stedman, SGRE, SWT-6.0-154, Race Bank, UK

Report template adapted from `https://github.com/Inventitech/phd-thesis-template`

An electronic version of this thesis is available at
`https://repository.tudelft.nl` and `https://findit.dtu.dk`

TU Delft

SIEMENS Gamesa
RENEWABLE ENERGY

DTU

Abstract

With the increasing number of wind farm projects, a growing interest is seen towards the extension of wind turbine durability and the optimisation of energy production. A promising technology in this direction, is the use of lidars for remote sensing of wind fields and particularly for lidar-assisted control of wind turbines. Many investigations have been carried out to study the performance of lidars for measuring global wind statistics and test out lidar-assisted control strategies. However there appears to be less research efforts towards identifying and characterising localised and specific flow structures within the wind field, which is the aspect of focus in this study.

Whilst the main objective is to detect flow structures, this study also dives into the lidar measurement process. A striking feature of this process is the extensive data processing procedure applied to reduce noise and provide a final output in the form of the line-of-sight velocity. As this consists on relatively large data reduction and condensing steps, the question therefore arises, is useful information lost during this process?

To investigate the different stages of the lidar measurement process, a continuous wave lidar emulator was developed and served as the main tool for simulating lidar operation under controlled conditions. The first part of the investigation was performed on the Lamb-Oseen vortex, and was aimed at finding traces of the vortex within the lidar outputs. Besides, the line-of-sight velocity output, the Doppler spectrum was also analysed in a statistical sense with the use of moments. Three main indicators of the presence of the vortex were identified in the velocity envelope and the variations of the Doppler spectrum standard deviation and skewness across the vortex core. Tests were performed to see the effects of varying conditions (core size, noise, line-of-sight effects, etc.) on these patterns. From these sensitivity tests, a possible approach at characterising the vortex position, core radius and circulation was formulated. Further testing was then performed by adapting the methods used to a LES simulated wind turbine tip vortices.

In all tests performed, it is clear that the most detrimental obstacle to reliable vortex detection arises from the surrounding flow field which distorts the structure of the vortex and hence the regularity of the patterns identified within the lidar measurement process. An additional barrier are measurement process noise sources which tend to damp the signal rather than distort it, thus weakening but preserving the general shape of the identified features.

Applicability of the detection method developed is possible, but challenging in real operating conditions, due to the noisy background wind field and the ignorance of the approximate vortex location in the wind inflow. However, with continued and improved future studies, the approach shown may result in a suitable way of determining wake regions from the detection of tip vortices, thus providing a valuable input for wind turbine control and wind farm power optimisation.

Acknowledgements

This marks the end of my journey as an EWEM student. A journey full of ups and downs but made up of unique experiences and a multitude of incredible encounters. The final outcome has been made possible as a result of nine months of hard work, and with the help, support and contributions of many.

First of all, I would like to thank my daily supervisors, without which this endeavour would not have been possible. Thank you for your guidance, all the detailed feedback, inspirational ideas and time spent in helping me achieve this result.

I would like to express my gratitude to the SGRE team in France, for allowing me discover a variety of fascinating R&D topics I may not have been exposed to in my studies and for being able to witness the organisation and development behind part of the wind industry. I am particularly thankful to Paul and Norbert for giving me this unique opportunity and being able to feel like my work can be built upon and be the source of further opportunities and collaborations. Many thanks to Félix for sharing his own work with me and for spending the time with Étienne to set up and run the wake simulations.

I would like to extend my gratitude to my fellow students and the SGRE team in the Den Haag office, for welcoming me and for creating such a great atmosphere there. A special thank you to Colinda for making the entire process so smooth and for all the times I asked for extra office days.

Lastly, and perhaps most especially, thank you to my friends and family for all the refreshing discussions and, the continuous and essential support during these last couple of months.

Mathieu Pellé
Delft, July 2022

Contents

List of Figures

List of Tables

Nomenclature

Abbreviations

pdf	Probability density function
ABL	Atmospheric boundary layer
AEP	Annual energy production
ALM	Actuator line model
BS	Backscatter
CW	Continuous wave
DFT	Discrete Fourier transform
DS	Doppler spectrum
FFT	Fast Fourier transform
LAC	Lidar assisted control
LES	Large eddy simulation
LO	Lamb-Oseen
LOS	Line-of-sight
RHI	Range height indicator
SNR	Signal to noise ratio
TEM	Transverse electromagnetic mode
TI	Turbulence intensity
VAD	Velocity azimuth display

Greek symbols

α	Shear exponent	[-]
β	Backscatter coefficient	$[\mathrm{m^{-1}\,sr^{-1}}]$
χ	Lidar beam to vortex axis angle	[°]
δ_{VLOS}	Line-of-sight velocity bin size	$[\mathrm{m\,s^{-1}}]$
Γ	Circulation	$[\mathrm{m^2\,s^{-1}}]$
λ	Wavelength	[m]
μ	Mean	[variable dependent]
ω	Angular frequency	$[\mathrm{rad\,s^{-1}}]$
ϕ	Signal phase	[rad]
σ	Standard deviation	[variable dependent]
τ	Range-gate sampling time	[s]

θ	Lidar beam azimuth angle	[°]
θ_d	Divergence angle	[°]
φ	Lidar beam inclination angle	[°]

Roman symbols

A	Signal amplitude	[-]
a_0	Effective aperture radius	[m]
c	Speed of light	[$\mathrm{m\,s^{-1}}$]
D	Rotor diameter	[m]
d_p	Aerosol diameter	[m]
E	Electric field amplitude	[$\mathrm{V\,m^{-1}}$]
F	Beam focus range	[m]
f	Frequency	[Hz]
H	Histogram counts/frequency	[-]
I	Intensity	[$\mathrm{W\,m^{-2}}$]
N	Number of points	[-]
P	Power	[W]
r	Radial coordinate	[m]
r_c	Vortex core radius	[m]
s	Axial coordinate (along beam) beam focus range F	[m]
Sk	Skewness	[-]
t	Time	[s]
t_p	Pulse duration	[s]
U_∞	Free stream velocity	[$\mathrm{m\,s^{-1}}$]
V_θ	Vortex tangential velocity	[$\mathrm{m\,s^{-1}}$]
V_{LOS}	Line-of-sight velocity	[$\mathrm{m\,s^{-1}}$]
W	Range weighting function	[-]
w	Beam radius	[m]
w_0	Beam waist	[m]
z_R	Rayleigh length	[m]

1

Introduction

In the hope of achieving the goal of net zero emissions by mid-century set out by the UN Climate Change Conference [1], the share of renewable energy sources in the global energy production is set to increase and dominate in the coming years. In Europe, it is expected that wind energy will become the leading energy source past 2025, supplying 50% of the EU's needs by 2050 [2]. For these objectives to be met, the need for a lower levelised cost of energy, particularly for offshore wind turbines is necessary and can partly be achieved with increased wind turbine reliability and overall durability [3].

Wind turbines are typically designed with an operational lifetime of 20 years [4, 5], during which they are subject to large ultimate loads as well as a considerable amount of load cycles as a result of inertial loads from the rotor but also from fluctuations in wind velocity also referred to as turbulence [5, 6]. Whether it arises from the planetary boundary layer or wind turbine wakes, turbulence has been found to be proportional to fatigue loading [7], and it is therefore important to gain sufficient knowledge of the expected turbulence a wind turbine will face during its lifetime and try to minimise resulting fatigue loads.

Light Detection and Ranging (lidar) technology allows for the remote detection of wind speed and already offers an appealing alternative to traditional sensing technology such as meteorological masts. With the ever increasing size of wind turbine rotors, lidars are being increasingly applied to wind resource assessment, prototype validation and wind turbine control [8, 9], the latter being the application of interest in this thesis. Using lidars to characterise the wind field upstream of the wind turbine, allows the controller to operate ahead of time and effectively optimise the wind turbine for the incoming wind conditions. This can lead to reduced extreme and fatigue loads that arise from gusts, eddies, shear or more generally turbulent flow structures and in conclusion improve the wind turbine's durability and prolong lifetime.

It is natural to first take interest of previous applications of lidars in flow structure detection. Lidars have been applied for to a vast scope of flow types and conditions. As one can expect, wind speed estimation for resource assessment is a popular research area, with more recently, focus on understanding flow behaviour in complex terrain regions (e.g. [10, 11]). Extensive research has been performed in the field of lidar turbulence quan-

tities estimation such as turbulent kinetic energy dissipation rate, length scales, cross-correlation or even velocity structure function as summarised and presented by Sathe [12]. Similarly, wakes have also been greatly studied, for example to quantify velocity deficit and turbulence intensity [13] or with lidar wake characterisation in complex terrain [14, 15] and wake detection using spectral broadening [16]. There however appears to be fewer investigations into the characterisation of coherent flow structures using lidars for wind energy applications. Large scale coherent structures in the atmospheric boundary layer, such as rolls and streaks, have been detected using dual Doppler lidar and permitted the calculation of integral lengths scales [17]. Classification of similar, large scale structures, was also performed using supervised machine learning by Cheliotis et al. [18]. There also exists examples of identifying vortical structures in the flow field upstream of wind turbines, although not using lidars. The effect of vortical coherent structures on wind turbine loading and wake recovery has been evaluated by using natural snow as a flow visualisation technique [19] and Mauz [20] made use of an unmanned aircraft system equipped with pressure probes to characterise blade tip vortices.

To find further investigations of flow structure detection using lidars, one can review research in the aeronautics domain where lidars have been tested for shear, turbulence, gust and wake vortex detection [21]. Pulsed and continuous wave lidars have both been experimentally field tested by Wu et al. [22] and Harris et al. [23, 24] respectively to detect aircraft tip vortices during landing. Numerical tests of such conditions have also been performed [25]. Various detection algorithms have also been developed to characterise the vortex strength. The most common appears to be the velocity envelope method which makes use of the positive and negative velocity peaks detected [26, 27]. Other approaches make use of estimators together with analytical vortex models [28, 29] or even a hybrid approach that uses both algorithm types [30]. From the observations of most studies [23, 26, 28, 29], it can be concluded that the tip vortex detection becomes increasingly challenging with increasing flow complexity for example in the presence of atmospheric turbulence that increases vortex decay and decreases signal-to-noise ratio (SNR).

As presented, a diverse amount of flow types have previously been analysed using lidars, although there are limitations, particularly dependent on the flow complexity and how well it can be defined. However, it has become apparent during this literature review that detecting flow structures relies majorly on line-of-sight velocity measurements and rarely makes use of other information collected by the lidar. In reality, the lidar measurement process makes use of large amounts of data and reduces it down to a single line-of-sight velocity measurement. Other potentially useful information, in the form of the phase or power spectra are either ignored or averaged out to decrease the noise level. The aim of the current research proposal is therefore to develop a numerical lidar model to investigate signatures within the measurement process of turbulent flow structures, which could for instance lie within the phase, power or Doppler spectra for example. This is performed in the hope to provide information from lidar outputs, other than the line-of-sight velocity whilst also striving for better characterisation of flow structures for wind energy applications.

The initial approach to this task is to construct a numerical model of the lidar measurement process which gives the freedom of testing different flow cases and lidar characteristics with relatively fast implementation. The first focus will be on understanding the

measurement process and in particular the way various noise sources arise and contribute to the measured signal. Following this, the model will be tested with 'simple' vortex flow cases, in an effort to reproduce results similar to the ones obtained in [23–25, 28, 30], whilst striving to identify a pattern in the measurement process that may indicate the presence of a vortex. Further testing will then be carried out with varying vortex orientation, size, strength and superposition of other flow fields such as a global advection wind speed or small scale turbulence. Finally, the model will be tested with flow structures resembling those found in the wake of a wind turbine where tip vortices occur.

1.1 Research Objective and Questions

In order to establish a well-defined research framework, the work presented within this thesis is realised with a certain goal to achieve, which can be summarised in the following way:

The research objective is to extract a greater level of information from the lidar measurement process in order to enhance the use of lidar-assisted control by constructing a numerical lidar model, understanding the contributions of noise sources to the measurement errors and uncertainties, and determining possible approaches or patterns within the lidar measurement process for the identification of turbulent flow structures.

To help structure and isolate the tasks to complete towards achieving the research objective, the following sub-objectives can be defined:

- **RSO1** Construction of a lidar emulator model: consisting of a continuous wave lidar with user-defined properties (beam type, sampling points, noise, etc.) and the data processing chain.
- **RSO2** Verification and validation of the model: making use of software unit and module tests for checks, applying model to simple flow cases which can be validated analytically.
- **RSO3** Evaluation of the model with vortices: using line-of-sight velocity and expanding into phase, power spectra or time series to observe effect of added vortex.
- **RSO4** Expansion to higher complexity flows: making use of the approaches found in **RSO3** on flow fields with more advanced features such as turbulence, shear, gusts or wakes.

Once these sub-objectives have been met, the research is then carried out in the hope of answering the following research questions:

- **RQ1** Can a generalised approach or approaches within the numerical lidar measurement process be identified to detect turbulent flow structures?
- **RQ2** Which parameters of the turbulent flow structures can reliably be detected by the lidar model?

- **RQ3** How is the uncertainty in the detection and characterisation of turbulent flow structures affected with increasing flow complexity?

1.2 Report outline

The following parts of the report are all dedicated towards answering the research questions. Chapter 2 provides the theoretical basis for all future developments in this thesis. The aim is to collect all necessary knowledge concerning firstly, lidars and their operating principles, and secondly, relevant flow phenomena and the various features they exhibit. Once this is achieved, Chapter 3 will present the lidar model developed and that serves as the main tool for the testing phase of the thesis. The lidar emulator's structure, modelling assumptions and different features are detailed and some initial verification tests and comparison between different modelling approaches will be shown. Chapter 4 will introduce the first step towards answering the research questions, and will demonstrate the approach taken to detect and characterise a simple flow structure in the form of a vortex. Chapter 5 will then adapt and test the methods presented in chapter 4 to more realistic and complex flow structures found in the wake of a wind turbine. Finally, chapter 6 will summarise the main findings of this thesis along with possible future research within this scope.

2 Theory

The aim of this chapter is to present the reader with the necessary theoretical background that supports the rest of this study. The first section will introduce lidar technology and delve into the details of the measurement process, in order to serve as a knowledge basis for the creation of a lidar emulator. The second section will present the various flow types that were used and modelled in the experimental phase.

2.1 Lidar

LIght Detection And Ranging (lidar) technology first appeared in the 1930s when attempts were made to measure altitudes and density profiles with light beams. With the invention of the laser in the 1960s, faster development of lidar technology began, offering its use to a very wide and diverse range of applications. This started from rangefinders, obstacle detection and autonomous navigation to imaging, atmospheric or ocean sensing and of course remote sensing for wind energy [31, 32].

The need for remote sensing in wind energy has augmented as a result of the constant increase in size of wind turbines. This has rendered the use of meteorological masts to be too expensive for such scales and also inaccurate as the central hub wind speed now becomes unrepresentative of the wind speed across the rotor plane [9]. The current motivations for using lidars in remote sensing for wind energy can therefore be summarised with the following [8]:

- Wind resource assessment: Wind speed, direction and turbulence measurements for siting or mapping wind climates in various terrains.
- Wind turbine performance verification: Using measurements as input conditions for evaluating wind turbine power curves or experimental testing.
- Wind turbine control: Measuring and characterising incoming wind to inform controller (yaw, pitch) of variations in wind speed or direction, gusts, wind shear, etc.

2.1.1 Setup

Similarly to other remote sensing techniques, lidars use electromagnetic waves in order to perform measurements, and as the name suggests, electromagnetic waves in the optical to infrared wavelength range are used, usually in the order of 1.5 µm [8]. These light waves are emitted from a laser transmitter and pass through the necessary optics (lens, beam expander, etc.) before hitting any obstacles, which in the case of wind lidars are aerosols contained in the air and assumed to travel at the same speed [8]. The signal is then partially absorbed, transmitted or reflected depending on the properties of the aerosols. The lidar's receiver block then detects the backscattered signal and is able to generate an electronic signal [31]. There exists two variants of transmitter-receiver geometry: monostatic which consists of the transmitter and receiver being collocated, and bistatic where the transmitter and receiver are separated as shown in Figure 2.1. It is however more common for wind lidars to use a monostatic configuration due to the simplicity of the alignment setup and the possibility to share optics for both transmitter and receiver [8].

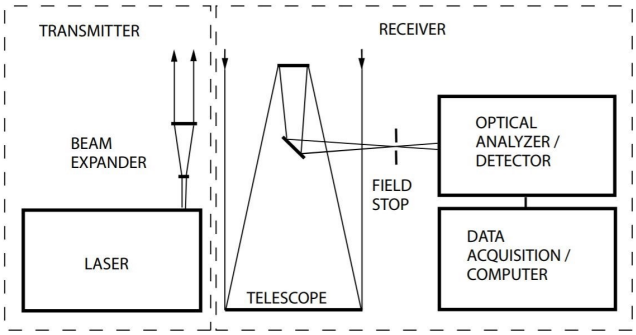

Figure 2.1: Lidar system setup. Obtained from [31].

2.1.2 Light scattering

The light beams emitted from the lidar may interact with the atmosphere when light photons are either absorbed or scattered by any obstacle present in the atmosphere under the form of molecules, aerosols, clouds, etc. The overall process, called extinction, represents the loss of light in the atmosphere and is mainly dominated by absorption, although some aerosols such as soot absorb more than they scatter [33]. The levels of absorption and scattering are thus dependent on the type of aerosol or molecule but also on the light's wavelength. Absorption of infrared wavelength by atmospheric molecules varies quite extensively across the full range of wavelengths and so-called atmospheric windows, or regions of low atmospheric attenuation occur [34]. The exact wavelength of emitted light is therefore selected such that it remains within such a window, this is in the range of 1.55 µm-1.8 µm for lidars.

The backscatter coefficient $\beta(\lambda, z)$ quantifies how much light is scattered backwards (at a scattering angle of 180°) and is dependent on the incident light's wavelength and altitude. Its value can be as low as $10^{-8}\mathrm{m}^{-1}\,\mathrm{sr}^{-1}$ in clear boundary-layer air [8]. In order to analyse backscattered signals it is first important to understand how this signal first

occurs. Firstly, there exists two forms of scattering, elastic and inelastic. The former being when no energy exchange takes place and hence the signal wavelength or frequency remains unchanged. The later occurs when energy is exchanged, resulting in a change of the signal's wavelength [31, 35]. These forms of scattering occur at different frequencies and different kind of information can be extracted from the backscattered signals such as temperature, aerosol properties, cloud heights or wind speed for example. However the following two types of elastic scattering are the most important for wind (Doppler) lidars [36]:

- *Rayleigh*: Scattering arising from particles with diameters approximately a tenth smaller than the incident light's wavelength. This can also be referred to as molecular scattering and in the case of wind lidars is generated from air (Nitrogen and Oxygen mostly). The intensity scales with λ^{-4} and may vary with atmospheric conditions leading to a spectral broadening of the scattered signal [31]. The scattering distribution is presented in Figure 2.2.
- *Mie*: Typically defined as the scattering from particles with larger or similar diameters to the incident light's wavelength (aerosols such as dust, soot, smoke, pollen or also ice and rain). However, it may also be defined as a general scattering theory, independent of particle size, and hence encapsulates Rayleigh scattering as well [31]. There does not exist a simple relation between intensity and wavelength but it has been estimated to be proportional to λ^{-1} or λ^{-2} depending on the composition of the aerosols in the atmosphere [37]. As seen from Figure 2.2, the scattering direction is less uniform and a weaker backscattering signal is formed for larger particles given the same frequency.

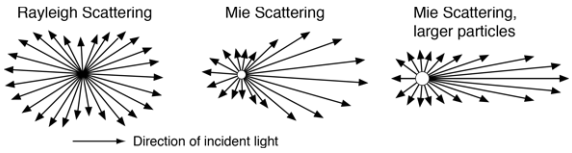

Figure 2.2: Light scattering direction for different particle sizes [38].

Figure 2.3 shows the collected frequencies at the lidar receiver. A molecular spectrum appears as a result of the Rayleigh scattering of air molecules and an aerosol peak occurs from Mie scattering. Gas molecules move in random motion and typically at high speeds, depending on the temperature and molecular properties. This is measured by the Doppler phenomenon and explains the various range of frequencies detected from the molecular return and the broadening of the spectrum. Aerosol particles are however much heavier and slower, meaning that they tend to travel with the wind and hence give a good approximation of the wind speed. Furthermore, background light also creates a floor signal and arises from external light beams (solar radiation for example) being collected [37]. The spectrum detected by wind lidars may differ from the one presented in Figure 2.3 as the lidar is limited in the range of frequencies it can detect. From the range of velocities of each

scattering regime, it can be obtained that molecular backscatter frequencies may deviate by as much as 400 MHz (or ~ 300 $m s^{-1}$) from the mean frequency whilst Mie backscatter frequencies will vary less, 13 MHz (assuming turbulent wind variations of ~ 10 $m s^{-1}$) [39]. Wind lidars such as the *ZephIR* lidar have a maximum frequency of 50 MHz, thus not all backscattered frequencies can be resolved but this provides a sufficiently large range of velocities.

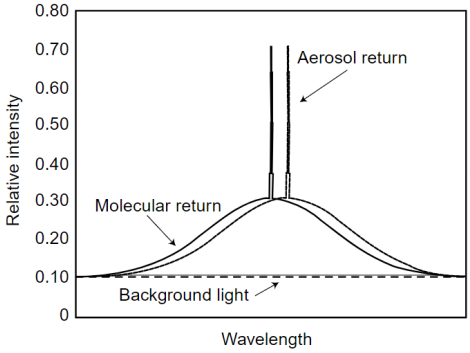

Figure 2.3: Typical spectrum of backscattered signals [37]

2.1.3 Lidar Equation

As previously described in subsection 2.1.2, the atmosphere interacts with emitted light beams, meaning that the return (backscattered) signal power is different to the emitted signal power. Equation 2.1 accounts for the contributions of the lidar settings (emitted power, geometry, efficiency) and atmospheric conditions (amount of backscatter, losses from absorption) to the signal power [31].

$$P(z,\lambda) = KG(z)\beta(z,\lambda)T(z,\lambda) \tag{2.1}$$

K is the system factor, given by Equation 2.5, where P_0 is the emitted power, $ct_p/2$ is the spatial pulse length, η is the system efficiency (including both detection and optical performance efficiencies) and A is the receiver area which can be computed from $A = \pi\sigma_a^2$ where σ_a is the aperture radius. $G(z)$ is the geometric factor and incorporates the effect of the measurement range as seen with Equation 2.6. It is dependent on the range z which decreases power as an inverse square law and an overlap function $O(z)$, which is a factor of the amount of area overlap between the laser and detector field of view, and hence typically higher in monostatic configurations. It can also be noted that when grouping Equation 2.5 and Equation 2.6, the term $\frac{A}{z^2}$ appears which is the solid angle of the telescope.

$$K = P_0 \frac{ct_p}{2} A\eta \quad (2.5) \qquad G(z) = \frac{O(z)}{z^2} \quad (2.6) \qquad \beta(z,\lambda) = \sum_j N_j(z) \frac{d\sigma_{j,sca}}{d\Omega}(\pi,\lambda) \quad (2.7)$$

The effect of the atmosphere is formulated with two terms, namely backscatter given by Equation 2.7 and transmission given by Equation 2.8. The backscatter coefficient, $\beta(z,\lambda)$, describes the ratio of signal that is propagated back towards the incident direction. This is approximated by taking the sum over all particle types, j, of the differential scattering cross section at a specific wavelength, $d\sigma_{j,sca}/d\Omega(\pi,\lambda)$, weighted by the particle's concentration N_j. Note the scattering angle of π which is backwards.

Finally, the transmission term, $T(z)$, encapsulates the loss in power as a result of extinction, which is absorption or scattering in other directions and is formulated from the Beer-Bouguer-Lambert law. The level of extinction, α, is integrated over the full return path. Similarly to the backscatter coefficient, the extinction coefficient is obtained by taking a weighted sum of the extinction cross section of all types of particles present, as seen by Equation 2.9. Combining all equations, results in Equation 2.10, which is the final expression for the detected signal power. This equation remains quite detailed and it is often simplified to only account for dominant terms, such as the backscatter for example.

$$T(z,\lambda) = \exp\left[-2\int_0^z \alpha(z,\lambda)dz\right] \tag{2.8}$$

$$\alpha(z,\lambda) = \sum_j N_j(z)\sigma_{j,ext}(\lambda) \tag{2.9}$$

$$P(z,\lambda) = P_0\frac{ct_p}{2}A\eta\frac{O(z)}{z^2}\cdot\sum_j N_j(z)\frac{d\sigma_{j,sca}}{d\Omega}(\pi,\lambda)\cdot\exp\left[-2\int_0^z \alpha(z,\lambda)dz\right] \tag{2.10}$$

2.1.4 Doppler shift

In order to measure wind velocity, lidars make use of the Doppler effect, which relates the frequency shift between the emitted and backscattered signals to the relative speed of the signal source with the receiver. The signal is compressed if the sources are moving towards the receiver and expands if moving away from the receiver. This is represented with Equation 2.11 where Δf is the frequency shift, f_0 and λ_0 are the emitted frequency and wavelength respectively, c is the speed of light and V_{LOS} is the relative velocity or line-of-sight velocity.

$$\Delta f = \frac{2V_{LOS}f_0}{c} = \frac{2V_{LOS}}{\lambda_0} \tag{2.11}$$

It is important to note that as the name suggests, the line-of-sight velocity is the aerosols' velocity in the direction of the light beam. In order to resolve the full velocity components in three dimensions, it is necessary to make use of three light beams, to receive three different frequency shifts and hence compute three different line-of-sight velocities.

2.1.5 Gaussian beam

A simple laser consists of an optical cavity enclosed by two aligned mirrors (resonator) and filled with a gain element which amplifies the power of light through it. Light bounces

2

off the resonator in spatial pattern of transverse electromagnetic modes or TEM_{nm} modes with n and m as mode numbers. The lowest order mode or TEM_{00} is characterised by the smallest beam waist and divergence (presented below), thus making it easier to focus on a single spot [40]. The intensity of this TEM_{00} can be described by a Gaussian beam profile. The variation in the beam's intensity in radial (r) and axial (z) direction is characterised by Equation 2.12 [41], where $w(z)$ is the beam radius, w_0 is the beam waist and P is the power of the beam which can also be written as a function of peak irradiance $P = \frac{\pi w_0^2}{2} I_0$.

$$I(r,z) = \frac{2P}{\pi w(z)^2} e^{-\frac{2r^2}{w(z)^2}} \tag{2.12}$$

Equation 2.13 gives the expression for the beam radius as a function of the axial position and the Rayleigh range z_R which in turn is dependent on the beam's wavelength λ and the beam waist. A visual representation of theses quantities and the beam geometry in the waist region is depicted in Figure 2.4. The Rayleigh length is the distance at which the beam radius has reached $\sqrt{2}w_0$ and where the cross-sectional area has doubled. Furthermore, θ represents the divergence angle and characterises the beam geometry in the far-field regions, where the beam follows a linear expansion. The parameter F represents the measurement range, or the point at which the beam is focused, and s is the distance measured from the beam focus to the lidar meaning that $s = F - z$.

$$w(z) = w_0 \sqrt{1 + \left(\frac{z}{z_R}\right)^2} \quad \text{with} \quad z_R = \frac{\pi w_0^2}{\lambda} \tag{2.13}$$

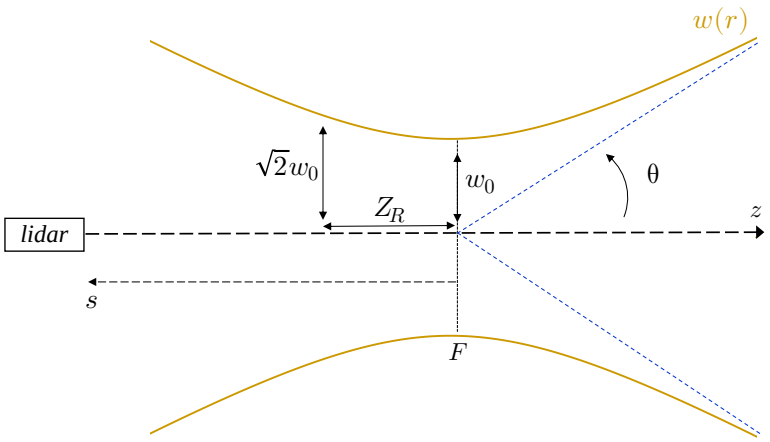

Figure 2.4: Beam geometry definition.

Figure 2.5a shows the shape of the Gaussian beam across the full radial and axial domain. In the Doppler lidar measurement process, the Gaussian beam intensity function is utilised to weigh the signal contributions received from different spatial locations in the beam, in order to compute the line-of-sight velocity at the measurement point. This

weighting is a convolution of the line-of-sight velocity along the beam and the range weighing function (W) given by Equation 2.14. Notice that the spread of the Gaussian is much larger in axial direction than in radial direction, as also shown in Figure 2.5b. Hence, it is usually the case that the radial spread of the beam is ignored in the weighting function and only follow from the axial spread.

$$V_{LOS}(F) = \int_{-\infty}^{\infty} V_{LOS}(s) W(s) ds \tag{2.14}$$

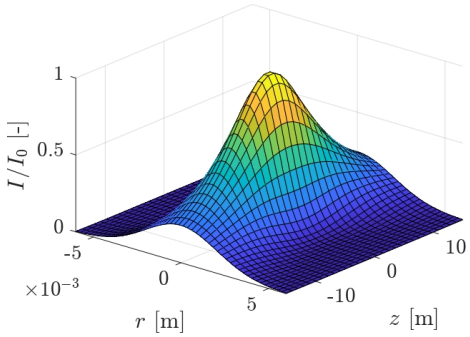

(a) Radial and axial distribution.

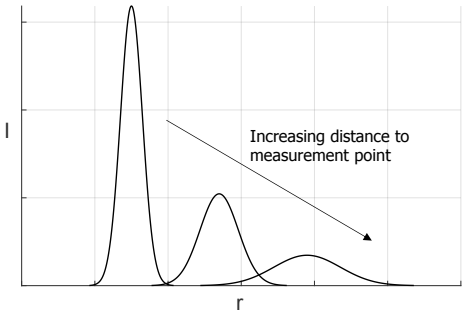

(b) Axial broadening.

Figure 2.5: Gaussian beam intensity distributions.

2.1.6 Types of lidars

To detect the signal frequency shift, two main types of lidars can be employed. The first are *Coherent lidars* which measure the frequency shift by mixing the backscattered signal with a local oscillator or reference beam. This leads to the phenomenon of 'beats', by which the interference of two signals at slightly different frequencies alter the amplitude of the resultant signal due to the phase difference of the source signals. The variations in amplitude is referred to as beats and occurs at the beat frequency [42]. Photodetectors respond to intensity which is proportional to the square of the signal electric field, $I \propto E^2$. The following expression can be derived for the interference of the fields of two signals [43]:

$$\begin{aligned} E^2 &= \left(E_0 \cos(\omega_0 t) + E_{BS} \cos(\omega_{BS} t)\right)^2 \\ &= E_0^2 \cos^2(\omega_0 t) + E_{BS}^2 \cos^2(\omega_{BS} t) + 2E_0 E_{BS} \cos(\omega_0 t) \cos(\omega_{BS} t) \\ &= E_0^2 \cos^2(\omega_0 t) + E_{BS}^2 \cos^2(\omega_{BS} t) \\ &\qquad + E_0 E_{BS} \left[\cos((\omega_0 + \omega_{BS})t) + \cos((\omega_0 - \omega_{BS})t)\right] \end{aligned} \tag{2.15}$$

What is interesting to note here is that the photo detector cannot respond to a very large range of frequencies and typically measures frequencies in the order of MHz. The backscattered signal being in the order of 2×10^{14} Hz, and using a local oscillator frequency of a similar order, the term containing the frequency difference, or beats frequency (ω_0 –

ω_{BS}), can now be measured. Additionally, this term is also amplified by the local oscillator. Note that this process may also be referred to as *heterodyne* detection as it employs two frequencies. An additional shift in the local oscillator frequency may also be added to the emitted signal only and not to the local oscillator frequency used for mixing. This allows to determine the direction of the frequency shift and hence velocity.

The second type of lidars are *Direct-detection lidars* which make use of molecular backscatter (Rayleigh component) and spectral filters to measure frequency shifts. As a single frequency is used, this detection process is also called *homodyne*. Their use for wind remote sensing is however quite difficult as they require corrections when the Mie peak (Mie frequency component) is in the same order of intensity as the Rayleigh signal and shifts [31]. Direct detection lidars are therefore more suited for higher altitude measurements, where the aerosol concentration is not as high as close to the ground.

Coherent lidars can then be further classified depending on their emission waveform, into namely *continuous wave (CW)* lidars and *pulsed lidars*, which will be presented in the two sub-sections below and compared in Table 2.1.

Continuous wave lidars

Continuous wave (CW) lidars emit and focus a laser beam towards a specific location or measurement point in space. A continuous backscatter and Doppler shift is therefore measured. The telescope's design controls the lidar's measurement range and spatial resolution [8]. A larger telescope aperture not only allows for shorter measurement ranges, but also narrower beam waists for the same focal length, leading to a better defined measurement volume. The telescope's Rayleigh length is proportional to the square of the measurement range, the spatial resolution hence decreases with range and this defines the lidar's maximum range, given an upper limit on the telescope aperture. This is given by Equation 2.16 with a_0 the effective aperture radius and F as the measurement range [44]. CW lidars typically perform measurements in the range of 10 m to approximately 200 m, longer ranges are possible but will come at a reduced SNR [12].

$$z_R = \frac{\lambda F^2}{\pi a_0^2} \tag{2.16}$$

As described in subsection 2.1.5, weighting functions are used to distribute accordingly the contributions of the measurement volume to the line-of-sight velocity. This is done by integration of a simplified Gaussian beam profile. For CW lidars, a Lorentzian function, given by Equation 2.17 is used [44]. Note that s is simply the distance along the beam but measured from the focal range (F) or $s = F - z$. Figure 2.7 shows how the range-weighting function varies with the F. The Rayleigh length was obtained using the input parameters from the *ZephIR* lidar by *ZX Lidars* [44, 45] as an example.

$$W_{CW}(s) = \frac{1}{\pi} \frac{z_R}{z_R^2 + s^2} \tag{2.17}$$

In order to measure wind speed at various locations, the beam's orientation and the distance between the laser emitting fibre and the focusing lens is changed to refocus the beam to a new measurement point in space. Furthermore, to obtain the full wind velocity vector, a minimum of three measurements needs to be performed. This is typically done

in a conical scanning pattern as shown by Figure 2.6 where Z_1 to Z_3 represent different height levels. A least-squares fit can be applied to when the number of measurements is greater than three. There however exists various other scanning patterns, such as the ones presented in the work of Dimitrov et al. [46], which differ in the number and position of measurements taken across the measurement plane. These patterns are sometimes better suited for measuring turbulent wind fields, when a higher number of points is used across the measurement plane, allowing for a higher spatial resolution of the wind field and the ability to detect local variations in wind speed or small scale turbulence. This is not the case in the conical scan, for example, which assumes flow homogeneity across each disc [47].

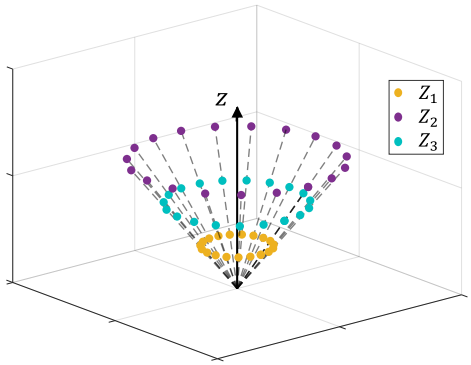

Figure 2.6: Conical scanning pattern of CW lidar.

Pulsed lidars

Pulsed lidars differ in the way the laser is emitted, however the concepts previously described for Doppler lasers remain applicable. A continuous wave laser is used to generate both the local oscillator and the laser pulses which are emitted at the pulse repetition frequency. The Gaussian beam intensity profile is simply enclosed inside the travelling pulse. The spatial resolution (or measurement volume) is independent of the measurement range as the beam is not focused onto a precise location but collimated. Range-gating is then used to process the backscattered signals. This classifies the backscattered signal by their time of arrival in order to distinguish the measurement distance corresponding to the backscattered signal [8]. Pulsed lidars can therefore measure multiple ranges simultaneously, but this reduces the data acquisition rate due to the processing time of several pulses. Additionally, the pulse length may be varied to expose more or less aerosols to the laser beam, thereby increasing the measurement range [12].

A range weighting function is also applied for pulsed lidars and is obtained by integrating the intensity of the pulse within the range-gate length [48, 49]. As the pulse's intensity is described by a Gaussian, error functions appear due to the integration of the Gaussian: $\mathrm{Erf}(x) = \frac{2}{\sqrt{\pi}} \int_0^x e^{-t^2}\, dt$. The weighting function is given by Equation 2.18 where τ, t_p, c are the range gate sampling time, pulse duration and speed of light respectively [44]. It

is important to realise that theoretically there is no focal range F here and s is therefore defined as the distance measured from the centre of the range-gate. In practice, pulsed lidars are often slightly focused at a fixed distance. Figure 2.7 shows the range-weighting function relative to the CW range-weighting function. The parameters of Equation 2.18 were chosen based on the *WindCube*® lidar from *Leosphere* [44], now *Vaisala* [50].

$$W_{pulsed}(s) = \frac{1}{\tau c}\left[\operatorname{erf}\left(\frac{1}{ct_p}s + \frac{\tau}{2t_p}\right) - \operatorname{erf}\left(\frac{1}{ct_p}s - \frac{\tau}{2t_p}\right)\right] \tag{2.18}$$

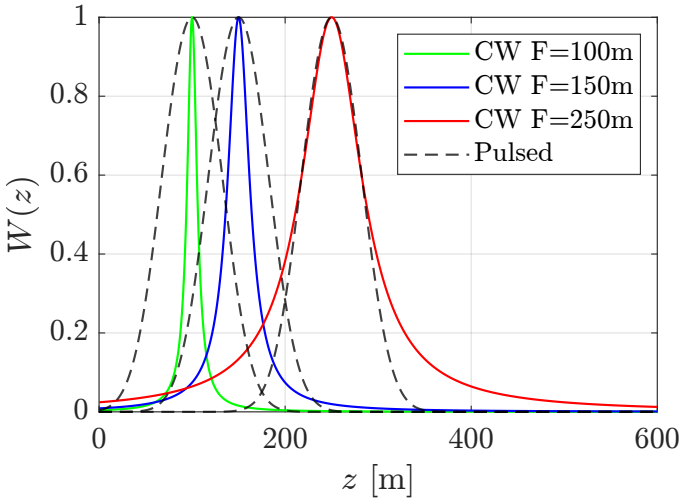

Figure 2.7: Comparison of normalised range-weighting function for CW and pulsed lidars.

Table 2.1: Comparison between CW and pulsed lidars [8, 12, 44].

	CW Lidars	**Pulsed Lidars**
Velocity accuracy	Limited by atmosphere coherence time.	Dependent on pulse duration.
Range gate	Determined by telescope focus. Increases as s^2	Determined by time of flight. Constant with s.
Minimum range	Short (~ 10 m)	Long 40 - 50 m. Blinded by pulse emission.
Maximum range	Dependent on telescope aperture. Few hundred meters	Dependent on pulse energy several kilometres
Data acquisition rate	Fast. Limited by sampling time only.	Slow. Limited by sampling time and time of flight for scanning.
Multiple locations (profiling)	Slow. Requires time to re-adjust and focus.	Fast. Range gating means only one pulse is necessary.

2.1.7 Signal processing and uncertainties

To obtain a velocity measurement from the output time series of the lidar detector, several steps are required and shown in Figure 2.8. The voltage output of the detector is first binned into blocks of 5 µs. Note that for pulsed lidars the range-gate length first needs to be identified before the binning takes place. Each interval is then Fourier transformed using a Discrete Fourier Transform (DFT) and squared to obtain a power or Doppler spectrum. In order to lower the floor noise level, all the Doppler spectra obtained are then averaged together to obtain a single averaged Doppler spectrum. The fluctuations in the floor noise level decrease with the square root of the number of averages, this is often of the order of 4000 [8]. Note that the power and Doppler spectra are functions of frequency but can then be converted to line-of-sight velocities via Equation 2.11. Once again, this process is done per range-gate for pulsed lidars. The peak frequency can then be identified and converted to an LOS velocity by use of the Doppler equation. This process may then be repeated to obtain the LOS velocity at other measurement points and reconstruct the wind field. Additionally, the Doppler peak may not always be sharp and can be composed of a small range of frequency shifts. This is a result of measuring particles moving at different velocities which can happen in the case of turbulence or shear but also due to the time delay between measurements when performing a conical scan.

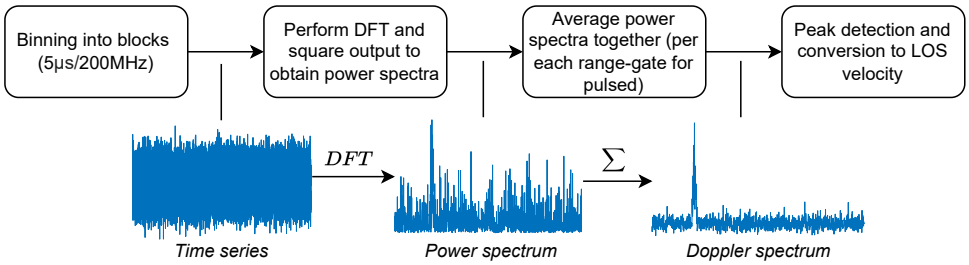

Figure 2.8: Signal processing phases. Reproduced from [8].

A number of assumptions are made when using lidars for measuring wind speed. The following list summarises the main uncertainties that may arise as a result of both atmospheric/environmental and system sensitivities. A more detailed investigation into lidar uncertainties can be found in [51].

- Aerosol composition: Aerosols are assumed to travel with wind speed but this may not always be the case for other particles or objects present in the atmosphere. For example, rain, snow or ice falling to the ground leads to an overestimate of the vertical velocity component.
- Aerosol concentration: The level of signal backscatter is dependent on the concentration of scattering particles in the air. Low concentration (clear air) may lead to a low SNR and larger uncertainty in the velocity measured.
- Aerosol distribution: Aerosols are assumed to be homogeneously distributed within the measurement volume when applying the range-weighting function.

- Obstacles: Light may be scattered by other moving objects (birds, aircraft) or stationary ones (wind turbines, trees, buildings). Their contribution to the Doppler spectrum can most likely be identified as outliers in the case of moving obstacles. Stationary obstacles will lead to data loss such as in the case of nacelle-mounted lidars being obstructed by a the turbine's blades.
- Clouds: Naturally, clouds also provide a source of backscatter signal, particularly in the case of wind profiling. They contribute to an inhomogeneous backscatter distribution but this can however be suppressed by making use of a 'cloud removal algorithm'. The cloud return signal is typically identified from its higher velocity and narrow spectral width. When focusing the beam closer to the cloud base, an increase in its Doppler peak can be detected and removed. Furthermore, clouds and fog may also hinder the lidar's power signal, restraining the lidar's measurement range.
- System accuracy: The lidar positioning and orientation may not be aligned with the right coordinates system. This will lead to errors in the measured velocity magnitude and direction.
- Flow homogeneity: For a single lidar, a scan is used to measure the full wind velocity vector. This assumes that flow across the measurement volume remains uniform or homogeneous whilst the scan is performed. This may not always be the case, for example in areas with complex terrain or conditions of high turbulence.
- Measurement volume: Air within the measurement volume may not be travelling at the same speed. This is particularly true in the case of shear layers and turbulent flows with the resulting spectra being skewed or broadened respectively.
- Terrain: Similarly to the previous two points, the complexity of terrain affects wind speed and can lead to speed-ups, veer or high turbulence causing flow inhomogeneity in the measurement volume.

2.2 Flow phenomena

The different types of flow features that will be tested in this study are presented in this section. The purpose is to present the terminology and main characteristics behind each phenomena. In most cases, the flow field is fully modelled, as solving the Navier-Stokes equations is too costly. A wind field is therefore generally modelled as the sum of different contributions: time-averaged shear, turbulence in a linearised transport form and gusts. Other flow structures such as vortices may then be superimposed onto such a simulated wind field. Only in the case of simulating wakes will a low-pass filtered version of the Navier-Stokes equations be solved, such that time dependent fluctuations are kept and a more realistic wake is obtained.

2.2.1 Wind shear

Wind shear describes the variation of mean horizontal wind speed with height from a surface. In simple cases, this may be described by a gradient of wind speed increasing

with height, however log or power laws are typically used to describe such wind speed profiles [52]. The log law is based on the law of the wall and derived from the boundary layer equations. This is given by Equation 2.19, and makes use of the von Kármán constant κ, the friction velocity U^* and the surface roughness length z_0 to relate the horizontal wind speed U as a function of the height z. On the other hand, the power law is an empirical fitting of the boundary layer and is given by Equation 2.20, uses a reference point with given height z_r and horizontal wind speed U_r, and a shear exponent α to vary the steepness of the profile [53].

$$U(z) = \frac{U^*}{\kappa} \log\left(\frac{z}{z_0}\right) \tag{2.19}$$

$$U(z) = U(z_{ref})\left(\frac{z}{z_{ref}}\right)^{\alpha} \tag{2.20}$$

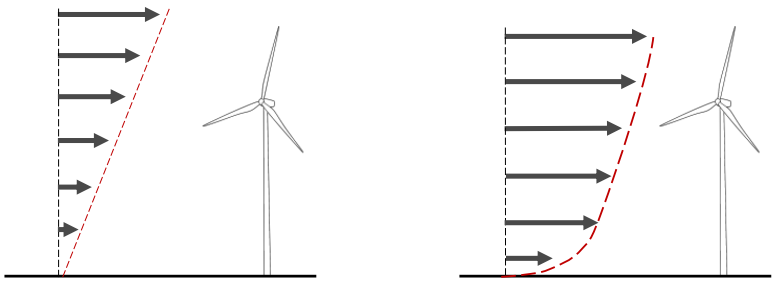

Figure 2.9: Linear (left) and log/power law shear profiles.

2.2.2 Turbulence

Turbulence refers to random-like fluctuations of velocity generated by the dissipation of turbulent kinetic energy. This phenomenon is described by the energy cascade, where large scale structures or eddies initiated by mechanical or thermal forces in the atmosphere, decay into smaller scale eddies. The level of turbulence is most commonly referred to as turbulence intensity or TI and is computed with Equation 2.21, using the standard deviation of wind speed, σ_u and the mean wind speed $\bar{U}$, which is a time-averaged measure obtained from Equation 2.22 [53, 54]. Figure 2.10 ([55]) shows a turbulent shear profile with the combined mean and fluctuating wind speed components.

$$TI = \frac{\sigma_u}{\bar{U}} \tag{2.21}$$

$$\bar{U} = \frac{1}{\Delta t}\int_0^{\Delta t} U(t)dt \tag{2.22}$$

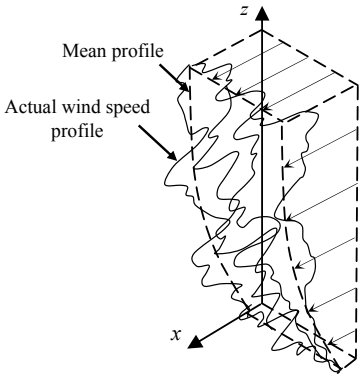

Figure 2.10: Turbulent shear layer. Obtained from [55].

There exist various solutions to modelling this fluctuating wind component, each with their own assumptions and complexities. However, as prescribed by the IEC standard, turbulence for wind applications is typically modelled with the Kaimal spectral model or the Mann uniform shear model [52]. The Mann model is the only one presented in this work as it is the chosen model for turbulent wind field simulations.

The Mann model is built on several assumptions listed below:

- *Linearised transport*: Eddies are advected with a mean streamwise transport velocity (Taylor's frozen hypothesis), removing the time dependence from the transport equations: $\vec{u}(x, y, z, t) = \vec{u}(x - Ut, y, z)$ [56].
- *Homogeneity*: Flow statistics are independent of position.
- *Isotropy*: Flow statistics are invariant under rotations.
- *Incompressibility*: Constant density: $\nabla\vec{u} = 0$.
- *Kolmogorov K41*: The slope of the energy spectrum decay is −5/3 [57].

The covariance tensor, defined by Equation 2.23, measures the statistical dependence of the velocities between different points. Given homogeneous turbulence, the Fourier transform of the covariance tensor may be taken, which leads to the power spectral tensor defined by Equation 2.24.

$$\mathbf{R}(\mathbf{r}) = \langle u(\mathbf{x}) \cdot u(\mathbf{x}+\mathbf{r}) \rangle \qquad (2.23)$$

$$\mathbf{\Phi}(\mathbf{k}) = \frac{1}{(2\pi)^3} \int \mathbf{R}(\mathbf{r}) e^{-i\mathbf{k}\cdot\mathbf{r}} d\mathbf{r} \qquad (2.24)$$

The wind field may then be obtained through the Fourier integral (Equation 2.25) of the orthogonal process given by Equation 2.26 (where * denotes the complex conjugate).

$$u(\mathbf{x}) = \int e^{i\mathbf{k}\cdot\mathbf{x}} d\mathbf{Z}(\mathbf{k}) \qquad (2.25)$$

$$dZ^*(\mathbf{k}) dZ(\mathbf{k}) = \mathbf{\Phi}(\mathbf{k}) d\mathbf{k} \qquad (2.26)$$

Using the incompressibility condition, $\nabla \cdot u(\mathbf{x}) = i\mathbf{k} \cdot u(\mathbf{k})$, and expressing the velocity field using Helmholtz decomposition, $\nabla\phi + \nabla \times \mathbf{A}$, the velocity field in Fourier space is left as $u(\mathbf{k}) = i\mathbf{k} \times \mathbf{A}(\mathbf{k}) = \mathbf{KA}$. Relating this back to the power spectral tensor gives Equation 2.27 and simplifying leads to the power spectral as a function of wave numbers only. The power spectral tensor can be desingularised at the origin using the integral length scale L and then scaled by $\alpha\epsilon^{2/3}/4\pi$ to give the von Kármán power spectral tensor as Equation 2.28.

$$\mathbf{\Phi} = u(\mathbf{k})\left(u^*(\mathbf{k})\right)^T = \mathbf{KA}\left((\mathbf{KA})^*\right)^T \quad (2.27)$$

$$\mathbf{\Phi}(\mathbf{k}) = \frac{\alpha\epsilon^{2/3}\left(k^2 I_3 - kk^T\right)}{4\pi\left(\frac{1}{L^2} + k^2\right)^{17/6}} \quad (2.28)$$

The two parameters of the von Kármán power spectral tensor are: the turbulence length scale (L) or size of energy containing eddies and the energy dissipation rate in the form of $\alpha\epsilon^{2/3}$. Note that the ϵ is the rate of viscous energy dissipation and α is a dimensionless constant in this case. The Mann model modifies this by incorporating a third parameter as the anisotropy parameter (γ) responsible for the distortion of eddies under shear. Furthermore, corrections for aliasing are made to the high-frequency component and numerical integration is used for the low-frequency components [58, 59].

2.2.3 Lamb-Oseen vortex

The Lamb-Oseen vortex provides an exact solution to the 2D incompressible Navier-Stokes equations, in the form of a line vortex decaying in time under the action of viscosity. The velocity is quantified with Equation 2.29 where Γ is the vortex's circulation, r is the radial coordinate and r_c is the core radius also represented as a function of viscosity, ν, and time, t [60, 61]. The Lamb-Oseen velocity profile is shown in Figure 2.11a and Figure 2.11b shows how the velocity profile varies with the core radius. As expected from Equation 2.29, all velocity profiles decay at a similar rate of $1/r$ when r becomes much larger than the core radius. The core radius also determines the location of the peak velocity as well as the rate at which this peak is reached.

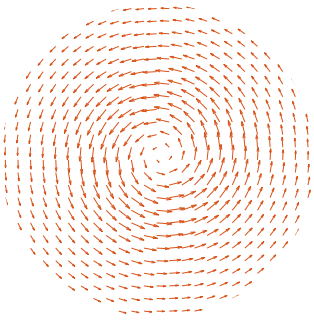

(a) Lamb-Oseen vortex velocity vectors

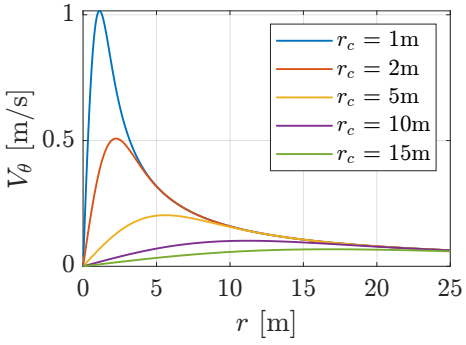

(b) Tangential velocity with core radius.

Figure 2.11: Lamb-Oseen vortex.

$$V_\theta(r,t) = \frac{\Gamma}{2\pi r}\left(1 - e^{-\frac{r^2}{r_c^2}}\right) \quad \text{with} \quad r_c = 2\sqrt{\nu t} \tag{2.29}$$

Although the maximum tangential velocity does not occur at the core radius exactly, it does occur relatively close to it.The derivative of the velocity profile in r is given in Equation 2.30. Finding the roots of this equation will lead to the radial position corresponding to the maximum velocity of the Lamb-Oseen vortex. The derivative cannot be expressed in terms of r and therefore needs to be solved numerically. This may then be used to tune the circulation in order to achieve the desired induced velocity.

$$\frac{dV_\theta}{dr} = \frac{\Gamma}{2\pi}\left(-\frac{1}{r^2} + \frac{1}{r^2}e^{-\frac{r^2}{r_c^2}} + \frac{2}{r_c^2}e^{-\frac{r^2}{r_c^2}}\right) \tag{2.30}$$

2.2.4 Wind turbine wake

As wind turbines extract energy from the incoming flow, a lower energy content is expected in the resulting wake flow, which is generally associated with a velocity deficit and increased turbulence. The wake region may be subdivided into characteristic parts as shown by Figure 2.12. A *transition* region may also sometimes be defined as the region in between the near and far wake regions. The near wake region, typically 1 to 4 rotor diameters long, still exhibits evidence of the rotor [62, 63]. Indications of the number of blades, aerodynamics of the blades, tower and nacelle or even operating parameters of the wind turbine may all be related to the flow observed within this region. The far wake region displays less influence from the rotor and is mostly affected by the global environmental conditions as larger flow structures are broken down to small scale and the wake deficit is recovered through turbulent dissipation, or the mixing and interaction of eddies [63, 64].

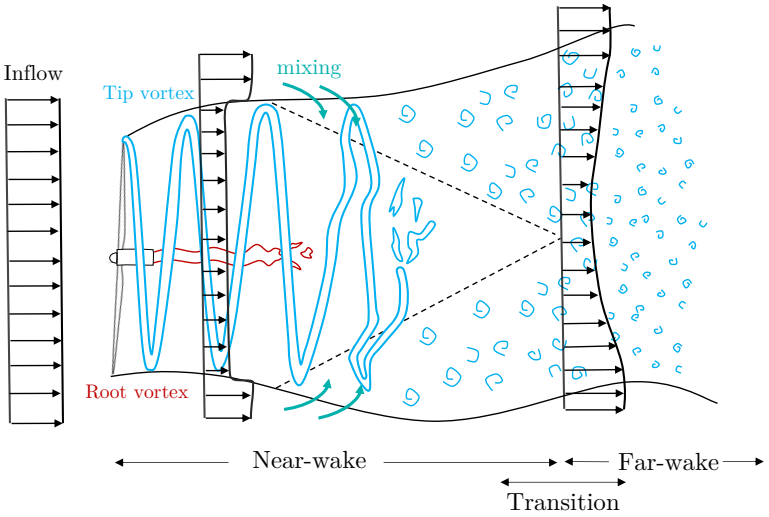

Figure 2.12: Top view of wake behind single turbine. Inspired and adapted from [63, 65].

The main aspect of interest for this study are the helical vortices created at the blade tips and roots, present in the near wake region. In a similar way to aircraft tip vortices, the pressure difference between the two sides of the blade cause air to flow from the high pressure (pressure side) to the low pressure (suction side), thus inducing a velocity component along the blade and orthogonal to the streamwise flow. The structure of these helical vortices can be generalised as a system of vortices or vortex sheet as shown in Figure 2.13. Each blade consists of a similar vortex sheet with a bound circulation distribution arising from the flow over the aerofoil profile, trailing vortices from the span-wise variation in bound circulation and shed vortices from the time variation in bound circulation. The root and tip vortices close the system, following Helmholtz's second theorem, vortex filaments may not end in a fluid and should form a closed path or extend to the boundaries of the fluid.

During the transition from near to far wake, the vortices start interacting with one another, which eventually leads to the decay of turbulent scales [66]. The process arises from the mutual inductance between vortex pairs, in a similar way to the well-known leap-frogging phenomenon [67, 68]. This development, combined with ambient turbulence creates a more and more chaotic system, eventually resulting in the full break down of the helical vortices and gradual wake recovery from turbulent mixing.

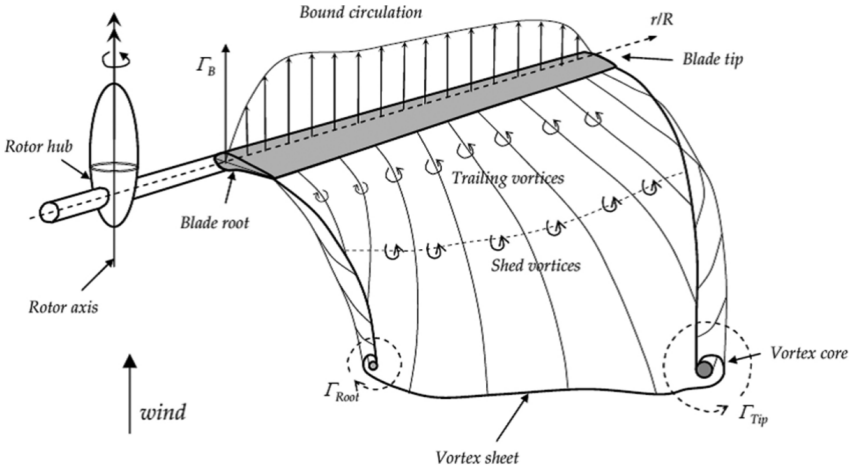

Figure 2.13: Wind turbine blade vortex sheet. Obtained from [69].

3

Lidar modelling

The lidar model will be presented within this chapter, including its features and the selected modelling approaches. Verification tests are shown for various conditions and for different outputs of the model. The final part will present lidar tests realised in different configurations for shear profiling as an example case.

3.1 Model overview

Figure 3.1 provides a simple overview of the numerical lidar emulator that has been developed and used to perform the tests and results presented in the later chapters. To further constrain the research scope, only CW lidars have been modelled, although the model can easily be extended to pulsed lidars as well. The general structure of the model can be captured with the following four key points:

1. Selecting lidar properties and model settings
2. Creating a set of sampling points with assigned weights
3. Obtaining wind field at sampling points
4. Computing outputs (V_{LOS}, Doppler Spectra, etc.)

The first step involves providing the model with a number of user defined inputs that characterise the lidar. Pre-defined lidars such as WindVISION and ZXTM models have been included, however, one may also chose to define a new lidar by selecting the number of beams, the shape or type of beam and certain beam characteristics: Rayleigh length, wavelength, focus range, inclination angle, azimuth angle.

Secondly, the lidar beams are initialised based on the previous inputs. A set number of sampling points are generated in space, representing the position of a light scattering aerosol. The arrangement of the sampling points are chosen with the type of beam selected, which vary in how they approximate the lidar beam. Additionally, every sampling point is

assigned a weight, representing its contribution to the backscattering as will be explained in section 3.2.

The third block involves the simulation of the wind field, which is not a part of the lidar model and can be symbolised as a black box that provides a full wind vector at every sampling point for a desired flow field type.

Finally, the fourth part computes the outputs necessary, such as line-of-sight velocity, Doppler spectrum or even, power and phase spectra. The V_{LOS} computation block includes the implementation of two different modelling approaches for V_{LOS} and Doppler spectrum estimation, which will be detailed in section 3.3.

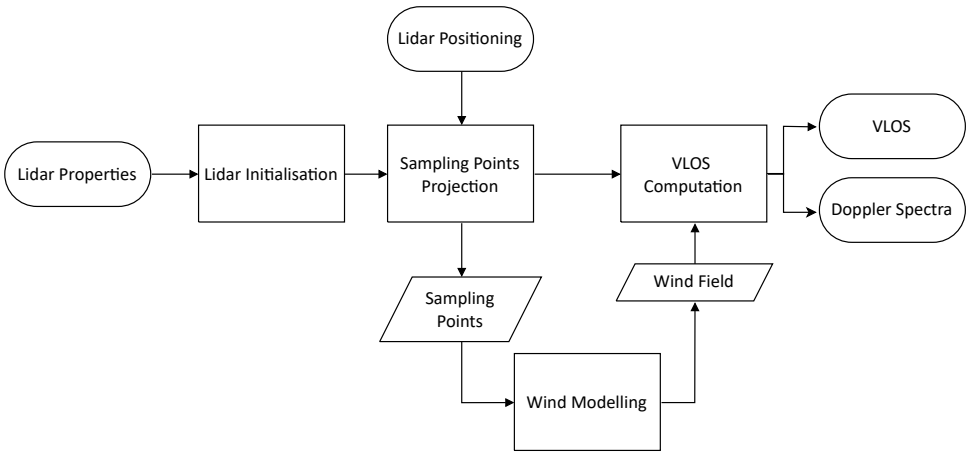

Figure 3.1: Overview of lidar model.

3.2 Lidar initialisation

The following section details the lidar initialisation and particularly the different type of beams implemented within the model. The idea of implementing various beams was to offer a compromise between computational cost/accuracy and more realistic modelling assumptions as will be shown in subsection 3.2.3. Figure 3.2 gives a picture of the lidar properties and initialisation details and how this links to the remaining parts of the model.

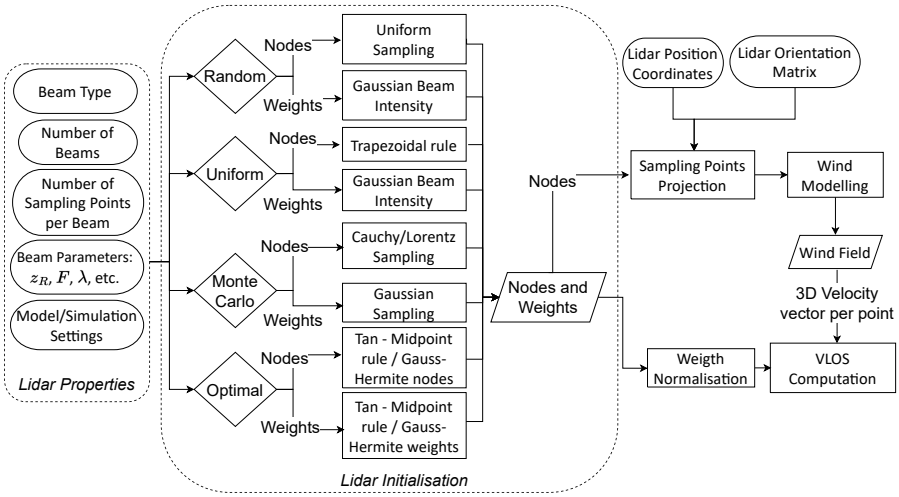

Figure 3.2: Block diagram of lidar beam initialisation.

As described in section 2.1, a convolution integral needs to be evaluated in order to compute the line-of-sight velocity at the measurement point. This requires the use of numerical integration methods or quadratures which may have the objective of minimising the numerical error for a given number of sampling points (N), translating to lower computational effort. In the discrete form, the convolution can be described by Equation 3.1, with the weighting function $W(s)$ being dependent on the lidar type and level of approximation. The following sections will outline the different numerical methods that will be applied to the various weighting functions tested.

$$V_{LOS}(F) = \int_{-\infty}^{\infty} W(s) V_{LOS}(s) ds \approx \sum_{i=1}^{N} w_i V_{LOS}(s_i) \tag{3.1}$$

3.2.1 Lorentzian

Making the assumption of negligible radial variation in the Gaussian beam, leaves the intensity as a function of the axial Lorentzian or Cauchy profile. This is typically applied to CW lidars (Equation 2.17) and is simplified here as Equation 3.2 in order to test different quadratures. A test function is used to represent the line-of-sight velocity function and is chosen such that an analytical expression can be obtained for the integral, as seen from Equation 3.3. This function does not represent a realistic flow field but serves as a mean to verify if the implementation of the numerical method is correct.

$$W(x) = \frac{1}{1+x^2} \tag{3.2}$$

$$I = \int_{-\infty}^{\infty} \frac{1}{1+(x+3)^2} W(x)dx = \frac{2\pi}{13} \tag{3.3}$$

Four different integration methods have been implemented and are presented in the following sections. A comparison of the convergence of each technique is presented in Figure 3.4.

3

Uniform spacing

A direct and easy approach to solving the integral in Equation 3.3 is to discretise the domain and apply Newton–Cotes rules such as the trapezoidal rule: $\sum_{i=1}^{N-1} \frac{f(x_{i+1})+f(x_i)}{2}\Delta x$. Discretising the integral in Equation 3.3 into uniform intervals requires to choose finite bounds to the integral. This is however not a straightforward choice and has a large effect on the error. As seen from Figure 3.3a, setting smaller and more restrictive bounds for the integral 'cuts' a larger portion of the curve and hence results in part of the area to be ignored. However, for a given number of points N, a smaller integral range allows to divide the domain into smaller intervals and in this case obtain a better representation of the function. This translates into the convergence plot shown in Figure 3.3b. For larger limits, the minimum error is lower but it takes more points for the error to start decreasing compared to smaller limits. Notice also that the methods scale with N^{-2} as a result of the trapezoidal rule.

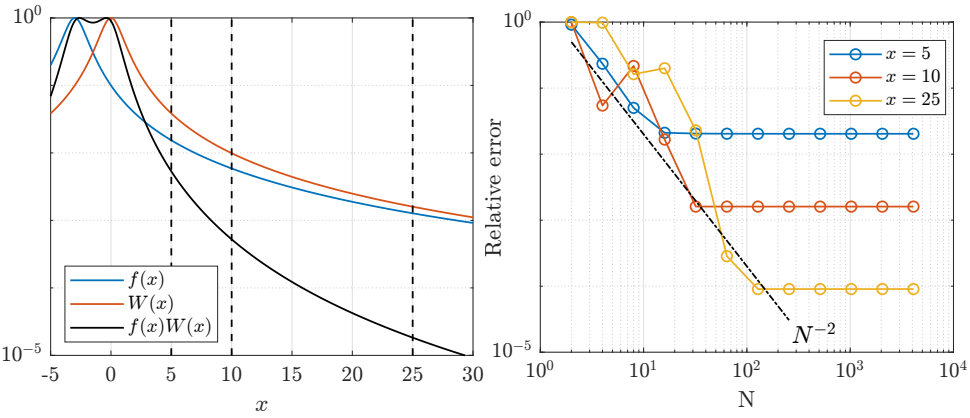

(a) Integrand function with varying limits.

(b) Convergence for varying limits.

Figure 3.3: Effect of finite integral limits on convolution.

Tan substitution

The approach presented here makes use of substitution in order to map the integral domain from an infinite one to a finite one. The substitution $x = \tan(\theta)$ is made an shown by Equation 3.4.

$$I = \int_{-\infty}^{\infty} \frac{f(x)}{1+x^2}dx = \int_{-\frac{\pi}{2}}^{\frac{\pi}{2}} \frac{f(\tan(\theta))}{1+\tan(\theta)^2}\sec^2(\theta)d\theta = \int_{-\frac{\pi}{2}}^{\frac{\pi}{2}} f(\tan(\theta))d\theta \tag{3.4}$$

From this resulting integral, several different methods can further be applied to compute the discrete sum. The first method applied is simply the midpoint rule: $\sum_{i=1}^{N} f(x_i)\Delta x$, with uniformly spaced nodes in $\left[\frac{\pi}{2}, -\frac{\pi}{2}\right]$. Another option is to make use of Gaussian quadratures. As there does not exist one specifically for the Lorentzian profile over an infinite domain the option is then to apply Gauss-Legendre quadrature shown by Equation 3.5 to the finite approximation of the integral in Equation 3.4. The nodes (x_i) are now defined by the roots of the nth order Legendre polynomials (P_n) and are scaled onto the desired domain. The weights w_i are obtained as shown by Equation 3.5 [70].

$$\int_{-1}^{1} f(x)dx \approx \sum_{i=1}^{N} w_i f(x_i) \quad \text{with} \quad w_i = \frac{2}{\left(1-x_i^2\right)\left[P_n'(x_i)\right]^2} \tag{3.5}$$

Monte Carlo - Cauchy

The final method tested here is Monte Carlo integration and consists of selecting nodes that are distributed according to a chosen probability density function. In the case of the Lorentzian weighting function, sampling from the Cauchy distribution (also known as Lorentz distribution) is ideal. Equation 3.6 shows the probability density function the points are sampled from. The function is then evaluated at these points and the summation of all contributions is done. Notice how there are no weighting terms in the sum as the weighting function effects are entirely dictated by the node placement. For the Lorentzian in the form of Equation 3.2, points are sampled from the Cauchy distribution with the following scale (γ) and location (x_0) parameters: Cauchy$\left(x_0 = 0, \gamma = 1\right)$. Additionally, this approach, also makes use of the tan mapping, as in order to generate Cauchy distributed samples, uniform samples u_i are first obtained on the domain $[0, 1]$ and are then mapped with $x_0 + \gamma\tan(\pi u_i - \pi/2)$).

$$I \approx \frac{1}{N}\sum_{i=1}^{N}(X_i) \quad \text{with} \quad pdf(X_i) = \frac{1}{\pi\gamma\left[1+\left(\frac{X_i - x_0}{\gamma}\right)^2\right]} \tag{3.6}$$

Figure 3.4 shows the performance of the different numerical integration methods previously presented. As expected, the uniform method levels off after reaching a certain error limit, Monte Carlo integration follows the $1/\sqrt{N}$ convergence rate quite well and the quadratures used in combination with the tan substitution display spectral convergence or increasing rate of convergence. This is dictated by the mapping to a finite domain as the use of Gauss-Legendre did not improve convergence.

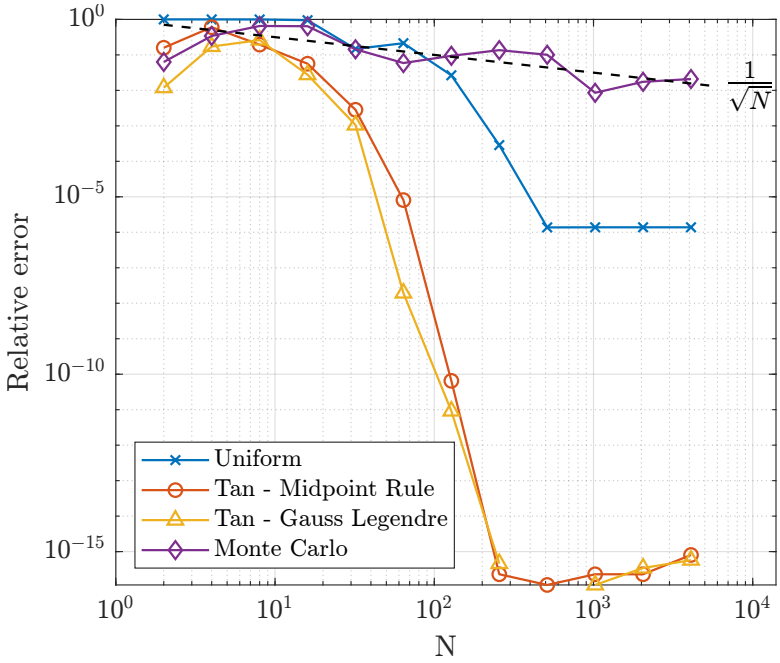

Figure 3.4: Comparison of quadratures applied to the Lorentzian weighting function convolution.

3.2.2 Gaussian

In a similar way to what was shown in subsection 3.2.1, ignoring axial variations in the Gaussian beam this time, the weighting can now be represented as a radial function of the Gaussian profile, Equation 3.7. The test function used here is shown by Equation 3.8 and similar quadratures to those used for the Lorentzian weighting function are tested, namely, the uniform, Monte Carlo and Gaussian quadratures. The uniform quadrature is not detailed but in an identical way to previously shown, the integrand is 'cut' to obtain finite integral bounds.

$$W(x) = e^{-x^2} \tag{3.7}$$

$$I = \int_{-\infty}^{\infty} \cos(x) W(x) dx = \sqrt{\pi} e^{-\frac{1}{4}} \tag{3.8}$$

Monte Carlo - Gaussian

A slight modification can be made to apply Monte Carlo to the Gaussian weighting. Sampling from a normal distribution with specified mean (μ) and standard deviation (σ), $X_i \sim \mathcal{N}(\mu = 0, \sigma = \sqrt{1/2})$, is ideal to describe the Gaussian weighting function, as the probability density function is given by Equation 3.9. The summation process remains the same, and once again, there exists a mapping step from uniformly generated samples to normally distributed ones. Drawing uniform samples u_i, the normally distributed samples are given by $X_i = \mu + \sigma\sqrt{2}\text{erf}(2u_i - 1)$, thus mapping from [0,1] to $[-\infty, \infty]$.

$$pdf(X_i) = \frac{1}{\sigma\sqrt{2\pi}} e^{-\frac{1}{2}\left(\frac{X_i-\mu}{\sigma}\right)^2} \tag{3.9}$$

Gauss-Hermite

There exists various Gaussian quadratures, adapted to different weighting functions and different integral limits. In the case that the integrand compromises of a Gaussian type profile or that the integral bounds are infinite, the Gauss-Hermite quadrature rule is most suited. The nodes are obtained by finding the roots of the physicist's Hermite polynomial (H_n) and the weights with Equation 3.10 [70].

$$\int_{-\infty}^{\infty} f(x)e^{-x^2}\,dx \approx \sum_{i=1}^{N} w_i f(x_i) \quad \text{with} \quad w_i = \frac{2^{n-1}n!\sqrt{\pi}}{n^2\left[H_{n-1}(x_i)\right]^2} \tag{3.10}$$

Figure 3.5 compares the convergence of the different quadratures implemented. Similar trends to what was observed with the Lorentzian weighting function can be seen here as well, such as the $1/\sqrt{N}$ convergence rate of the Monte Carlo quadrature and the initially slow and then faster convergence of the uniform quadrature depending on the integral limits. As one can expect, the Gauss-Hermite quadrature converges the quickest as it is specifically made to efficiently integrate functions multiplied with an exponential weighting function.

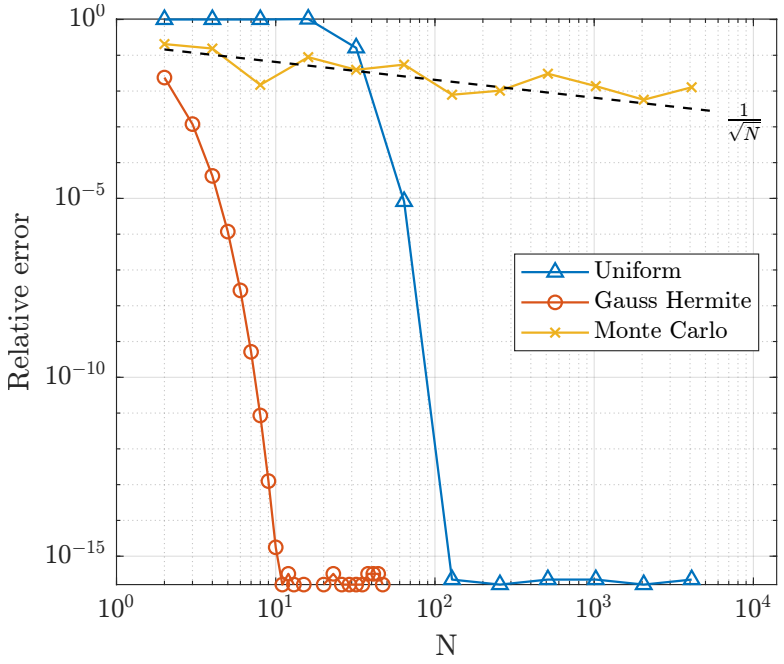

Figure 3.5: Comparison of quadratures applied to the Gaussian weighting function convolution.

3.2.3 3D Beam quadratures

Now that various methods have been tested to integrate separately the Lorentzian and Gaussian weighting functions in 1D, they can now be extended to the combined weighting function or Gaussian beam intensity profile given by Equation 3.11 (equivalent to Equation 2.12 and Equation 2.13). Furthermore, the procedure is now applied in a 3D domain as the weighting is a function of x, y and z (sometimes combined as r).

$$I(x,y,z) = \frac{2P}{\pi w(x)^2} e^{-\frac{2(y^2+z^2)}{w(x)^2}} \quad \text{with} \quad w(x) = w_0 \sqrt{1+\left(\frac{x}{z_R}\right)^2} \tag{3.11}$$

The quadrature methods tested for the Lorentzian profile are applied along the axial direction and those for the Gaussian profile applied in the radial direction. The convergence properties of each quadrature method that were previously identified are matched with one another. This means that for an optimal or fast convergence, a combination of the Tan-Midpoint rule and Gauss-Hermite quadratures is selected. It is also natural to combine the Monte Carlo methods with one another, as well as the uniform methods too. Finally, a new type of quadrature is also introduced in the form of a random approach. This does not deviate much from the Monte Carlo approach but instead of sampling from Lorentzian and Gaussian probability distributions, uniform distributions are used both radially and axially. Figure 3.6 shows the sampling points generated from the four type of beams that were implemented inside the lidar model. The optimal beam shown in Figure 3.6a is fully determined by the quadrature method selected, meaning that nodes and weights are entirely defined from the quadrature method. This is also the case for the Monte Carlo beam shown in Figure 3.6b where the nodes follow the Lorentzian/Cauchy distribution axially and the normal distribution radially, and all weights being equivalent. Finally Figure 3.6c and Figure 3.6d show the uniform and random beams respectively. In both cases, the weights are determined by computing the Gaussian beam intensity (Equation 3.11) at every point. A summary of the beams and corresponding quadratures is given in Table 3.1 and can also be viewed in Figure 3.2.

Table 3.1: Overview of beam types and quadratures implemented.

Beams	Axial Quadrature (x)	Radial Quadrature (r or y,z)
Optimal	Tan-Midpoint rule	Gauss-Hermite
Monte Carlo	Monte Carlo - Cauchy	Monte Carlo - Gaussian
Uniform	Uniform trapezoidal rule	Uniform trapezoidal rule
Random	Monte Carlo - Uniform	Monte Carlo - Uniform

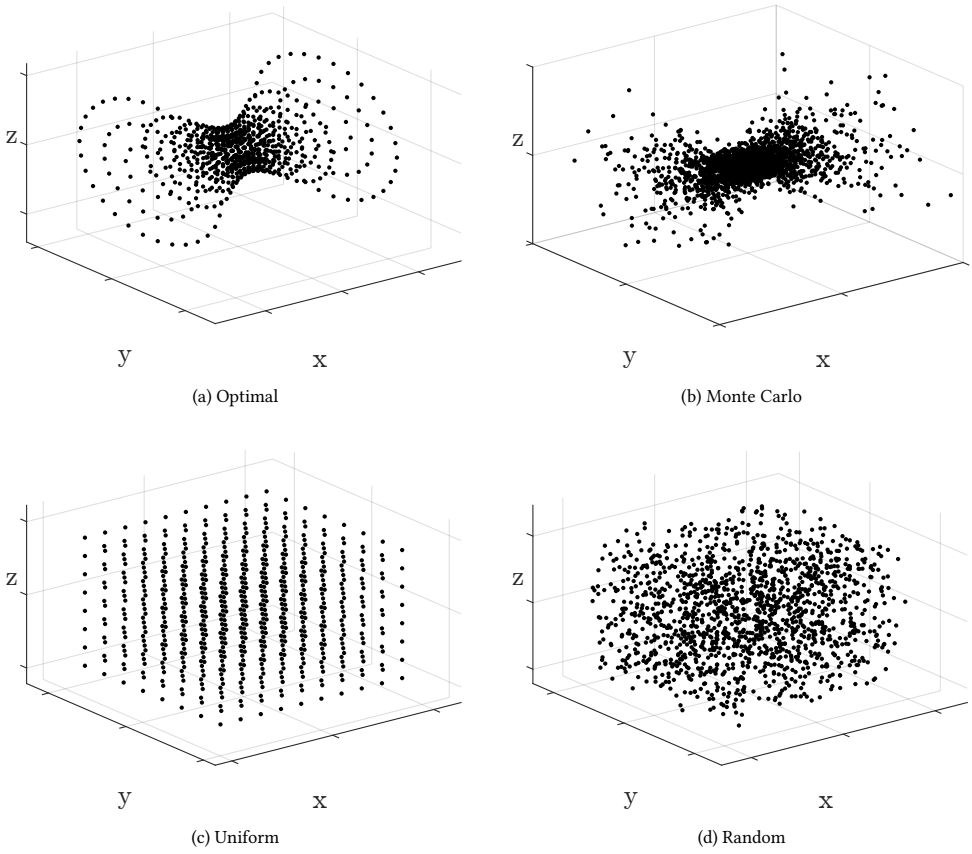

(a) Optimal

(b) Monte Carlo

(c) Uniform

(d) Random

Figure 3.6: Lidar sampling point distributions.

For all beams, the weights are normalised and it should be remembered that the quadrature nodes are scaled to correct for the Gaussian beam parameters such as the Rayleigh length and the beam waist. For example, the shape factor of the Lorentzian can be compared to the Rayleigh length of the lidar. Another noteworthy aspect is that the uniform and random beams are both finite, as they are based on finite approximation of the integrals. Thus, both of these beams need to be limited in space by setting bounds, for example as a function of the Rayleigh length axially and the beam waist radially.

All of these beams are the model's representation, with different levels of approximation, of the position of aerosols in the air. In parallel, the associated weights aim to model the intensity of the backscattered light signal received from each aerosol. However, this modelling approach is entirely based on the Gaussian beam and thus only takes into account the shape of the light emission or how much light reaches a particular point in space. In actual lidar operation, the functions may ideally approach the theoretical ones but there are other physical aspects that alter this reality. This may for example be due to variations in the aerosol backscatter. Different aerosols may backscatter the light with different intensities, based on their individual characteristics, and hence bear a different contribution

to the V_{LOS} estimate. A more physical model can therefore be to construct the weights based on the Gaussian beam and in a second stage modify these weights by incorporating effects that affect an aerosol's scattering properties, such as density or size. As this can extend quite deeply into the physics of light scattering and atmospheric sciences, only one effect has been implemented and is presented below.

Particle size effect

The intensity of backscatter is naturally dependent on the emitted signal but also on the aerosols properties as previously described in subsection 2.1.3. Mie scattering is sensitive to certain aerosol properties such as particle size, shape or refractive index [37] and hence affect the contribution to the detected signal. Incorporating these parameters into the weighting of the V_{LOS} convolution increases the noise of the data but aims to better approximate real conditions. An extensive amount of research and effort can be put into detailed modelling of Mie scattering, however as this is not the main scope of research here, this has been limited and simplified solely to the effect of particle size or diameter.

As found in [71, 72], the level of backscattering in the Mie scattering regime can be related to the square of the particle diameter. The subsequent step is then to assign a certain diameter to each modelled particle. The weight of each particle is initially obtained from one of the methods presented above and is then modified by the square of the particle diameter such that the size of a particle affects its contribution to the V_{LOS} weighting. The diameter of a particle follows a log-normal distribution ($d_p \sim \mathrm{Log}-\mathcal{N}(\mu,\sigma)$) with probability density function defined by Equation 3.12, median particle diameter d_{p_m} and standard deviation σ_{d_p} [73].

$$pdf(d_p) = \frac{1}{d_p \sigma \sqrt{2\pi}} \exp\left(-\frac{(\ln(d_p)-\mu)^2}{2\sigma^2}\right) \quad \text{with} \quad \mu = \ln(d_{p_m}) \quad \sigma = \sigma_d \tag{3.12}$$

3.3 V_{LOS} computation

Once the sampling points, weights and velocities are known, one can compute the line-of-sight velocity. For this, two different approaches have been implemented in parallel within the model as shown in Figure 3.8. The first approach, given in blue in Figure 3.7 and Figure 3.8, is generally viewed as the standard approach to lidar modelling and only models the final part of the lidar measurement process. This process is shown in Figure 3.7, and only the Doppler spectrum and the V_{LOS} estimate are modelled, with a set of weights and velocities.

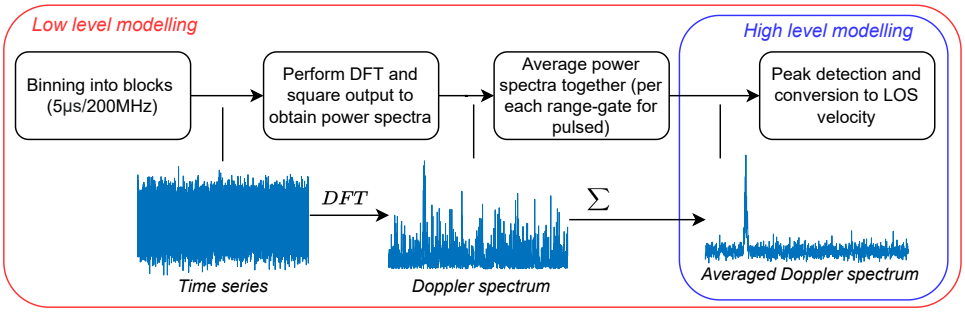

Figure 3.7: Lidar measurement process and modelling approaches. Adapted from [8].

The second approach, given in red in Figure 3.7 and Figure 3.8, offers a different and perhaps unconventional way of modelling the lidar. This models the entire lidar measurement process of Figure 3.7, making use of the weights, velocities and sampling points to simulate the light intensity time series signal received by the lidar detector. The full data processing chain: binning, DFT, averaging can then be applied to obtain the Doppler spectrum and V_{LOS} but also the intermediate outputs such as the power or phase spectra. Both approaches are detailed in section 3.4 and section 3.5 and include verification tests on synthetic wind fields.

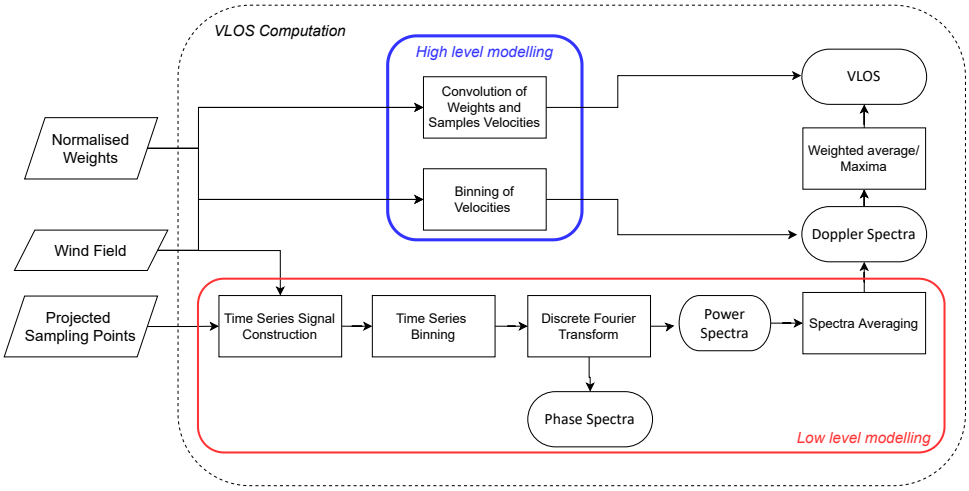

Figure 3.8: Block diagram of V_{LOS} computation.

3.4 High-level modelling

The 'high-level' approach consists on directly modelling the line-of-sight velocity and ignores the real lidar data processing that is typically applied to the recorded backscattered signal. As this approach relies heavily on the weights assigned, the calculations to obtain

V_{LOS} is rather simple and involves a weighted sum of the velocities measured at every sampling point and is given by Equation 3.1. In order to obtain the Doppler spectrum, one can work backwards through the lidar processing, and make use of the weights as the columns or counts of the Doppler spectrum histogram. Each line-of-sight velocity is categorised into bins of $0.15\,\mathrm{m\,s^{-1}}$, ranging from $0\,\mathrm{m\,s^{-1}}$ to $38\,\mathrm{m\,s^{-1}}$, corresponding to a 512-point (double-sided) DFT and 100 MHz sampling rate. These are typical continuous wave lidar settings but may also be user specified inputs to the lidar model. The weights of each binned velocity are then summed to build the histogram counts. In the following parts some exemplary verification tests with simple wind fields, comparing both line-of-sight velocity and Doppler Spectra obtained for various beam types will be presented.

3.4.1 Line-of-sight velocity

Uniform wind

Figure 3.9 shows the successive error in line-of-sight velocity estimates with increasing number of sampling points. The flow field is uniform, meaning that all sampling points, or aerosols, have the same velocity, in this case $U_\infty = 10\,\mathrm{m\,s^{-1}}$. Only a single lidar beam is used and pointed directly against the flow, hence avoiding any discrepancies due to the line-of-sight measurement. The expected measurement to this case is known here and should be $U_\infty = 10\,\mathrm{m\,s^{-1}}$ as all V_{LOS} measurements are identical and all weights sum to one. As seen from Figure 3.9, all beams converge straight away, showing that the weights are correctly normalised. The increase in error is purely a result of numerical round-off error.

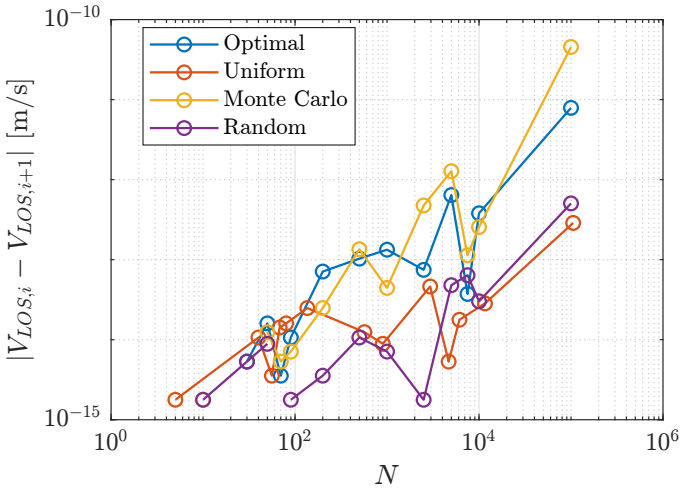

Figure 3.9: Successive error in V_{LOS} for uniform wind field: $V_\infty = 10\,\mathrm{m\,s^{-1}}$

Turbulent wind

Figure 3.10 presents the results with the identical lidar setup to the previous uniform flow field case but this time applied to a turbulent flow field. In this case, the true answer to the convolution integral is not known as each sampling point is assigned a random velocity

deviation from the mean wind speed. The lidar therefore measures an average velocity over the sampling volume. The expected behaviour of the different beams can however be recovered from Figure 3.10a and Figure 3.10b. As seen in section 3.2, the uniform and random beam approximate the infinite integral domain on a finite one and are therefore limited in terms of accuracy by the part of the domain that is ignored or 'cut off' in the approximation. This feature appears in Figure 3.10a with the offset between these two beams and the infinite domain optimal and Monte Carlo beams. With increasing number of points, the optimal beam generally has a lower error magnitude than the Monte Carlo beam and the other two 'finite' beams as seen from Figure 3.10b.

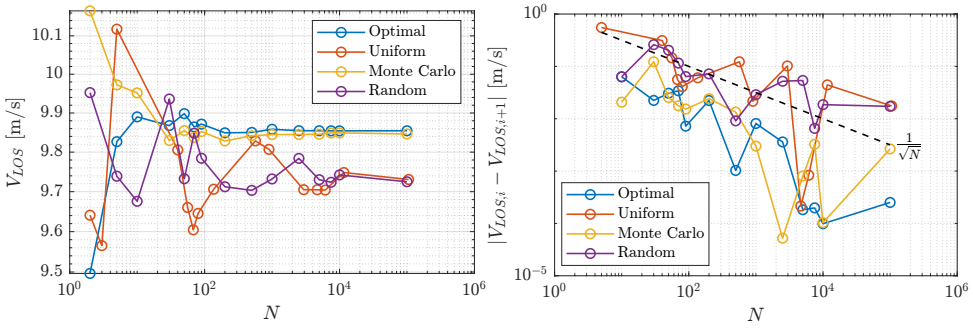

(a) Measured V_{LOS}.

(b) Successive error in V_{LOS}.

Figure 3.10: Beam convergence for turbulent wind field: $V_\infty = 10\,\mathrm{m\,s^{-1}}$,TI = 0.1.

3.4.2 Doppler Spectra

Figure 3.11 shows the Doppler spectra obtained for the four different beam types, with the same number of points, for two different turbulence levels. It should be noted that the Doppler spectra have been generated using 256 (one-sided) bins and the figure only shows the bins of interest, where velocity signals have been detected. The tested wind field is simply modelled with a mean velocity and some normally distributed variations. The turbulence level is varied by changing the amplitude of the variations (increased standard deviation) and this is clearly seen in the range of velocities that occur in the spectra. When comparing the four beam types, one notices that the random beam is most different to the others, it detects more extreme velocity measurements and fairly larger variations in histogram counts between adjacent velocity bins. This is expected as node placement is random and therefore does not capture effectively the range of velocities within the measurement volume. The similarity in the Optimal and Monte Carlo beams seen in the V_{LOS} convergence plot is also seen here, both spectra are quite similar with small discrepancies due to the randomness of the Monte Carlo beam, which will disappear for larger number of sampling points.

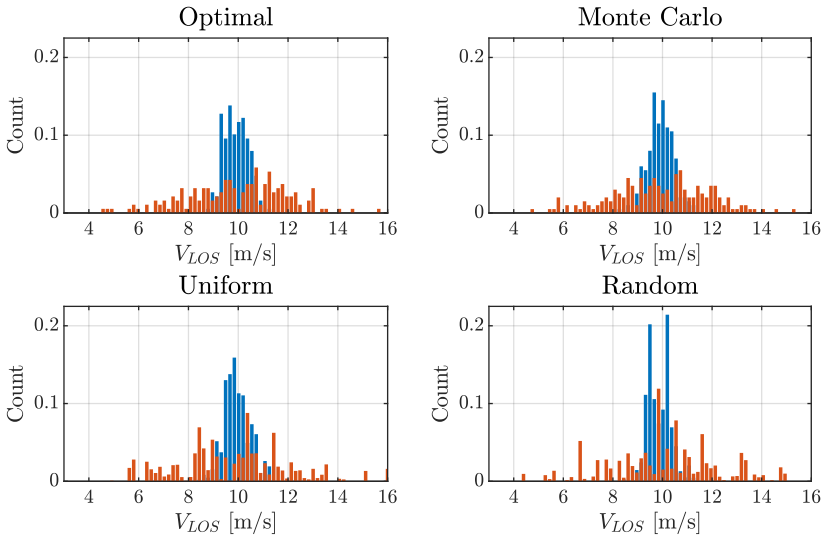

Figure 3.11: Doppler spectra for four beam types at low ( ) and high ( ) turbulence levels. All beams use $N = 200$ sampling points.

Figure 3.12a and Figure 3.12b show the mean and standard deviation estimated from the Doppler spectrum with an increasing number of sampling points. All beams appear to converge but the relative error seems to reach a limit for the estimated mean, which is due to the binning of the velocities. For 256 bins, each bin represents a 0.15 $\mathrm{m\,s^{-1}}$ velocity range which introduces a systematic error in the recorded velocities but may be reduced by increasing the FFT size.

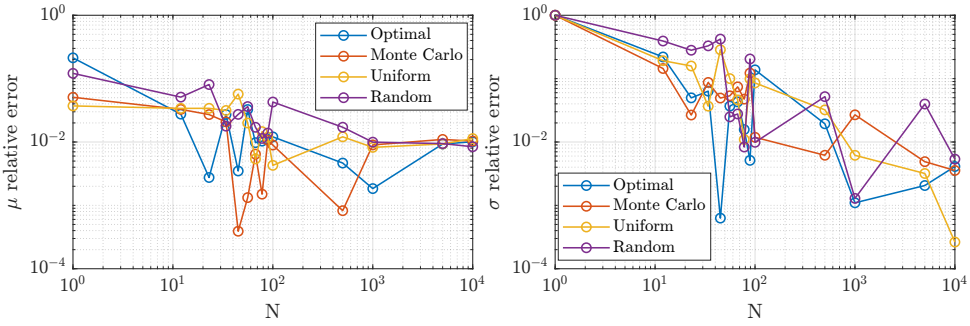

(a) Mean

(b) Standard deviation

Figure 3.12: Doppler spectrum moments convergence ($N_{bins} = 256$).

3.5 Low-level Modelling

The 'low level' modelling approach differs to the 'high level' approach in the part of the lidar measurement process that it is trying to approximate. As the name suggests, this

approach consists on modelling the bottom and initial stage of the measurement process which is the intensity signal recorded by the lidar detector. This intensity time series is modelled by the sum of the backscattered signals from N number of light scattering particles, as shown by Equation 3.13. Each particle is assigned an amplitude A_n, a frequency f_n and a phase ϕ_n.

$$I(t) = \sum_{n=1}^{N} A_n \cos\left(2\pi f_n t + \phi_n\right) \tag{3.13}$$

The amplitude (Equation 3.14) is dependent on the strength of the backscatter signal received from a particular scatterer. This is identical to the modelling of the weights previously presented in subsection 3.2.3 and the amplitude is therefore computed from the intensity distribution of the Gaussian beam, and may optionally include the effect of particle size. As one can expect, Equation 3.15 shows that the frequency of the signal is related to the particle's line-of-sight velocity as explained by the Doppler effect with λ the infrared wavelength of the lidar. Finally, the phase of the particle, ϕ_n is related to the ratio between the lidar-particle distance, r_n, and the wavelength of the beats signal, $\lambda_n = \frac{c}{f_n}$ with c as the speed of light. Note that f_n is the Doppler frequency and equivalent to the beats frequency, which is the difference between the local oscillator frequency and the backscattered frequency as previously shown from Equation 2.15. As this frequency is of the order of 1 to 50 megahertz, depending on V_{LOS}, the beats wavelength is then in the range of 6 to 300 meters. A detailed derivation on how Equation 3.16 is obtained can be found in section A.1 of Appendix A.

$$A_n = W_n \tag{3.14}$$

$$f_n = \frac{2V_{LOS_n}}{\lambda} \tag{3.15}$$

$$\phi_n = \frac{4\pi r_n f_n}{c} \tag{3.16}$$

3.5.1 Time series processing

The typical lidar data processing chain was previously shown in Figure 2.8. Given that the ZXTM CW lidar is quite often used as an example in literature, its data processing parameters have been used as reference here, but may most likely deviate for other lidar models. The measurements are performed at a sampling rate of 100 MHz and the recorded signal is split into blocks of approximately 5 µs. A 512 point DFT is then performed, and this process is then repeated near 4000 times to average each DFT output, giving a final averaged spectrum over 20 ms. Generating this averaged spectrum therefore requires 2,048,000 time samples and becomes computationally expensive and lengthy to simulate for larger number of sampling points. To remedy this, a 20 ms time series is simulated, and a single N point DFT is then performed, resulting in the averaged power spectrum or Doppler spectrum.

In order to accurately recover the frequency and phase, it is important to tune the parameters of the time series, particularly to reduce the effects of spectral leakage. The DFT assumes that the intensity time series is periodic within the measurement time. Due to the wide range of frequencies present within the signal, it is highly unlikely that the signal is perfectly periodic across the measurement time. This introduces discontinuities

in the assumed signal, which are detected by the DFT as a new frequency component that is not part of the physical signal [74]. To solve this issue, several techniques may be applied to improve the recovery of the signal: zero-padding, windowing, using a larger DFT, sampling longer time series. When spectral leakage occurs, frequencies in the adjacent bins to the true frequencies are detected. Although, the true frequencies may be retrieved by interpolating (*sinc interpolation*) the location of the peak, the phase appears to be more strongly affected by the effects of spectral leakage and exhibits large offsets. These offsets may be corrected by interpolation between bins but this initiates large inaccuracies with multiple frequencies. In order to recover accurate phase measurements and move forward of this issue, it is possible to avoid spectral leakage entirely by making sure each velocity falls into a single bin. This may be done by rounding the frequency such that no variation smaller than the bin size is detected. An example of this is given in section A.2 of Appendix A.

When testing these various methods on simulated intensity signals, a combination of a larger DFT size and longer samples resulted in the best phase and frequency recovery. Furthermore, in a similar way to the Doppler spectra obtained in subsection 3.4.2, some accuracy is lost when applying the DFT, as the size of the frequency or velocity bins is set from the size of the DFT and the sampling frequency as shown by Equation 3.17. This means that velocities with a discrepancy of δV_{LOS} or less will be assigned to the same bin.

$$\delta V_{LOS} = \frac{f_s}{N_{DFT}} \cdot \frac{\lambda}{2} \tag{3.17}$$

The DFT returns the complex spectrum which may then be converted to amplitude and phase spectra with Equation 3.18 and Equation 3.19 respectively, whilst also only taking one side of the frequency bins. Additionally, the spectra may then be filtered by setting an amplitude threshold to observe the most relevant frequency and phases. The phase values extracted are observed on $[-\pi, \pi]$ and are then are mapped onto $[0, 2\pi]$.

$$|I(f)| = \sqrt{\mathbb{R}\mathrm{e}[I(f)]^2 + \mathbb{I}\mathrm{m}[I(f)]^2} \tag{3.18}$$

$$\angle I(f) = \mathrm{atan2}\left(\frac{\mathbb{I}\mathrm{m}[I(f)]}{\mathbb{R}\mathrm{e}[I(f)]}\right) \tag{3.19}$$

3.5.2 Doppler spectrum

Figure 3.13a shows the Doppler spectra obtained for both modelling approaches at a turbulence intensity of 0.1. The same is shown in Figure 3.13b for a TI of 0.3, where as expected a wider range of velocities is found and the Doppler spectrum has larger tails. Both spectra have been obtained with a 1000 point DFT in order to get a better V_{LOS} resolution. The blue and red spectra do not show an exact match but the general position of peaks as well as the range of velocities obtained are quite similar. As it is rather difficult to compare this visually, the sample mean and standard deviation for both approaches and cases have been computed, and are shown in Table 3.2.

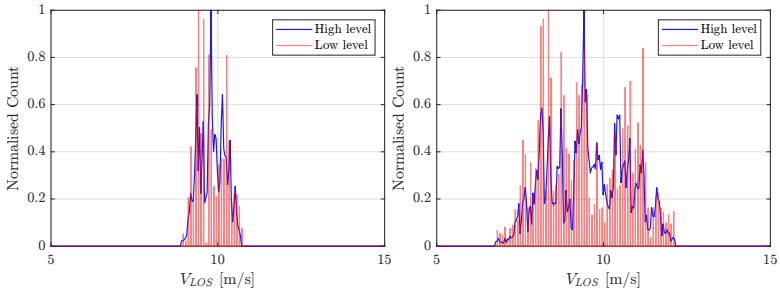

(a) TI = 0.1. (b) TI = 0.3.

Figure 3.13: Doppler spectra comparison for turbulent wind field (U_∞ = 10 m s^{-1}).

The main source of discrepancy between both approaches is due to the phase modelling of the 'low' level approach. In this modelling approach, two scattering particles with identical velocities and different spatial positions will translate to two signals with identical frequencies but different phases. The sum of these two signals is however not discernible by the DFT and interpreted as a signal with a different phase and intensity. The derivation of this is shown in section A.3 of Appendix A. The intensity of the signal is therefore slightly modified, and will turn out to be weaker or stronger depending on the phases corresponding to each frequency. To prove this reasoning, Figure A.5 in Appendix A shows the same result as Figure 3.13 excluding the phase from the signal. Both spectra then look very similar with some very small differences in peak values most likely coming from the rounding step of the 'low' level approach.

Table 3.2: Doppler spectra statistical comparison

	TI = 0.1		TI = 0.3	
	μ	σ	μ	σ
'High' level	9.83 m s^{-1}	0.387 m s^{-1}	9.54 m s^{-1}	1.16 m s^{-1}
'Low' level	9.80 m s^{-1}	0.428 m s^{-1}	9.45 m s^{-1}	1.27 m s^{-1}
Relative Difference	0.382 %	10.8%	0.964%	9.41%

3.5.3 Line-of-sight velocity

Figure 3.14 and Figure 3.15 compare the 'high' and 'low' modelling approaches for the same test shown in Figure 3.10. The overall line-of-sight velocity of the 'low' level approach is estimated by taking a sample mean from the Doppler spectrum histogram. This is represented by Equation 3.20 where H_i is the count per bin and $V_{LOS,i}$ is the line-of-sight velocity of a specific bin.

$$V_{LOS} = \frac{\sum_{i=1}^{N_{bins}} H_i \cdot V_{LOS,i}}{\sum_{i=1}^{N_{bins}} H_i} \tag{3.20}$$

It can be seen that using the 'low' level approach, the line-of-sight velocity also converges for all beams for an increasing number of sampling points and that the trends

previously perceived for each beam type also appear here. A fairly close match is seen between both modelling approaches. The differences once again mainly arise due to the impact of the phase, as previously explained in subsection 3.5.2.

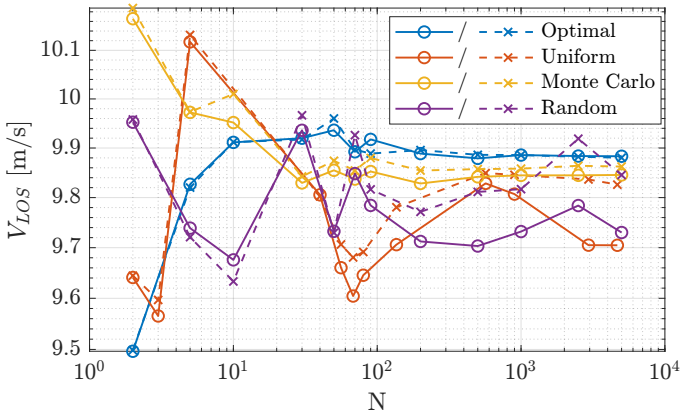

Figure 3.14: Measured V_{LOS} for low level (dashed) and high level (full) approaches on turbulent wind field: $V_\infty = 10\,\mathrm{m\,s^{-1}}$,TI = 0.1.

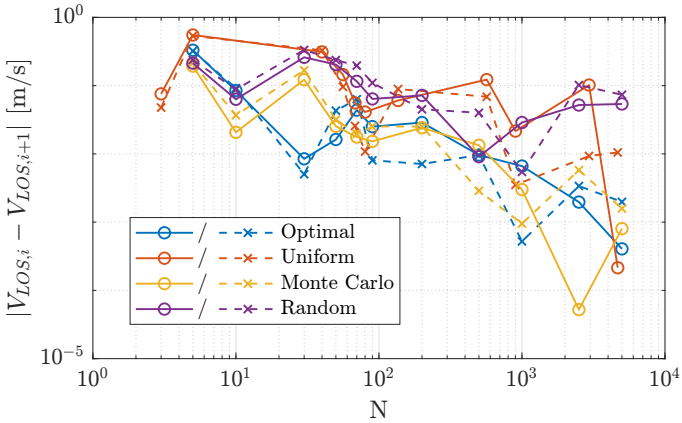

Figure 3.15: V_{LOS} successive error for low level (dashed) and high level (full) approaches on turbulent wind field: $V_\infty = 10\,\mathrm{m\,s^{-1}}$,TI = 0.1.

3.5.4 Phase spectrum

As the 'high' level modelling approach does not model the phase spectrum a comparison cannot be made. Nonetheless, the outputs of the phase spectrum can be analysed in order to investigate if it contains useful information. The most important part of this analysis is to determine from which range does part of the sampled signal come from. Starting back from Equation 3.16, this may be rewritten as Equation 3.21. Thus, the variation of the phase from 0 to 2π depends on the ratio $2d/\lambda_n$. Remember that this is not the same as

λ which is the infrared wavelength of the lidar. In an ideal case, this ratio would remain between 0 and 1, such that the phase cannot repeat itself and that signals from different locations do not produce the same phase. Unfortunately, λ_n is flow field dependent and cannot be controlled. In reality, this ratio therefore varies and phase information may overlap.

$$\phi_n = 2\pi \frac{2d}{\lambda_n} \qquad \text{with} \qquad \lambda_n = \frac{c\lambda}{2V_{LOS_n}} \tag{3.21}$$

One aspect that does not make the phase signal completely chaotic is the Gaussian beam intensity profile. As previously shown, the strongest part of the signal arises from close to the beam waist and the weight of the contributions follow the Lorentzian profile axially. Radial variations also have a small effect but are ignored here for simplicity. This means that if λ_n is in the same order of magnitude as the width of the Lorentzian, one could conclude that the phase measurements relate to the locations that are within the Lorentzian only. As an example, Figure 3.16 shows two different wavelengths λ_1 and λ_2, with $\lambda_1 > \lambda_2$. The points are spaced in intervals of the wavelength, and therefore have the same phase value. This means that when measuring this particular phase value, the signal may be coming from any of the points drawn and hence could correspond to several distance measurements. However, it is possible to use the Lorentzian profile (drawn in black) to help estimate which exact point the signal came from. In the case of λ_1, computing the intensity for each point, the third point will have the highest weight and can be predicted to be the correct point. However, in the case λ_2, the frequency of the wave is too high and the phase measured corresponds to several distances that all have a relatively high likeliness of being from the true signal. There is therefore a strong dependence on the measurement range and measured line-of-sight velocity. At large measurement ranges, the Rayleigh length will be increased, meaning that the Lorentzian will not decay as fast and the signal could arise from a larger region. At high V_{LOS}, the signal frequency is increased and the wavelength is decreased, implying that the phase measurement is repeating too frequently.

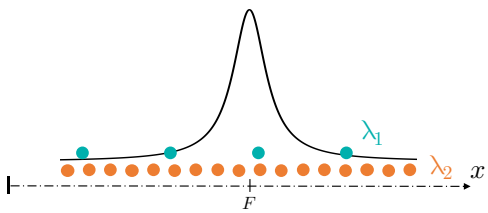

Figure 3.16: Wavelength variation and Lorentzian weighting profile.

Figure 3.17 shows a test case with the velocity profile shown on the left side. The lidar is aligned with the flow field, which only varies along the beam direction (x). The amplitude spectrum shows the expected Lorentzian shape centred around the velocity near the beam focus range (F). The phase spectrum, on the other hand, is quite difficult to interpret as it is.

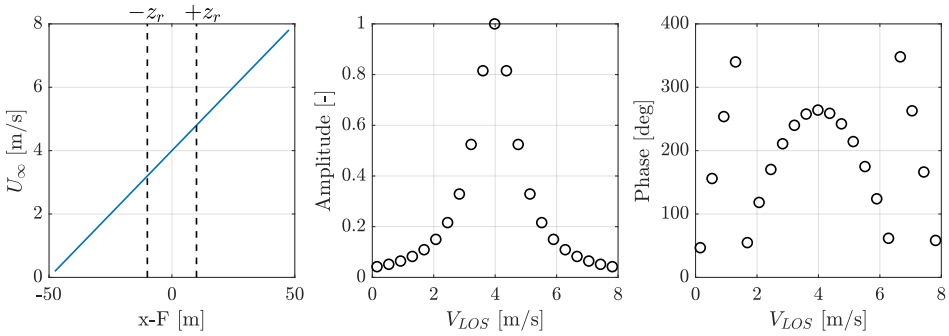

Figure 3.17: Streamwise velocity, amplitude spectrum and phase spectrum.

To extract useful information, the phase may be converted back to distances by rearranging Equation 3.21. As explained previously, the phase may repeat itself as $\phi_n + N2\pi$ with $N = 0, 1, 2..etc..$ When converted to distances, this means the measured distance r_n is actually $r_n + N\lambda_n/2$, the new term being the distance for the phase to reach 2π. Computing the intensity of the Lorentzian for $r_n + N\lambda_n/2$ and choosing N that gives the highest intensity leads to a corrected estimate of r_n. An outline of this exact procedure is shown under section A.4 of Appendix A. Figure 3.18 shows the true velocity profile as well as the velocity profile reconstructed from the phase information. In this particular case, the phase leads to the correct distance information, however this approach becomes unsuccessful and deteriorates under certain conditions. Firstly, as outlined in Equation 3.21, for larger velocity magnitudes, the signal wavelength decreases and the distance cannot be reliably detected anymore. This already occurs close to $5\,\mathrm{m\,s^{-1}}$ in Figure 3.18, after which there is no more certitude on the distance estimate. Secondly, when two different locations have the same velocity, a different phase is recovered which cannot be assigned to either of the original locations. Finally, for longer focal distances, the Rayleigh length will also increase, widening the Lorentzian distribution and once again making the distance estimation much more challenging. Given all these aspects and the additional noise sources and complications of real flow fields, it is difficult to find a suitable and consistent use case for recovering information from the phase.

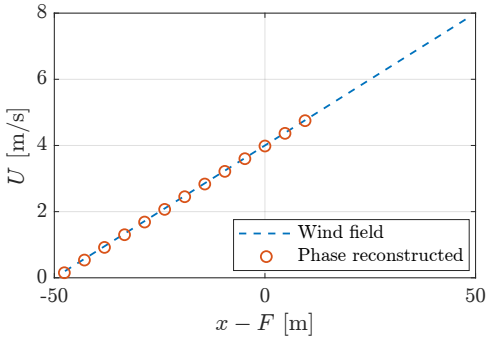

Figure 3.18: True and reconstructed streamwise velocity profile.

3.6 Shear layer test cases

The purpose of this section is to present some application or test cases of the lidar emulator scanning through a vertical wind shear layer. A combination of various conditions and scanning setups are presented. The 'high level' approach of the lidar emulator is used as only line-of-sight velocities are necessary.

3.6.1 Nacelle mounted lidar RHI

Figure 3.19a shows the scanning setup used for the vertical profiling tests shown below. The lidar is located on the nacelle and performs measurements at several heights by varying the inclination angle and the beam focus range. This scanning pattern, consisting of only an inclination angle variation is also named Range Height Indicator or RHI [75]. The measurements are performed at a range of 150 m in front of the lidar and the Rayleigh length is varied according to the range based on the estimated ZXTM attributes [44]. Additionally, note that for simplicity, no blade blockage effects are included here.

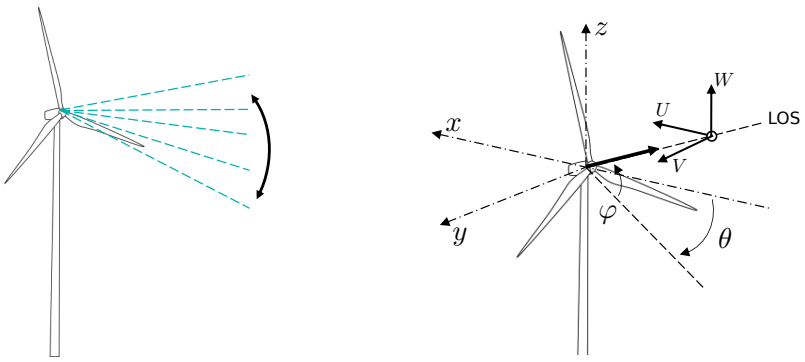

(a) Nacelle mounted lidar vertical profiling.

(b) Line-of-sight projection.

Figure 3.19: Nacelle mounted lidar setup.

When measuring the shear profile, the horizontal component (U) of the wind field is of interest. This component is related to the measured line-of-sight velocity through Equation 3.22, which is simply the projection of the 3D wind field vector onto the line-of-sight direction. An overview of the angles and coordinate system is given in Figure 3.19b, where ϕ and θ are the inclination and azimuth angles respectively. In steady conditions or over long time periods, the U component of the wind field dominates over the V and W components. Thus, these components may be ignored in Equation 3.22, and V_{LOS} may be corrected by the azimuth and inclination angles to obtain a better estimate of U.

$$V_{LOS} = U\cos(\theta)\cos(\varphi) + V\cos(\varphi)\sin(\theta) + W\sin(\varphi) \tag{3.22}$$

Figure 3.20a and Figure 3.20b show the reconstructed horizontal velocity component by correcting the line-of-sight velocity by the inclination angle. Note that the lidar is placed at the hub height of 120 m and therefore has 0° inclination angle for that height. The shear profile is well recovered and the errors appear to increase at higher inclination

angles. This is due to the measurement volume effects. When shining the beam, a greater volume is illuminated after the beam waist than before it. At higher inclination angles, a larger part of the beam will illuminate particles that are at different heights to the intended measurement or focus height. For example, at lower heights, or negative inclination angles, most of the beam is illuminating particles below the focus height. These particles have a lower velocity due to their height and are weighed into the line-of-sight velocity, and hence lower its value. The opposite being true for positive inclination angles, this explains the change of sign of the measured error in Figure 3.20b.

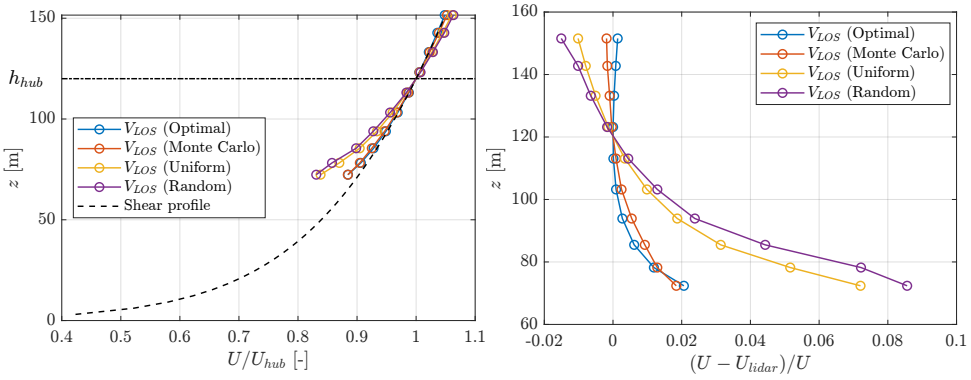

(a) Reconstructed velocity.

(b) Relative error in velocity.

Figure 3.20: Steady shear layer detection from nacelle (α = 0.15).

Figure 3.21 shows the same setup as the previous example, but this time with a turbulence intensity of 0.1. The addition of turbulence clearly induces large discrepancies in the recovered horizontal velocity component. As seen from Equation 3.22, for a non-zero inclination angle, the z-component of the wind field (W) will have a component contributing to the line-of-sight velocity and this is one of the main reasons for the added differences compared to the steady case. Another difference arises from the measurement volume effects, for turbulent wind fields, a larger range of velocities are distributed arbitrarily within the measurement volume. The V_{LOS} detected is therefore not representative of the exact velocity at the intended measurement point. Furthermore,the error increases in Figure 3.21b for the lowest heights as the inclination angle increases and hence sin(φ) as well. Note that the measurement range also has an effect here, should measurements have been performed closer to the lidar, the LOS effects will have been much larger as a larger inclination angle is required to reach the same height measurements.

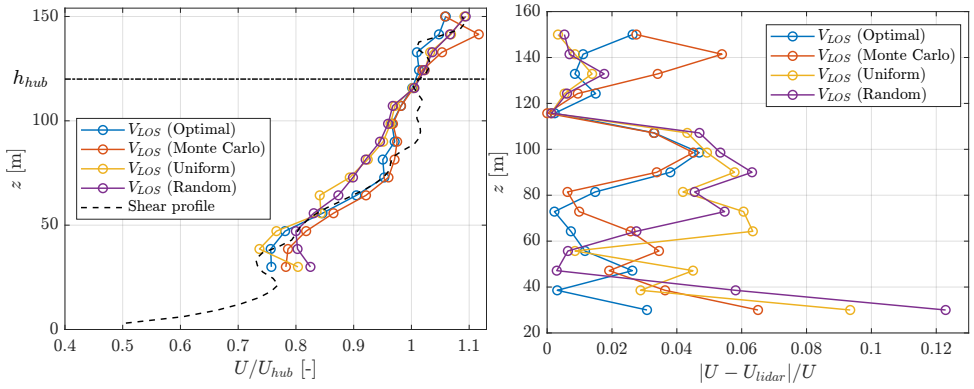

(a) Reconstructed velocity.

(b) Relative error in velocity.

Figure 3.21: Turbulent shear layer detection from nacelle (α = 0.15, TI = 0.1).

3.6.2 Ground lidar VAD

An other technique that can be used to recover the vertical velocity profile is Velocity Azimuth Display (VAD). This consists on measuring the line-of-sight velocity at several points across the same height, distributed around a circle as shown in Figure 3.22, the process is then repeated over multiple heights and concentric circles. The major assumption here is that the horizontal wind velocity remains homogeneous across this circular plane, which is mostly true for flat terrain only [8].

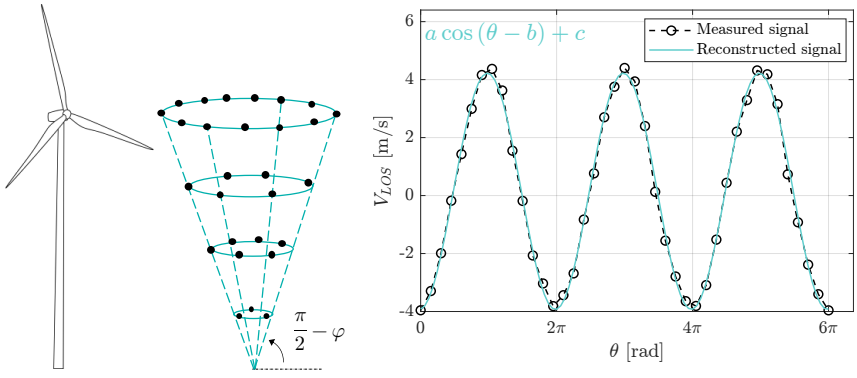

(a) Ground lidar VAD.

(b) Signal reconstruction

Figure 3.22: Velocity Azimuth Display (VAD) setup.

Figure 3.22b shows the measured signal for varying azimuth, in this case resulting in three full revolutions. This signal may then be fitted with a function of the form $a\cos(\theta - b) + c$ [8, 76]. The reconstructed signal is obtained using least-squares regression and is also shown in Figure 3.22b. The individual velocity components may then be retrieved from Equation 3.23. The inclination angle φ may be tuned to obtain a better result. For larger angles, a larger part of the U and V components will be projected along

the line-of-sight, however this will also mean that measurements are performed over a larger circle and that horizontal flow homogeneity may not always be true.

$$U = \frac{a}{\cos\varphi}\cos(b \pm \pi) \qquad V = \frac{a}{\cos\varphi}\sin(b \pm \pi) \qquad W = \frac{c}{\sin\varphi} \tag{3.23}$$

Figure 3.23 shows results of applying VAD to the same turbulent shear layer as Figure 3.21. The errors are also shown in Figure 3.23b. Three azimuthal revolutions with each 40 points were used per height measurement. The Rayleigh length is once again range dependent and based on the ZXTM CW lidar. One can notice in Figure 3.23 that the measured shear profiles appear to be a smoothed out version of the turbulent shear profile. This is due to the averaging effect that occurs when assuming homogeneous horizontal flow over each circle. Comparing the VAD profile to the RHI profile, the magnitude of errors are generally similar. Errors can sometimes remain quite high at larger heights for the VAD setup as the circle of measurement points becomes quite large and the flow homogeneity assumption becomes inadequate. The VAD setup however offers better estimates at lower heights as the LOS effects are quite high for the RHI setup.

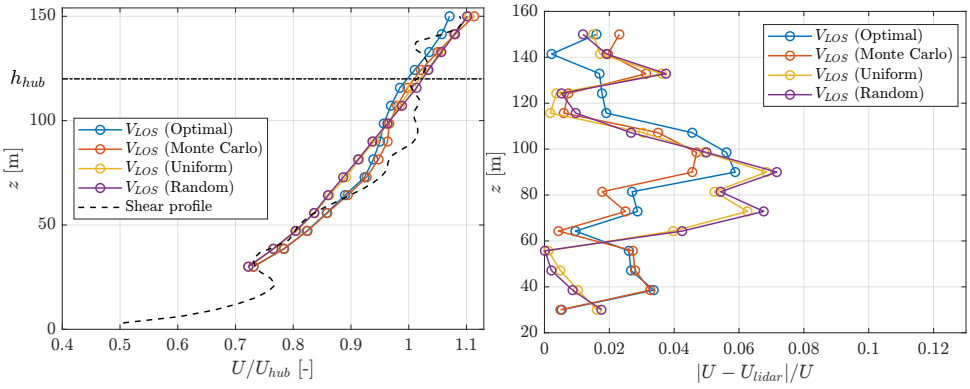

(a) Reconstructed velocity.

(b) Relative error in velocity.

Figure 3.23: Turbulent shear layer detection using VAD (α = 0.15, TI = 0.05).

4

Line vortex identification

The goal of this chapter is to investigate how lidar outputs behave when measuring through a vortex. A standard reference case with a Lamb-Oseen (LO) vortex is setup and the sensitivity of the line-of-sight velocity and Doppler spectrum to a variety of conditions are shown. Several approaches at detecting the position of the vortex core are first compared and attempts at recovering the vortex core radius and circulation are presented for varying conditions.

4.1 Detection

To be able to confirm the presence of a vortex within the flow field, an appropriate starting point is to seek patterns across the available lidar measurement outputs. Firstly, a base case is setup to give an idea of which of these measurement outputs may give an indication of the presence of a vortex. Secondly, the outputs of interest are then computed and analysed for varying setups and conditions to test their sensitivity and validity. Throughout this chapter, the 'high level' model of the lidar is used as the phase output was not investigated.

4.1.1 Case setup

The base case setup has been designed with the idea of reducing the complexity of CW lidar operation. In order to achieve this, a single lidar beam is used and aimed directly forward of the lidar, along the x-axis as depicted in Figure 4.1. Measurement volume effects from the Gaussian beam are present but not dominating as the Rayleigh length has been set to 1.0 m. The additional reason for this is based on the type of parameter space that will be investigated in this section, which are length scale-invariant (either angular or displacement variations). Thus, normalising length scales by the Rayleigh length will scale the entire problem, without altering its physical behaviour and requiring one less parametric investigation.

The Lamb-Oseen vortex is oriented such that it induces velocity in the xy plane only and therefore has its axis in z direction. The vortex is then moved in y direction and cuts across the lidar beam as shown by the black arrow. Note that angle χ is defined here as the angle between the vortex axis and the vertical z axis but is set to zero unless specified otherwise.

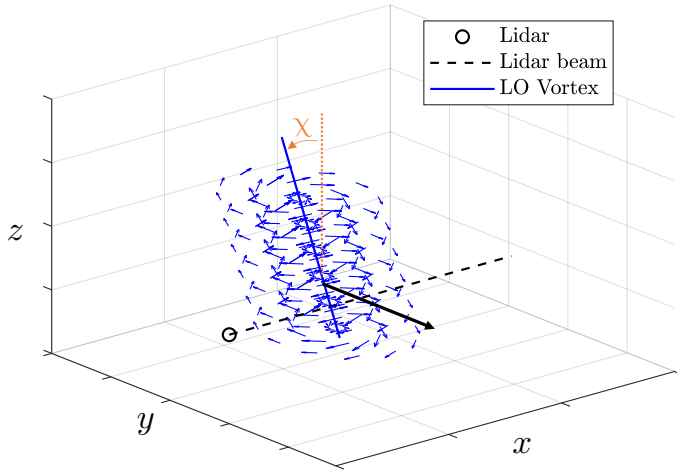

Figure 4.1: Geometry of the case setup.

Table 4.1 shows a summary of the main numerical parameters used for this case. The Lamb-Oseen vortex has a core radius of 1.0 m and a strength Γ set such that the maximum velocity induced by the vortex (max.$V_{\theta,LO}$) reaches 4.0 m s^{-1}. A background wind speed of 10 m s^{-1} is also added in x direction. Figure 4.2 shows the streamwise velocity profile along the x-axis as the vortex is moved in y and effectively shows what velocity field the lidar is measuring across.

Setting	Value
r_c	1.0 m
max.$V_{\theta,LO}$	4.0 m s^{-1}
χ	0.0°
U_∞	10.0 m s^{-1}
z_r	1.0 m

Table 4.1: Vortex and Lidar Settings

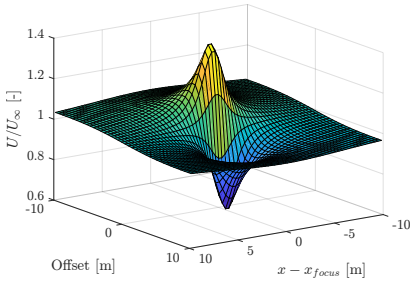

Figure 4.2: Velocity profile across moving vortex.

Figure 4.3 shows the successive Doppler spectra obtained at each offset position. The offset is defined as the position of the vortex core relative to the lidar beam's measurement point. The effect of the vortex is clearly seen by the detected V_{LOS} bins and particularly the increased spread around zero offset. The contour is coloured using the normalised amplitude of the Doppler spectra. Once again, the amplitude is lower around zero offset as the Doppler spectrum is more spread out and the normalised intensity is hence distributed over more bins.

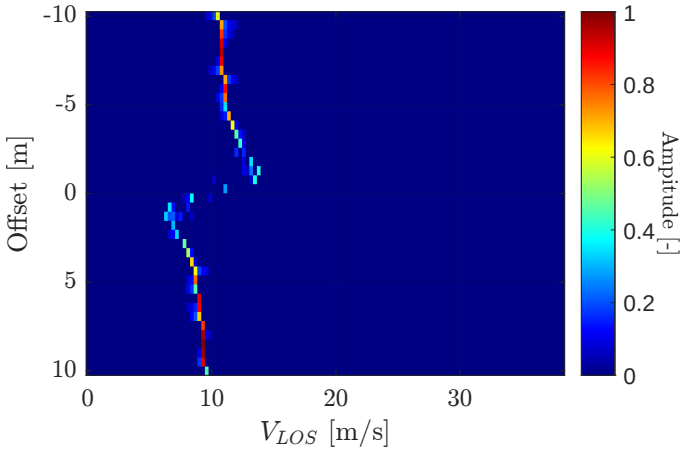

Figure 4.3: Doppler Spectra

From a series of spectra such as the one shown above, it is possible to condense the information into moments or other statistics. The first three moments: the mean, standard deviation and skewness can be computed using Equation 4.1, Equation 4.2 and Equation 4.3 respectively. Once again, H_i is the height of each bin, which is then normalised, and $V_{LOS,i}$ is the corresponding velocity of that bin. Moreover, the sample skewness is estimated using the adjusted Fisher-Pearson coefficient.

$$\mu = \frac{\sum_{i=1}^{N_{bins}} H_i \cdot V_{LOS,i}}{\sum_{i=1}^{N_{bins}} H_i} \tag{4.1}$$

$$\sigma_{DS} = \sqrt{\frac{\sum_{i=1}^{N_{bins}} H_i \cdot \left(V_{LOS,i} - \mu\right)^2}{\sum_{i=1}^{N_{bins}} H_i}} \tag{4.2}$$

$$Sk_{DS} = \frac{N^2}{(N-1)(N-2)} \frac{\sum_{i=1}^{N_{bins}} H_i \cdot \left(V_{LOS,i} - \mu\right)^3}{\sum_{i=1}^{N_{bins}} H_i} \frac{1}{\sigma_{DS}^{3/2}} \tag{4.3}$$

Visualising the statistics of the Doppler spectrum across the lidar scan results in Figure 4.4. The 'Min.' and 'Max.' label signify the minimum and maximum detected velocity past a certain amplitude threshold. Naturally, this threshold is flow dependent and should be set such to include the contributing velocities and exclude arbitrary spikes in velocities that are not representative of the overall flow inside the measurement volume.

One of the key features in Figure 4.4 is the sharp variation in velocity from high to low velocity, also named velocity envelope. As one may expect, this is the effect of the lidar measuring opposite sides of the vortex, which means for the clockwise rotating (negative z direction) setup, positive induced velocities are detected first. The impact of the vortex is not seen for zero offset as along the lidar beam, only perpendicular induced velocities are perceived. Some very minor discrepancies may appear depending on the radial spread of the lidar beam, however this is insignificant when the radial spread is much smaller than the vortex size. Furthermore the differences in peaks of the mean profile and the maximum and minimum profiles develops from the damping of the measurement volume.

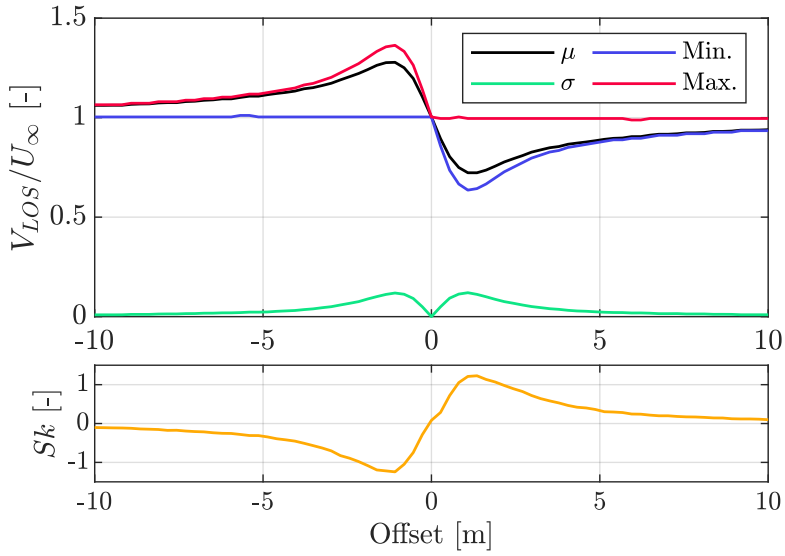

Figure 4.4: Doppler Spectra Statistics

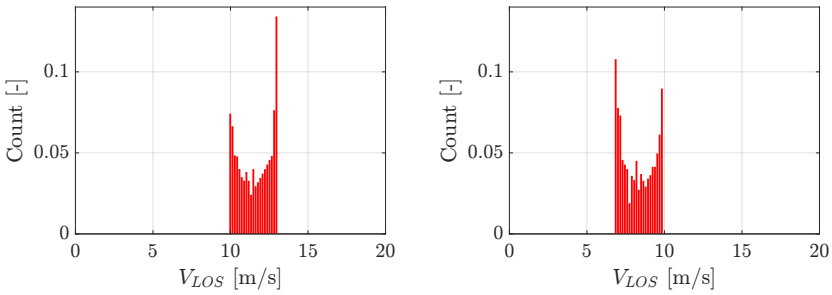

(a) Offset of −1 m

(b) Offset: 1 m

Figure 4.5: Doppler spectra at different offsets.

In terms of statistical moments, it is clear that as the core radius enters the measurement volume, the standard deviation increases as a result of the more varied range of velocities detected. The skewness, which indicates the symmetry of the Doppler spectrum, appears to increase in magnitude and then flip signs when the vortex passes through the measurement volume. A negative skewness factor implies a left-tailed distribution or that the mass of the Doppler spectrum amplitude is concentrated on the right hand side. Similarly, a positive skewness factor suggests a right-tailed distribution and more concentrated mass on the left hand side. This can also be observed on Figure 4.5a which shows negative skew and Figure 4.5b which displays positive skew. The mean velocity does have an effect on the skewness but does not balance out the effect of the vortex. With respect to line-of-sight velocities, this signifies that higher velocities have a larger contribution to

the measurement volume initially (from −10 m to 0 m) but that this then shifts to lower velocities dominating the Doppler spectrum (from 0 m onwards).

Finally, it is important to note that the quantities shown here are well retrieved as the measured signal is quite clean. However, under various conditions, these lines may not appear so distinct, therefore inducing errors in the detection of a vortex. The following sections will aim to investigate how varying certain setup parameters and flow conditions alter the measurements.

4.1.2 Beam focus effects

In this section, the effects of the beam's focusing range are investigated. The distance between the vortex centroid and the lidar beam focus is changed from 0 to 10 core radii in x direction. As seen from Figure 4.6, the velocity peaks are damped when the vortex is out of focus of the lidar beam. After the core is passed, the velocity decays due to the combined effects of the Lorentzian weighting function decay a well as the exponential decay found in the Lamb-Oseen velocity profile. It is clear that in order to still observe these velocity peaks, the lidar should focus the beam as close as possible to the vortex center.

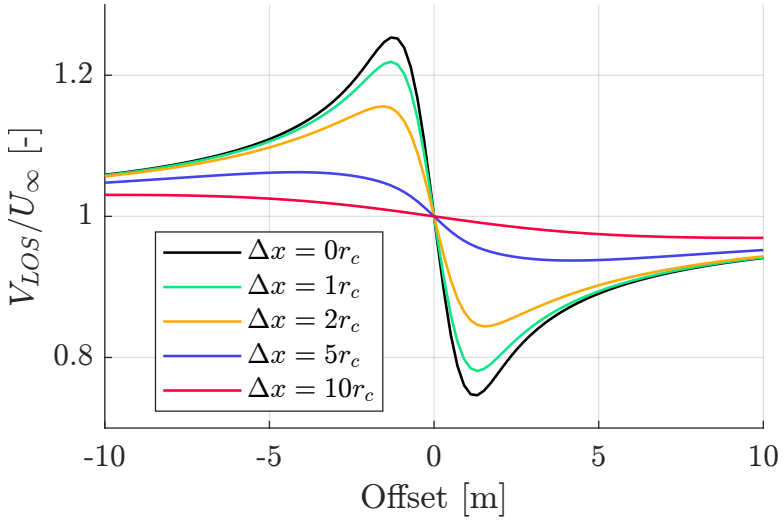

Figure 4.6: Line-of-sight velocity for varying beam focus.

For the Doppler spectrum, the beam focusing effects also translate to a damping of the perceived standard deviation shown in Figure 4.7a. It is interesting to see that for a shift of $1r_c$, there is little to no change in the standard deviation, indicating that a similar variation in velocity is obtained. This is supported by Figure 4.8 which shows the part of the Lamb-Oseen velocity profile that is within one Rayleigh length of the measurement point. It then becomes quite clear that the range of detected velocities is much smaller and that to detect the increase in standard deviation, focusing the lidar beam in the vicinity of the core radius is optimal.

The skewness shown in Figure 4.7b is a bit more difficult to analyse. The aspect of

interest here, is when and where do the shifts in skewness take place. For the first two lines ($\Delta x = 0r_c$ and $1r_c$), the skewness effects are caused by the vortex. The high vortex induced velocities shift the Doppler spectrum weight to the right (negative skew) and to the left (positive skew). The skewness lines then flip in the other direction when the effects of the vortex diminish. A positive skew is first seen, meaning that the weight of the distribution has now shifted left and that lower velocity components dominate over higher ones. This indicates that the signal from the mean velocity components is stronger than the signal from the vortex induced velocity components. An aspect of the skewness that however does not change is the zero crossing point, which always occurs when the core radius intersects with the lidar beam. At this instance, all vortex induced velocities are orthogonal to the beam and the Doppler spectrum is symmetric.

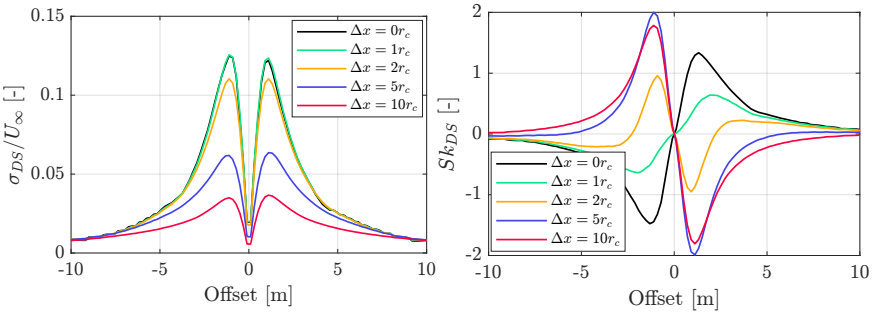

(a) Standard deviation.

(b) Skewness.

Figure 4.7: Doppler spectrum statistics for varying beam focus.

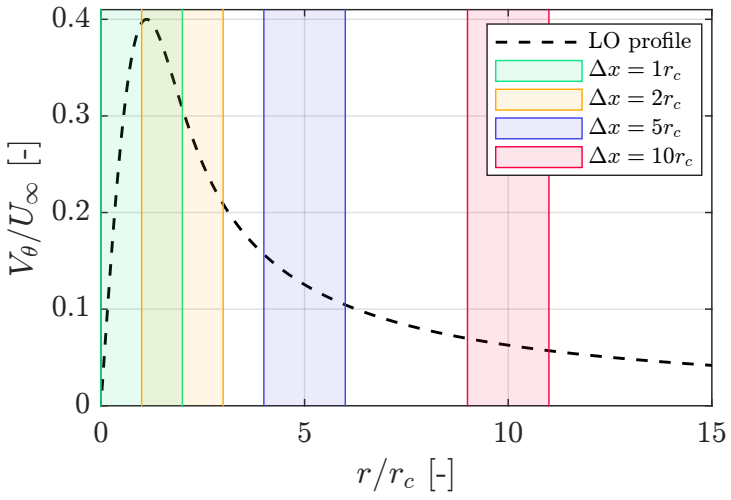

Figure 4.8: $1z_r$ measurement range for varying beam focus.

4.1.3 Angle effects

The orientation of the vortex also has an important effect in what can be detected by the lidar. The angle between the lidar beam and the vortex axis is varied from 0° to 90°. This introduces line-of-sight effects, as the induced velocity components do not align with the lidar beam anymore and only a part of the component is detected. The projected component varies with $\sin(\chi)$ and hence stronger velocity peaks are observed in Figure 4.9 when the vortex axis is orthogonal to the lidar beam. The effects on the standard deviation (Figure 4.10a) and skewness (Figure 4.10b) are quite similar, all lines are damped with a factor $\sin(\chi)$ once again. In conclusion, as long as part of the induced velocities project onto the line-of-sight, the same patterns as before are identifiable, but with more or less strength depending on the angle.

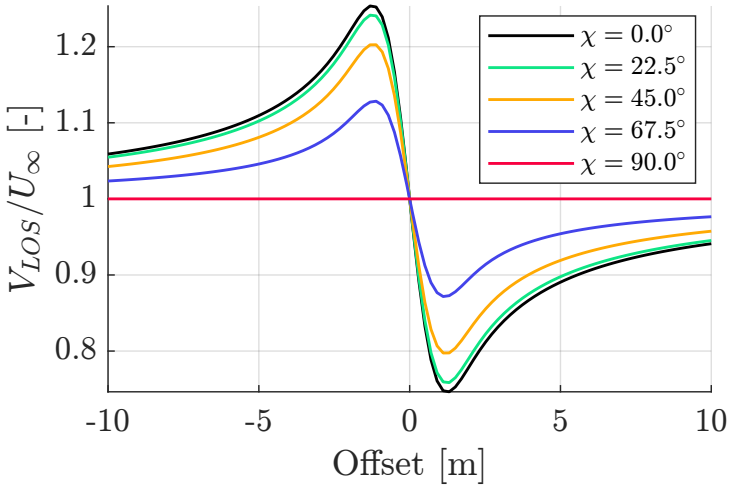

Figure 4.9: Line-of-sight velocity for varying vortex angle

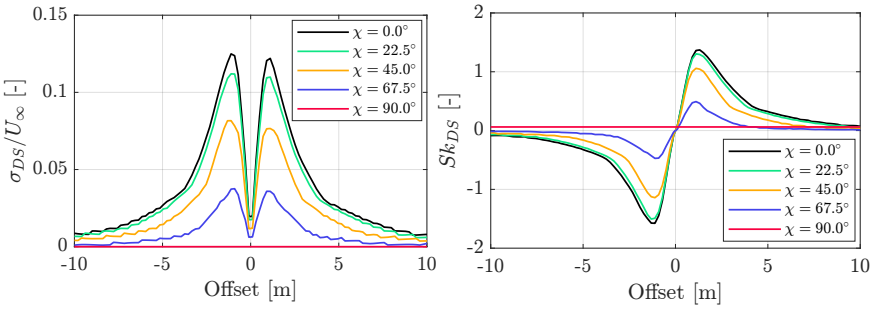

(a) Standard deviation.

(b) Skewness.

Figure 4.10: Doppler Spectra statistics for varying vortex angle

4.1.4 Core size effects

Figure 4.11 shows the line-of-sight velocity recorded whilst varying the vortex core radius. The maximum velocity induced by the vortex was kept at $0.4\,\mathrm{m\,s^{-1}}$ by adjusting the circulation accordingly. However, this does not appear in Figure 4.11 as a result of the measurement volume. For smaller core radii, the velocity peak is quite sharp and localised (see Figure 2.11b), meaning that the measurement volume consists only very partially of the added velocities induced by the vortex. The opposite is true for a larger radius, the vortex takes up a greater share of the measurement volume and boosts the estimate of the line-of-sight velocity. Keeping in mind that the vortex strength has also changed here, the velocity peaks are still observable in all cases but are now spread over different ranges.

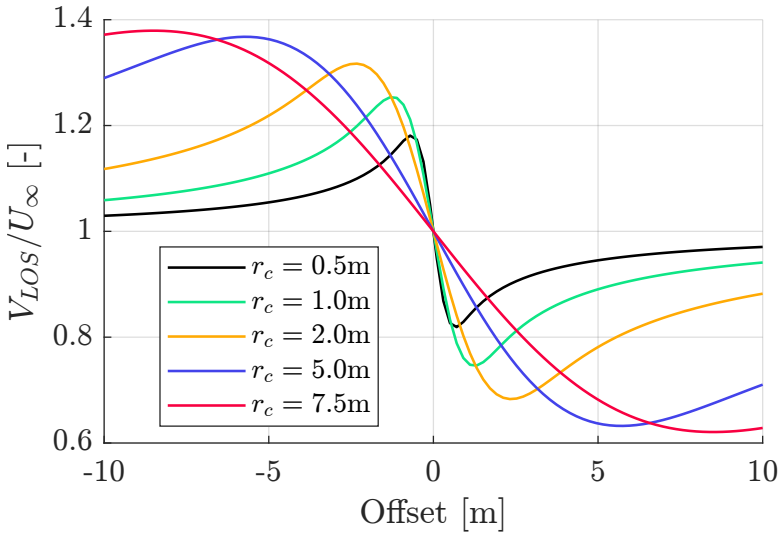

Figure 4.11: Line-of-sight velocity for varying vortex core radius

The standard deviation shown in Figure 4.12a presents the same idea that a larger vortex will take up more of the measurement volume. The velocity variations occur over a greater distance range for larger vortices, meaning that part of the velocity profile will be damped by the lidar beam and that only a small part of the velocity variations will be relevant. In the case of a small vortex, all velocity magnitudes appear within the measurement volume and are detected. This explains why the standard deviation becomes lower for increasing core radius. Using the same explanation for the skewness lines in Figure 4.12b, the skewness coefficient increases for larger radii as the vortex induced velocities make up a larger part of the measurement volume and skew the Doppler spectrum.

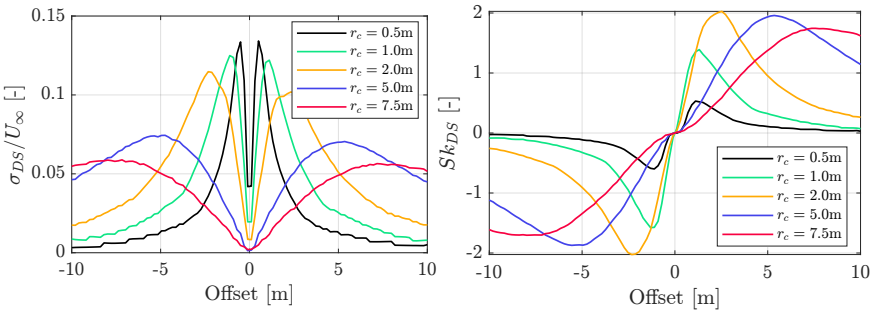

(a) Standard deviation.

(b) Skewness.

Figure 4.12: Doppler spectrum statistics for varying vortex core radius

4

4.1.5 Noise effects

The focus of this section is to add effects that should deteriorate the signal of the Lamb-Oseen vortex and, to an extent, simulate conditions closer to reality.

Signal noise

As presented in chapter 3, the lidar emulator has the capacity to simulate a beam composed of random aerosols arranged in space, which is a more realistic approximation of the atmospheric aerosol distribution than the other regular or optimal beams for example. Additionally, it is also possible to incorporate a further noise source in the form of varying aerosol sizes. The sizes of aerosols are randomly sampled and impact the contribution of each aerosol to the line-of-sight velocity. Four cases were tested, with the settings used summarised in Table 4.2. The aerosol size effects were added as described in subsection 3.2.3 and with parameters: $d_{p_m} = 0.951\,\mu\text{m}$ and $\sigma_d = 0.427\,\mu\text{m}$ [77].

Table 4.2: Random aerosol beam settings.

Label	Conditions
Hwo	High aerosol concentration ($N = 2000$) with no size effects
Lwo	Low aerosol concentration ($N = 50$) with no size effects
Hw	High aerosol concentration ($N = 2000$) with size effects
Lw	Low aerosol concentration ($N = 50$) with size effects

Figure 4.13 shows the effects of the lidar noise sources on the line-of-sight velocity. First of all, the random aerosol distribution appears to have a strong effect on the velocity peak and reduces their magnitude strongly. This phenomenon is particularly worse when the aerosol density is low as the measurement volume may not be homogeneously sampled. Secondly, the effect of aerosol size looks to be quite weak relative to the random aerosol distribution effects. Unfortunately, it is quite difficult to judge without experimental comparison whether or not this is the exact response. However, the aerosol size effect is stronger for a lower concentration and weaker for higher concentration. This is expected as the aerosol size effect will balance out for sufficiently large number of aerosols.

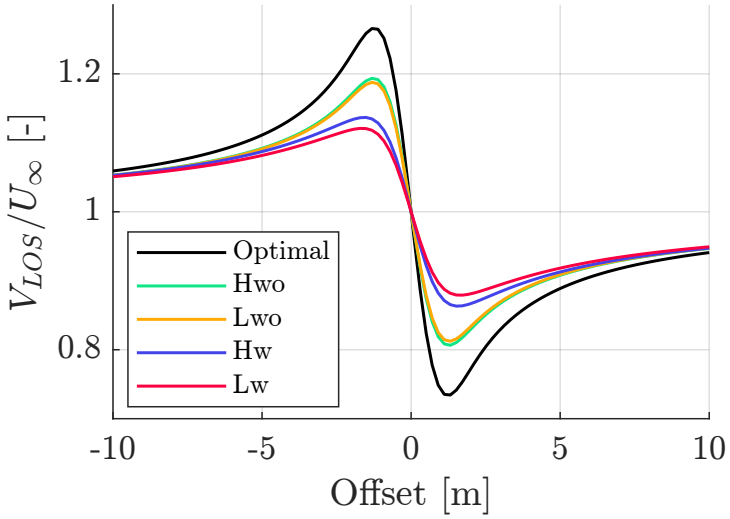

Figure 4.13: Line-of-sight velocity for various lidar beam noise sources.

The behaviour of the standard deviation is shown in Figure 4.14a. The aerosol size effects are near negligible but those of the random beam are not. A larger concentration of aerosols translates to sampling a larger number of velocities which explains the increased standard deviation of the green and yellow lines. However, this change in standard deviation remains quite small relative to the standard deviation created by the vortex. The skewness in Figure 4.14b is more affected by the added noise sources, particularly for low aerosol concentration. The combined effects are able to distort the spectrum so that the vortex induced velocities do not dominate over the mean flow anymore.

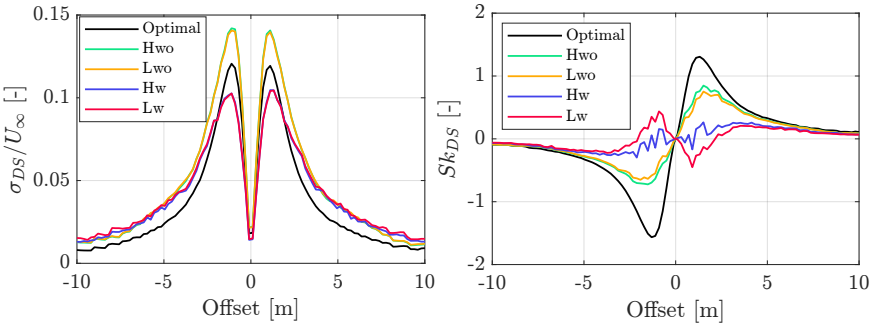

(a) Standard deviation.

(b) Skewness.

Figure 4.14: Doppler spectrum statistics for various lidar beam noise sources

Flow field noise

Flow field noise is simulated here with Mann generated turbulence with varying levels of turbulence intensity (TI). The tests are performed for multiple seeds, used for generating different turbulent conditions, from which the mean and standard deviation across all seeds are extracted. As an example, Figure 4.15 shows contours of the wind field for a single seed and increasing TI from 0 to 0.5. For this particular seed, the turbulence does not distort the vortex so much and in fact somewhat contributes to the effect of the vortex. Hence, multiple seeds are used in order to perturb the vortex in an arbitrary manner.

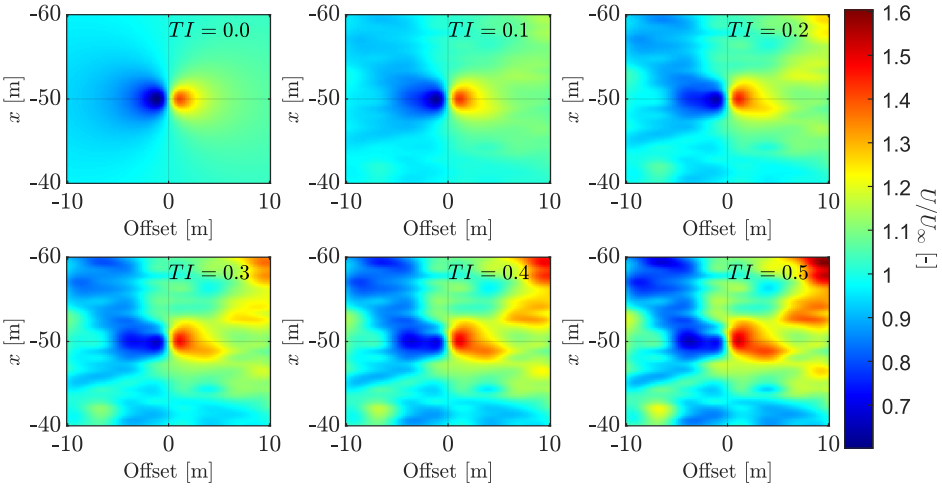

Figure 4.15: Vortex in turbulent flow field of varying TI.

Figure 4.16 displays the line-of-sight velocity measurements across the tested TI range. The black curve on all plots shows the profile for TI = 0 and the shaded area shows a standard deviation shift from the mean (coloured full lines). As TI increases, the standard deviation bands expand and the mean profile becomes increasingly distorted compared to the non-turbulent case. It is clear from the width of the band, that there reaches a point when the vortex velocity peaks may not be discernible anymore. In extreme cases where the TI reaches 0.4 or 0.5, the variations in wind speed from turbulence can reach much higher deviations than the ~ 0.3 deviation created by the vortex. Figure 4.17 shows an example of a particular case which shows a sharp drop in velocity between 0 m and 5 m which could also be assimilated to that of a vortex.

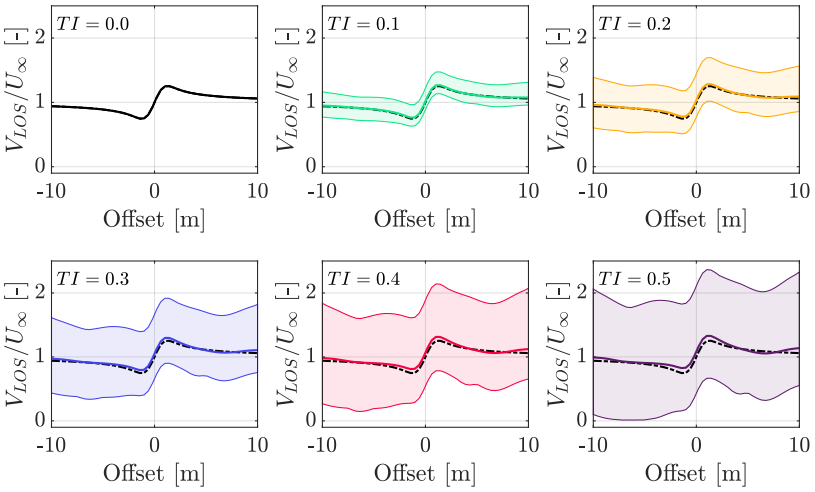

Figure 4.16: Line-of-sight velocity for varying TI. Tested over 20 turbulent seeds with mean and maximum/minimum bands shown in colour and TI = 0 line shown in black.

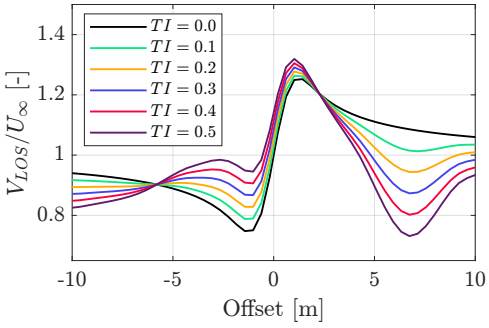

Figure 4.17: Line-of-sight velocity for varying TI (Seed 7).

A similar analysis is possible on the Doppler spectrum standard deviation and skewness (Figure 4.18 and Figure 4.19 respectively). All bands once again increase with increasing turbulence level and deviations in the mean lines are also stronger. In Figure 4.18, the standard deviation level is shifted up by the turbulence due to the additional variation in velocity magnitudes. Additionally, the shape of the mean and band lines also become less smooth, indicating sharper local jumps in σ_{DS}. The standard deviation resulting from the vortex is quite localised and is still fairly strong up to TI = 0.3. After this level, a jump in standard deviation may also be assigned to the effects of the turbulent flow. The same observation can be made for the skewness in Figure 4.19, when observing the bands, the skewness can vary quite sharply, also switching from positive to negative for TI of 0.3 and higher.

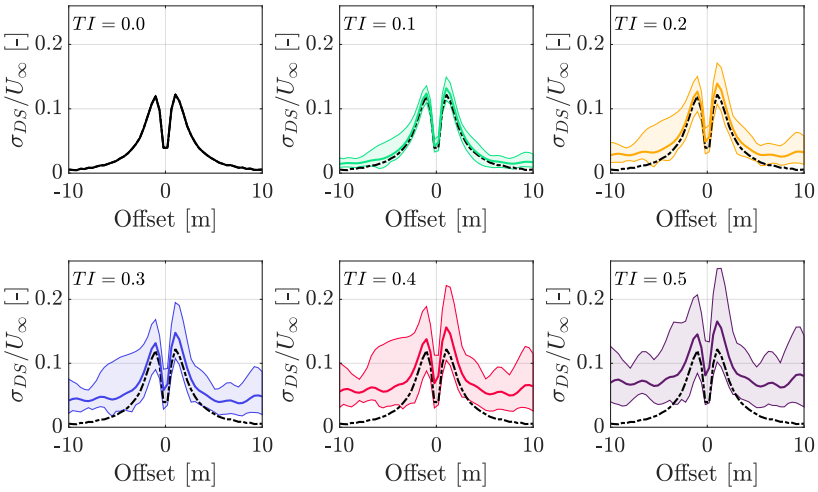

Figure 4.18: Doppler spectrum standard deviation for varying TI. Tested over 20 turbulent seeds with mean and maximum/minimum bands shown in colour and $TI = 0$ line shown in black.

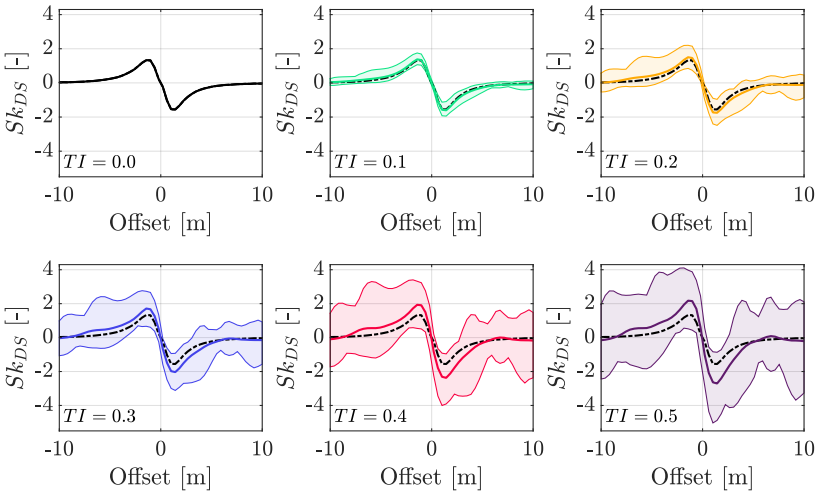

Figure 4.19: Doppler spectrum skewness for varying TI. Tested over 20 turbulent seeds with mean and maximum/minimum bands shown in colour and $TI = 0$ line shown in black.

4.2 Characterisation

From the patterns observed in section 4.1, an attempt can be made at characterising the vortex present within the flow field. To characterise the vortex, three parameters are

aimed to be recovered: the location of the core, the radius of the core and the strength of the vortex. The approach taken to estimate each parameter is described in the following sections. Figure 4.20 is shown here as reference and is only a modified version of Figure 4.4, with the minimum and maximum lines combined.

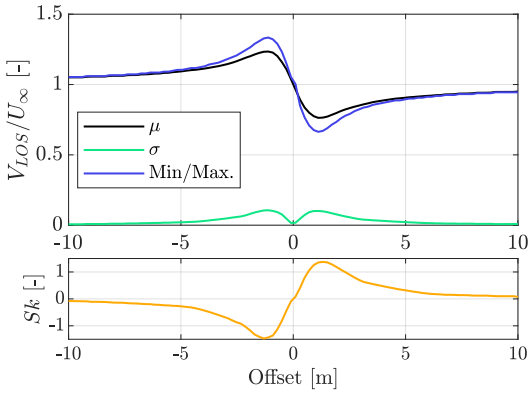

Figure 4.20: Doppler spectrum statistics for reference case.

4.2.1 Core location

A key observation from Figure 4.20 and most of the results obtained in the previous section is the symmetry property of the vortex around the core center. The measured lidar outputs also exhibit such symmetries and it is therefore possible to use this to retrieve the core location. The following three methods are implemented:

1. **Interpolate midpoint of velocity peaks**: The positions of the maximum and minimum detected velocity are found. This may also be done using the mean velocity but will be less accurate due to the damping from averaging the Doppler spectrum. The midpoint is then linearly interpolated which may require correcting for the mean velocity, which can be estimated separately or by averaging the mean velocity for the full scan.

2. **Interpolate local minimum of standard deviation**: The gradient of the standard deviation is first computed. This allows to search for when the gradient changes sign and linearly interpolate for the exact point at which the gradient is zero. As the gradient may also switch signs elsewhere throughout the scan, the velocity peaks may also be used to constrain the valid range where the core location is expected.

3. **Interpolate zero-crossing of skewness**: The points at which the skewness changes sign are first found. The point at which the skewness is expected to be zero is then linearly interpolated for. Once again, the velocity peaks may be used to define a smaller region and avoid detecting other zero-crossings of the skewness.

Each of these approaches may now be tested for varying conditions identical to the tests from section 4.1, in order to identify which performs best. Figure 4.21a shows the

absolute difference in the measured (x_c) and true ($\bar{x}_c$) core locations for different focal distances. In the same way as subsection 4.1.2, Δx is the distance between the vortex center and the lidar beam's focus range. The three methods previously listed are labelled in order as *Min./Max.*, σ and *Sk*. The standard deviation approach performs best, followed by the skewness approach. Both seem to remain within the same error range for increasing Δx as the symmetry of the standard deviation and skewness were rather unaffected under these conditions (see Figure 4.7). The min-max approach on the other hand performs poorly due to the stronger measurement volume damping for higher Δx. The interpolation for the midpoint therefore becomes more challenging as the velocity peaks are smeared out. Naturally, sampling at more locations should lead to a reduction in the error, for all methods as well. The core location error is then showed for varying angle χ and core radius in Figure 4.21b and Figure 4.21c respectively. Note that estimates for $\chi = 90°$ have been omitted as no vortex can be detected. The trends are quite similar once again, as the zone of the core location is always correctly identified and the errors mostly interpolation dominated.

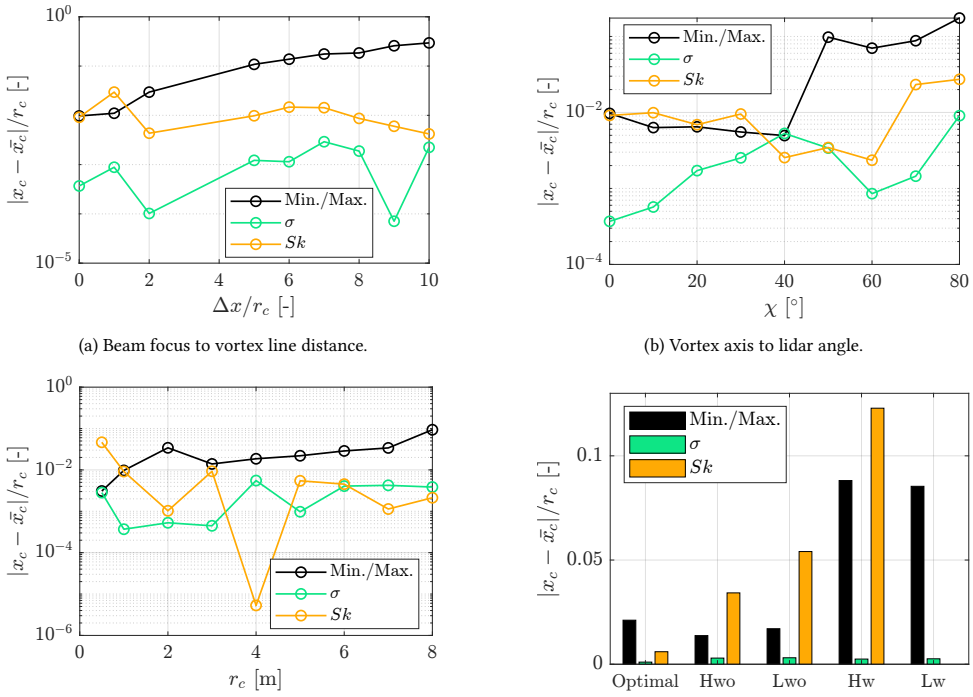

(a) Beam focus to vortex line distance.

(b) Vortex axis to lidar angle.

(c) Core radius.

(d) Lidar beam noise.

Figure 4.21: Absolute error in core location for varying conditions and methods

Figure 4.21d shows the error for the five conditions outlined in Table 4.2. Larger discrepancies between the different approaches are observed here and may also be linked back to subsection 4.1.5. The standard deviation approach remains quite accurate under all conditions as the shape of the standard deviation curve remained quite similar under

various noise conditions (see Figure 4.14). This is not the same for the skewness, which as was shown in Figure 4.14b, was quite badly distorted when including the effects of particle size on the backscattered signal. The core location estimation even becomes unfeasible for the noisiest conditions (Lw) The min-max approach is once again affected by the damping of the velocity peaks which appear further away from the core and lead to larger interpolation errors.

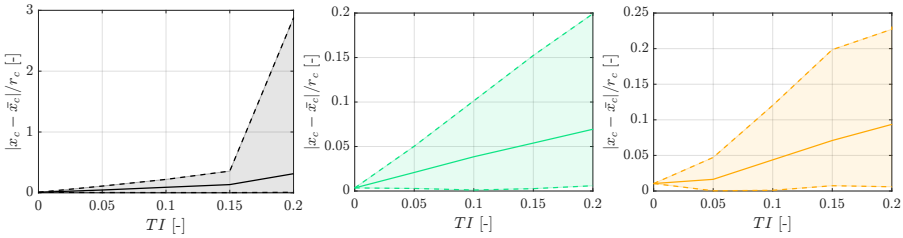

(a) Min-Max approach. (b) σ approach. (c) Sk approach.

Figure 4.22: Error in core location for varying TI and methods. Tested over 20 seeds with full lines showing mean error and dashed lines showing minimum and maximum errors.

Figure 4.22 shows the error in core location estimate under turbulent conditions for the three methods tested. The conclusions when comparing between the three approaches is still the same. The standard deviation seems like the best indicator of the core location. The TI range for this test has been decreased relative to the test from subsection 4.1.5 as the errors become increasingly larger and there are occurrences where the core location cannot even be recovered, particularly for $TI > 0.2$. In conclusion, the outcome of these tests has shown that using the standard deviation appears to be the most consistent and accurate way of locating the vortex center and confirms that turbulence is clearly the most challenging of conditions to attempt recovering vortex parameters.

4.2.2 Core radius and strength

Now that a method has been selected to locate the vortex, the next objective is to try recovering some of its defining parameters, namely the core radius and the circulation/strength. There exist various ways to tackle this problem, one could estimate core radius from vorticity or Lambda-2 and Q criterion. Circulation could also be computed directly with the line integral of velocity or fitting vortex models such as the Rankine, Burnham-Hallock [60] or Lamb-Oseen [60] models. As the main focus of this study is not on investigating ways of recovering vortex parameters, the most direct approach of fitting the measured velocity profile with the Lamb-Oseen velocity profile has been chosen. Non-linear least squares regression is applied with the aim of minimising the error between the measurements and the function given by Equation 4.4.

$$V_\theta(r) = \frac{\Gamma}{2\pi r}\left(1 - e^{-\frac{r^2}{r_c^2}}\right) \tag{4.4}$$

Some fine tuning is necessary to perform this fitting. First of all, the Min./Max. line is used as the velocity profile $V_\theta(r)$. As previously shown in Figure 4.20 this combines

the maximum and minimum Doppler spectrum velocity bins detected above a certain amplitude threshold. This removes the damping of the velocity peaks from averaging of the spectrum and leads to better estimates of Γ and r_c. The velocity profile is also adjusted by removing the mean velocity. The initial guess for the regression problem is computed for r_c as half of the velocity peak separation and for Γ as $2\pi V_{max} r_{c,guess}(1-\exp(-1))$ with V_{max} as the maximum detected velocity magnitude and $r_{c,guess}$ as the initial guess for the core radius.

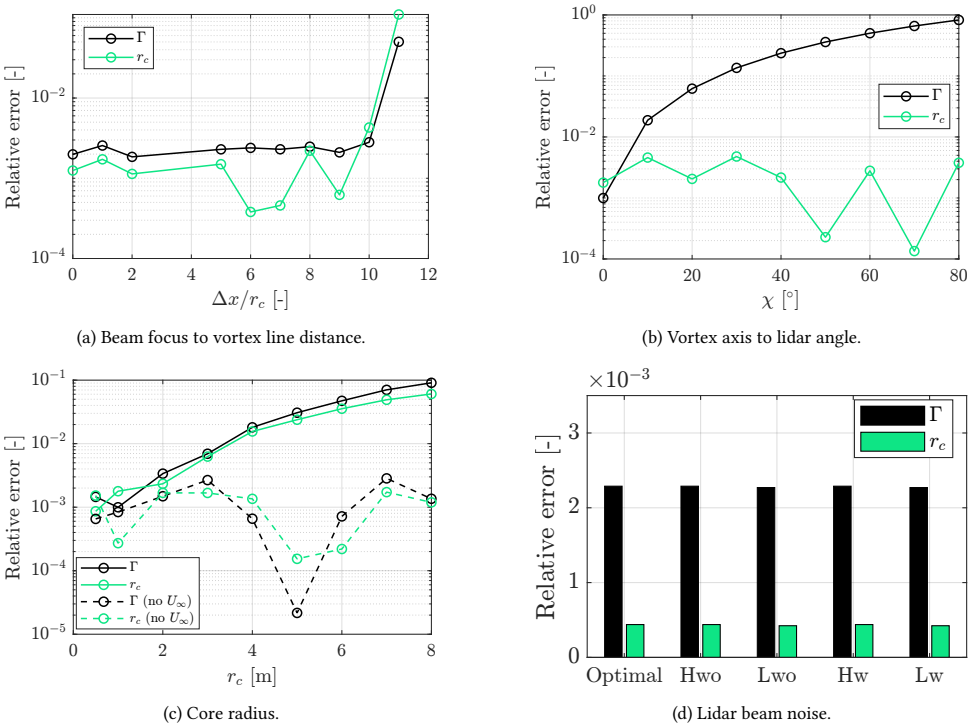

(a) Beam focus to vortex line distance.

(b) Vortex axis to lidar angle.

(c) Core radius.

(d) Lidar beam noise.

Figure 4.23: Absolute relative error in core radius and circulation for varying conditions.

The tests that were previously shown in section 4.1 and subsection 4.2.1 are repeated with identical conditions and extended to estimate the vortex core radius and circulation. Figure 4.23a shows how the relative error in circulation and core radius estimates evolves when the vortex is placed further and further away from the lidar beam's measurement point. The error remains acceptable and fairly constant until after $10r_c$ is reached. This is due to the incorrect maximum and minimum velocity bins being detected. As the vortex is not in the center of the measurement volume, the velocities are more heavily damped, which leads to the bins corresponding to the maximum and minimum velocities to have a low amplitude and falling below the threshold set. Setting a lower threshold would therefore solve this issue but would also increase the sensitivity to noise. A trade-off should therefore be made depending on the noise floor level. When varying the angle between the lidar beam and the vortex axis, recovering useful information is challenging as

due to the line-of-sight effects some of the velocity components may not be detectable at all. As seen from Figure 4.23b, the core radius estimate remains acceptable but the circulation estimate worsens with χ. This can be explained by the fact that the velocity peaks are damped from the line-of-sight effects but their position remains nearly unchanged (see Figure 4.9 for reference). The detected vortex size is therefore correctly estimated but its strength cannot be recovered unless the line-of-sight issue is solved.

Figure 4.23c illustrates the recovery of the vortex parameters for increasing core radius, and shows that the errors appear to increase. However, when taking a closer look at the procedure to recover the strength and radius, the estimate of the mean velocity was the prevailing source of error. The dashed lines in Figure 4.23c show the lower errors obtained when using the exact mean flow velocity. In the current setup, the mean velocity was estimated using the mean V_{LOS} across the full scan. Unfortunately, with increasing vortex size, most of the scan is influenced and dominated by the vortex's induced velocities rather than the mean flow field, meaning that the average velocity will be biased depending on the part of the vortex in the scan. Finally, Figure 4.23d shows the relative errors for the different noise conditions defined. There appears to be very minimal variations across different noise conditions. This is because in this particular case, the noise generated did not perturb the maximum and minimum velocity bins enough. Once again, this is also dependent on the threshold set to accept these maximum and minimum velocity bins.

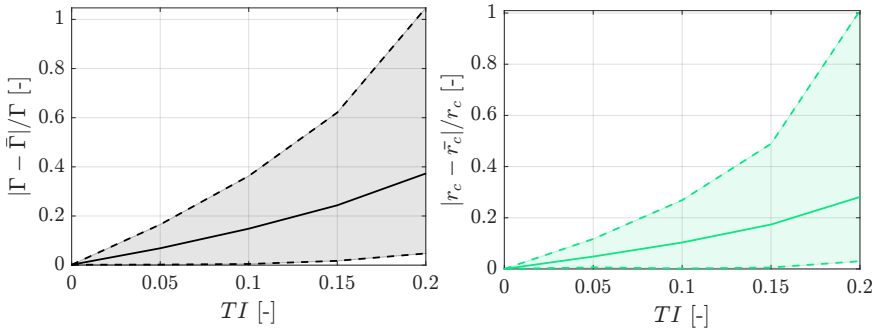

(a) Circulation.

(b) Core radius.

Figure 4.24: Mean (full) and maximum/minimum (dashed) relative error for varying TI

The results of recovering circulation and core radius are shown in Figure 4.24a and Figure 4.24b respectively. The level of relative error has clearly increased compared to the previous tests. There is a slightly narrower spread in the errors for the core radius than the circulation. This is due to the fact that the circulation is measured using the velocity magnitudes and the core radius by the position of the velocity peaks, which as previously shown in Figure 4.15, is less sensitive to turbulence. Overall, the range of error magnitudes is still quite high even for relatively low TI. This is also due to the combination of errors that arise first from the core location and mean velocity estimates and then from the distortion of the vortex velocity profile and the difficulty to fit this profile accurately.

5

Helical tip vortex identification

The purpose of this chapter is to extend the vortex identification approach previously developed to a more realistic and physical flow field. The chosen setup therefore consists of the helical vortices found within a wind turbine wake. The turbine is modelled using the actuator line method (ALM) and the flow is simulated with Large Eddy Simulation (LES) using the YALES2 flow solver [78].

5.1 DTU10MW wake

In this setup, the helical vortices are extracted from the wake of the DTU10MW reference turbine simulated by Houtin-Mongrolle et al. [79, 80], where the effects of yaw misalignment and turbulence on the wake were investigated. The data extracted from the LES simulation corresponds to spatial information obtained for a single time step. For the detection of the tip vortices to be most successful, the simplest case was selected, in order to preserve the structure of the vortices and retain a 'clean' trace of the vortex in the lidar measurements. Case LY0, in the work done by Houtin-Mongrolle et al. [79], was therefore used and consists of laminar, $10\,\mathrm{m\,s^{-1}}$, no shear velocity inflow. The DTU10MW ($D = 178.3\,\mathrm{m}$) turbine operates at a tip speed ratio of 7.5 and with no yaw misalignment. The tower and nacelle were not modelled and aero-servo-elastic simulation of the rotor was not included, meaning that no structural or control responses occur. The simulation domain is $25D \times 10D \times 10D$ but reduced to a smaller box of $0.69D \times 1.37D \times 1.37D$ for the lidar simulations. This box is centred with the hub of the rotor and starts $1.4D$ downstream of the rotor such that the start of the vortex pair-wise interaction and breakdown process is observed. The grid spacing is 1.75 m and grid interpolation is used to compute the velocity field at desired points of the lidar beam.

The helical tip and root vortices within the extracted box can be seen in Figure 5.1. One can observe that the initial tip vortices are quite 'clean', with little to no smaller structures emanating from them. This is not the case further downstream, where the tip vortices start breaking up, as well as for the root vortex which breaks down much faster than the tip vortices due to the proximity of the root vortices to one another.

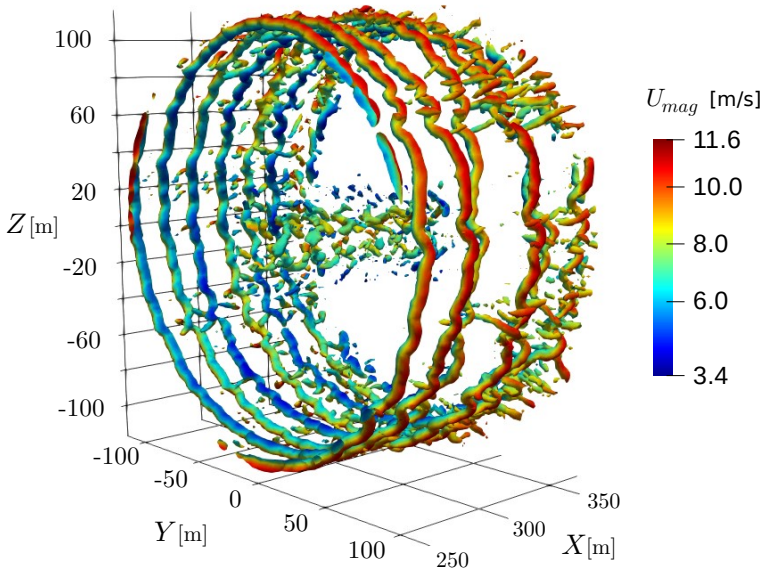

Figure 5.1: Q criterion iso-contours colored by velocity magnitude within extracted box.

The streamwise (U) and spanwise (V) velocity components at $z = 0$ are shown in Figure 5.2a and Figure 5.2b respectively. The main aspect of the streamwise component is the wake velocity deficit and the mixing with the outer flow regions, which create a shear layer at this boundary and superimposes with the effects of the tip vortices. From the spanwise point of view, most of the velocity component is due to the induced velocities of the tip vortices, with a contribution from the wake expansion which remains quite small for low turbulence levels [81].

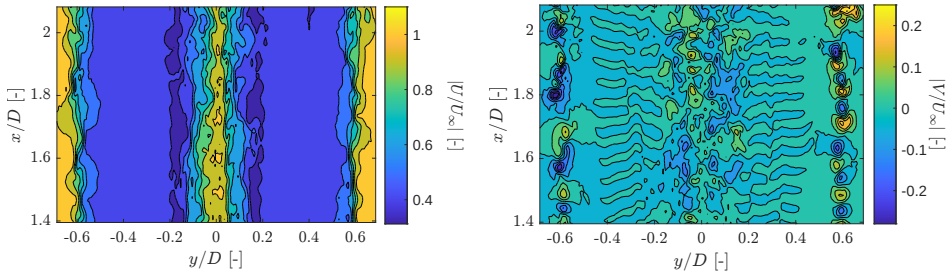

(a) Streamwise component.

(b) Spanwise component.

Figure 5.2: Wake velocity components at hub height ($z = 0$)

Figure 5.3 shows a cut through the wake, specifically at hub height or $Z = 0$. The vorticity magnitude is projected onto the slice in order to see the position and size of the vortices. Furthermore, the vortices have been labelled for clarity as L_1 through L_6 for the left side of the wake (facing streamwise) and R_1 through R_6 for the right side of the wake.

The degradation of the vortices with downstream distance is once again notable here, with the increased vorticity between vortices and the shift in y position of some vortices as a result of the pair-wise interaction. This also appears to be more prominent for the right side of the wake.

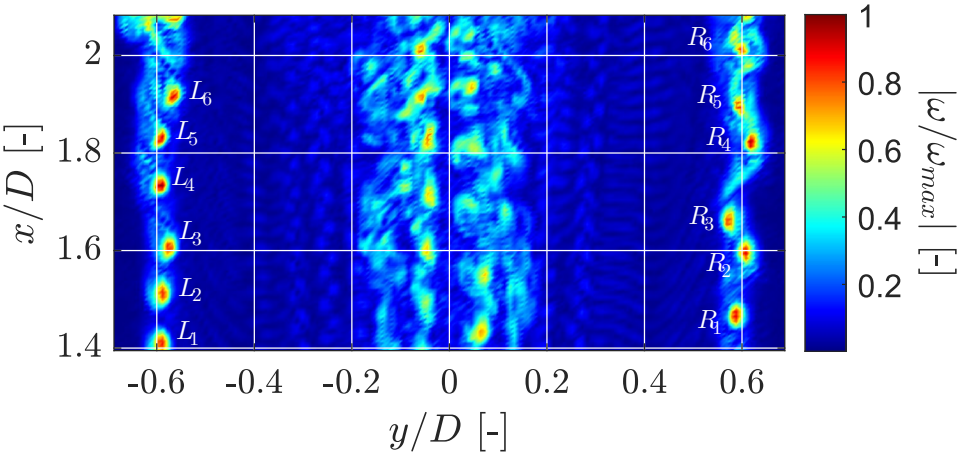

Figure 5.3: Normalised vorticity contour visualised on XY slice at hub height.

Two possible lidar setups can be made, one facing the x axis and hence measuring streamwise flow velocities, and the other facing the y axis and measuring spanwise velocities. As the main objective is to test the features shown in chapter 4 on a more physical flow field, the emphasis is not placed on the realism of the lidar setup. Experimental cases with nacelle mounted lidars or ground lidars are possible but would also require a simulated flow field that extends much further around the tip vortices in order to enclose the projected lidar beam as well as the lidar itself. Additionally, the placement of the lidar mainly influences line-of-sight and measurement volume effects during the measurement process. As previously seen in chapter 4, both of these aspects mainly damp the detected signals and cannot be truly corrected for, unless multiple beams or lidars are introduced. The goal of the following sections is therefore to preserve optimal test conditions by avoiding line-of-sight effects and keeping the measurement volume effects minimal in order to observe how the detection method previously tested on the Lamb-Oseen vortex will perform on stretched and distorted vortices found within the wake. Finally, as only Doppler spectrum and line-of-sight velocities are investigated, the 'high level' modelling approach of the lidar was used, also providing the benefit of lower computational time.

5.1.1 Streamwise scan

In this test, the lidar beam is aligned with the x-axis and therefore measures the streamwise velocity component. The lidar is placed at ($x = 1.38D, y = -0.59D$) and scans towards the positive x-axis and varies both azimuth angle and measurement distance such that measurement along a fixed x position can be made. The procedure to find the correct measurement point or beam focus range is outlined in subsection B.1.1. The idea simply

revolves around varying the beam focus range and selecting the point where the largest velocity envelope occurs. This is not detailed here as the only affects that are seen from this procedure is a damping of the measured signals due to the measurement volume effects, as previously shown in subsection 4.1.2.

The variation in azimuth introduce some LOS effects which are largest when the beam is focused close to the lidar as the angle that is swept through is larger for the same range of y. The Rayleigh length is kept fixed at 1.0 m throughout the scan. The effects of using a range-dependent Rayleigh length are shown in subsection B.1.2 of Appendix B and only show minor changes at longer ranges due to increased damping from the larger measurement volume.

In a similar way to what was done in chapter 4, some outputs are drawn out of the Doppler spectrum and plotted across a scan. This is shown for vortices L_2 and L_6 in Figure 5.4a and Figure 5.4b respectively. Identical figures for all other vortices can be found under subsection B.1.3 and subsection B.1.3 of Appendix B. The features that appear on such figures are quite similar to the results obtained during the testing on the Lamb-Oseen vortex. A velocity envelope or two opposite signed peaks in velocity is seen, the standard deviation increases approaching the core radius and drops to zero at the vortex center and the skewness also changes sign as the vortex center is passed. This therefore means that the techniques previously used to recover some of the vortex parameters can still be applied as the features that were visually identified are still present. The dashed black lines, in Figure 5.4a for example, show the estimated core location which is retrieved using the standard deviation approach described in chapter 4 and based on the local minima found in the standard deviation. This obviously becomes more challenging as vortices become more distorted such as in the case of Figure 5.4b. The area of local minimum is seen to spread over a wider range of positions and hence cannot be pinpointed with certainty. Note that although the skewness was not chosen as the preferred method for locating the core, it is still shown here for completeness and to observe that the expected behaviour still exists.

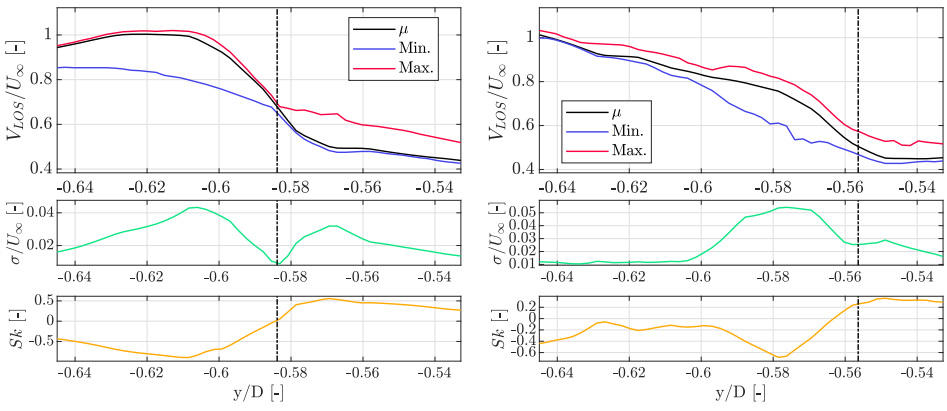

(a) Vortex L_2

(b) Vortex L_6.

Figure 5.4: Doppler spectrum outputs. Dashed line shows estimated core location.

The procedure to detect core location is then applied to all vortices on both the left side and right side of the wake and the estimated locations are shown by the black dots in Figure 5.5 and Figure 5.6 respectively. In general a fairly good match is seen. It is difficult to estimate what the true core location of these tip vortices is and therefore a visual comparison with the magnitude of vorticity is presented here. The core radius estimates are also shown by the black circles around each vortex. Similarly to the approach taken in chapter 4, the Min./Max. velocity profile is used. However, unlike the approach taken in chapter 4 of fitting the Lamb-Oseen velocity profile to the V_{LOS} profile, the core size was instead estimated by finding the distance between the two velocity peaks. This was done as the original approach largely overestimated the core size. For the Lamb-Oseen vortex, the velocity starts to decay past the core radius point. However, as seen from most of the profiles in Figure B.3 or Figure B.4, this decay does not occur and the velocity directly approaches the level of the free stream velocity as a result of the shear layer between the wake and the surrounding flow.

The exact core size of the tip vortices is difficult to quantify as the vortices are rarely circular and symmetric. Comparing the core radius estimates visually, there is clearly a trend between the estimate and the state of the vortex. The core radius estimates matches quite well with the vorticity contours when the vortex is isolated and still structured. For vortices L_6, R_3, R_5 and R_6 the core appears to be overestimated due to the smearing out of the vortex. This is noticeable in velocity curves being much flatter when moving downstream (see Figure 5.4a against Figure 5.4b).

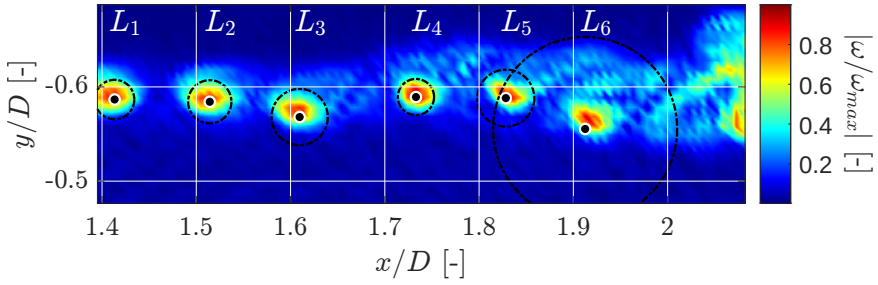

Figure 5.5: Detected vortex center and estimated core size from streamwise scan on left side of wake.

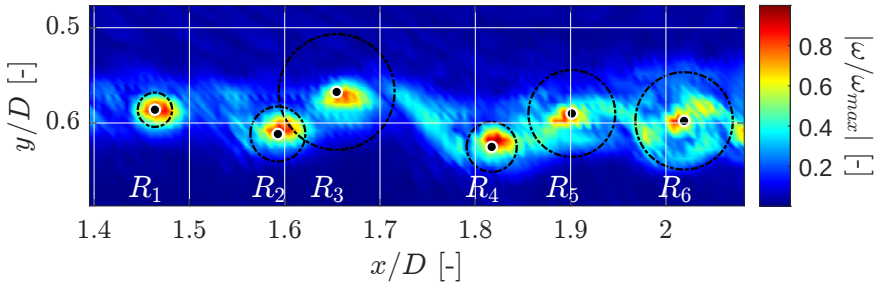

Figure 5.6: Detected vortex center and estimated core size from streamwise scan on right side of wake.

5.1.2 Spanwise scan

In this test, the lidar beam is aligned with the y-axis and hence measures the spanwise velocity component of the flow. This is done for the full length of the wake within the wake domain passing through the lidar beam, thus avoiding LOS effects. The Rayleigh length is still maintained at 1.0 m to reduce measurement volume damping. Similarly to the previous case, this is repeated both for the left and right hand sides of the wake and the same technique for estimating the optimal beam focal range is used (example given in subsection B.1.1).

Left side

As previously mentioned, the left side of the wake retains its helical tip vortex structure much better than the right side. This also translates in the detected lidar outputs shown in Figure 5.7. The oscillations in the velocities and subsequently in the Doppler spectra standard deviation and skewness are due to the measurement of the positive and negative spanwise velocities induced by the vortices. These variations remain quite clear until $x = 1.95D$, where vortex L_6 just ends, and the effects of the next tip vortex are smeared out and influence this zone. An important aspect to notice is that the line-of-sight velocity measurements may seem quite different to those shown in chapter 5 or subsection 5.1.1. This is because when viewing the vortices from the side, they are relatively close to one another and their induced effects are therefore stronger. Due to their proximity to one another, the full velocity profile is cut short by the start or end of the adjacent vortices. Furthermore, due to the vortex direction of rotation, the velocity peaks are damped.

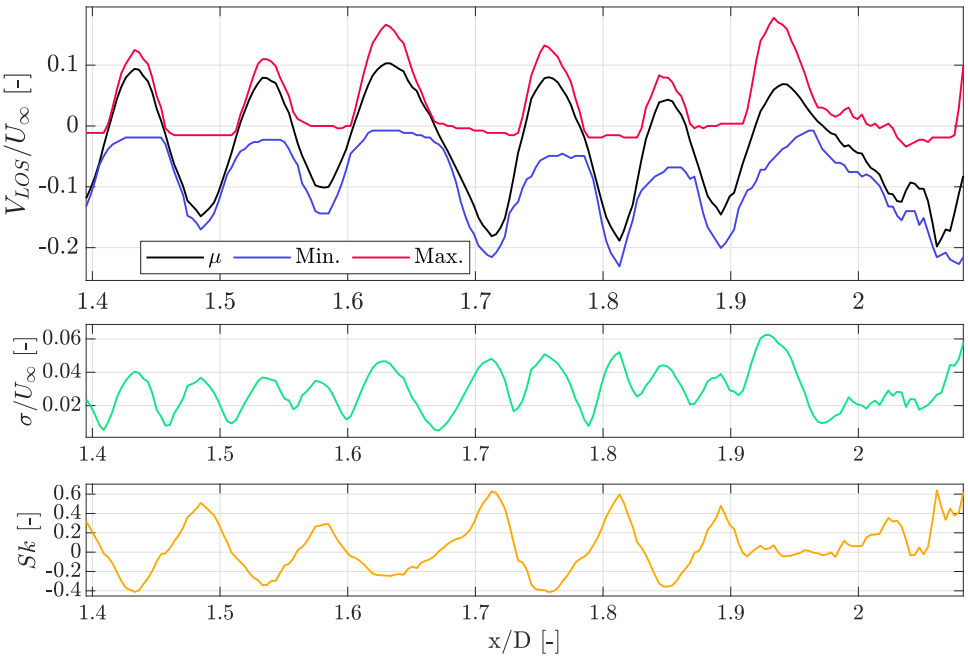

Figure 5.7: Doppler spectrum outputs across domain width on left side.

An identical procedure for characterising the vortex can be applied to this setup as well. The presence of the velocity envelope, local minima in the standard deviation and zero-crossing of the skewness are all still present in the Doppler spectrum outputs. Consequently, the local minima in the standard deviation are used to define the limits and center of each tip vortex, as shown in Figure 5.8 by the black vertical lines. It can be observed that in most of these cases this also matches quite well with the other techniques tested for core location estimate: the center of the velocity peaks and the zero-crossing of the skewness.

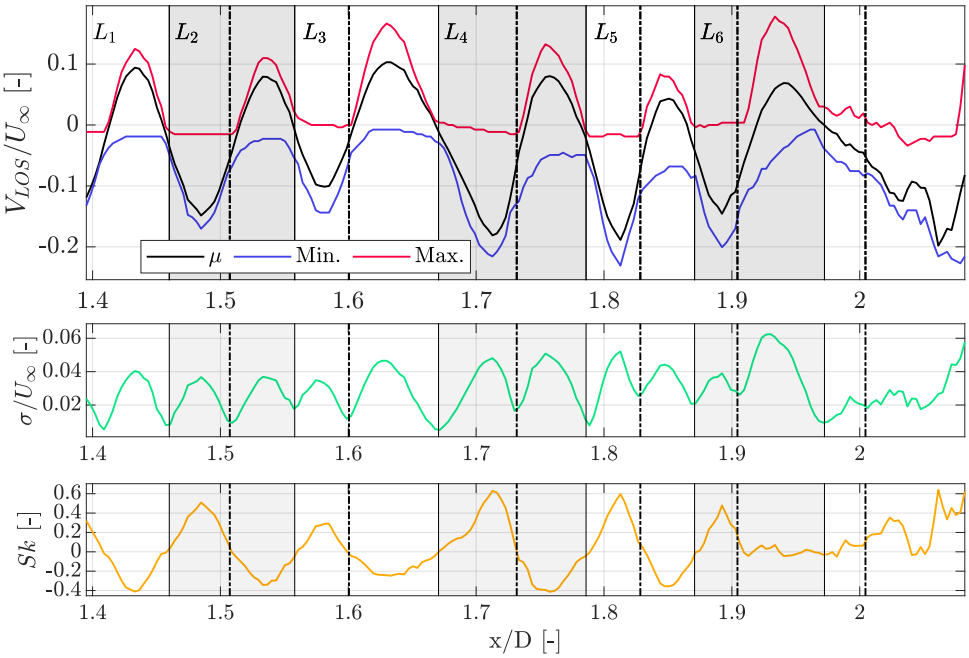

Figure 5.8: Identified vortex zone and Doppler spectrum outputs across domain width on left side. Estimated core location shown by black dashed lines.

Once again, the minimum and maximum velocity lines are used as the measured vortex velocity profile, from which vortex parameters can then be estimated. This process is shown in Figure 5.9, where the measured velocity profile (black line) is fitted with a sine wave and results in the reconstructed profile (dashed red line). The core radius is estimated as half of the wavelength of the sine wave and an additional mean term is also added to correct for the slight vertical shift of the profile that can be due to the mean streamwise velocity from the wake expansion.

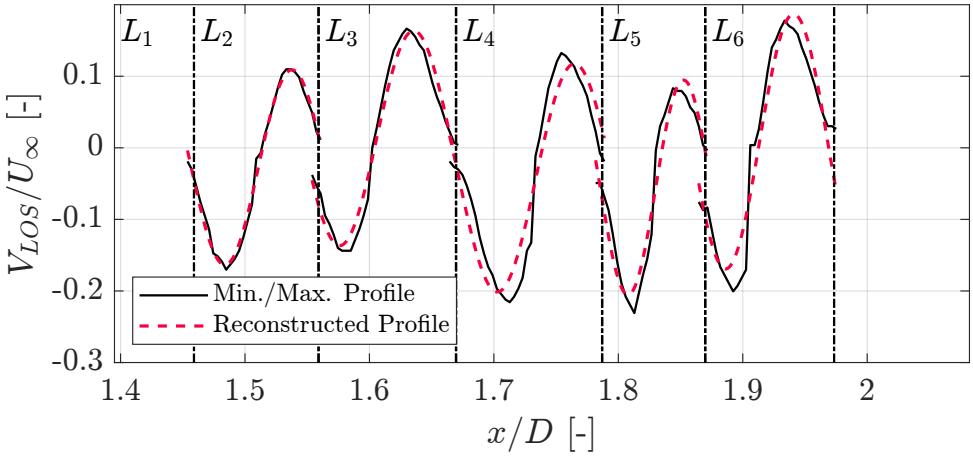

Figure 5.9: Measured and reconstructed velocity profiles across domain width on left side.

5

Figure 5.10 shows the estimated core locations and radii. The core location estimate is once again quite good but the core size is quite drastically underestimated for all vortices. As previously explained, due to the proximity of the tip vortices streamwise, the velocity peaks are damped and occur much closer to the vortex core as a result of the induction of adjacent vortices. The distance between the velocity peaks is reduced and the estimates are therefore smaller. It should however be possible to correct for this based on the estimated distance between adjacent vortices. Furthermore, the core location and radius of vortex L_1 here was not shown as only part of the vortex appears but from the features seen in Figure 5.8, the same approach can be taken using only half of the vortex profile.

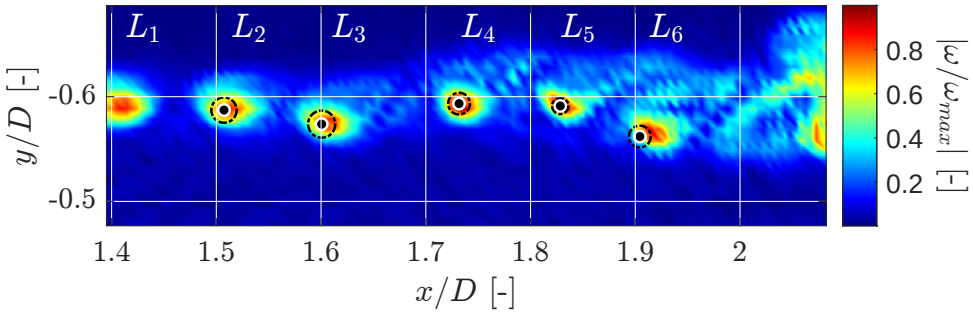

Figure 5.10: Detected vortex center and core size from spanwise scan on left side.

Right side

The same reasoning and observations can be applied to the right side of the wake. The aspects that differ here are the larger deformations of the tip vortices on the right side of the wake. As a result, it is much more difficult to accurately retrieve a clean signal or trace of the vortex. Similarly to the previous section, the Doppler spectrum outputs are shown

in Figure 5.11, with the addition of the estimated core location and limits in Figure 5.12. The reconstructed velocity profiles are depicted in Figure 5.13 and the final comparison of the estimates to the vorticity contour is shown in Figure 5.14. It is already visible from comparing Figure 5.7 and Figure 5.11 that the patterns previously observed are not as clear and constant on the right side. Vortex R_1 is perhaps the best preserved vortex. One can see in Figure 5.14 that vortex R_2 and R_3 are quite close to one another and due to their pair-wise interaction have shifted in vertical position. In the measured velocity signal, this translates to the velocity profiles of each vortex appearing as merged. As seen from Figure 5.11 or Figure 5.12, at $x = 1.65D$ the velocity decreases due to R_2 but the effects of R_3 are then immediately felt as the velocity rapidly increases back to a maximum. The features of both of these vortices can still be retrieved, visually it is still possible to conclude where approximately each of the vortices start and end, as well as estimating their respective sizes and strength. However, if this detection and characterisation is automated and generalised, then it is quite difficult to discern one vortex from the other. This is the case here, where the approach taken cannot automatically detect the left hand side of R_3 as the standard deviation signal is altered by the combined effects of R_2 and R_3. The pattern is somewhat recovered for vortex R_4 but the smearing out of the vortices R_5 and R_6 has too great of an effect on the standard deviation signal. The velocity signal and the peaks due to the last vortices are, to some extent, better preserved than the standard deviation or skewness but are still weaker than for the first few vortices.

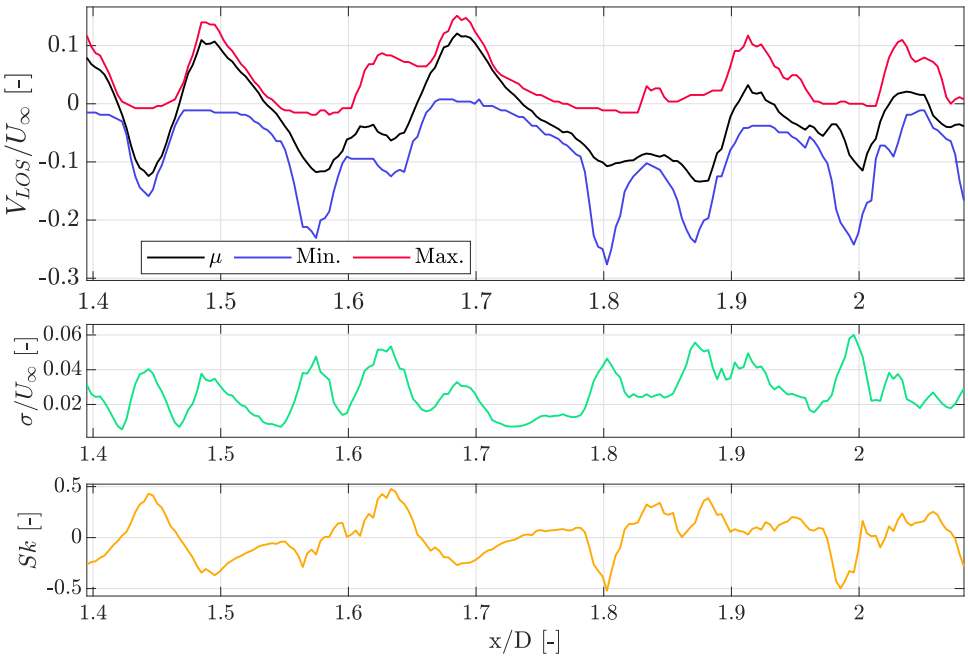

Figure 5.11: Doppler spectrum outputs across domain width on right side.

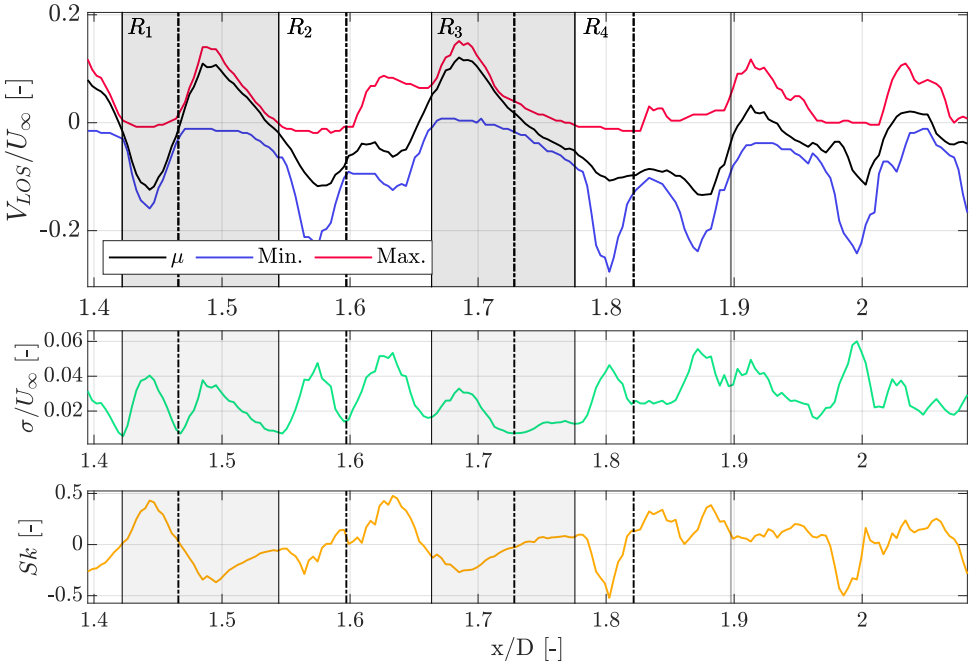

Figure 5.12: Identified vortex zone and Doppler spectrum outputs across domain width on right side.

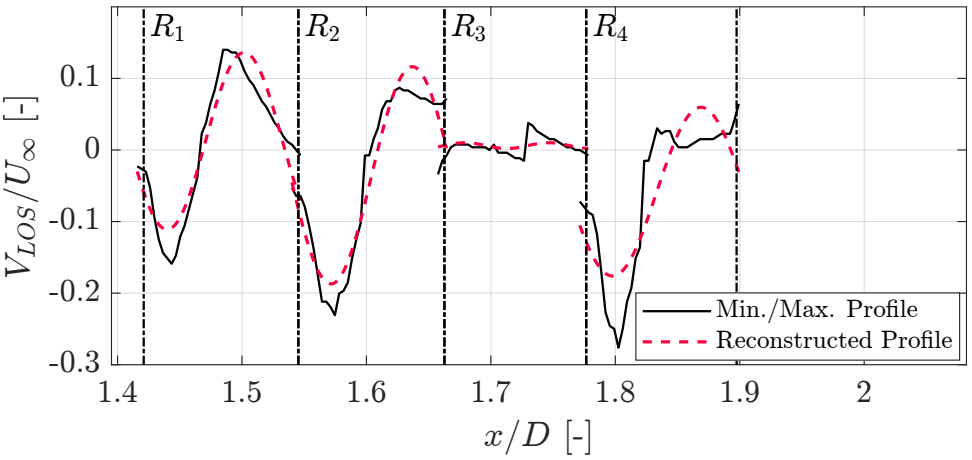

Figure 5.13: Measured and reconstructed velocity profiles across domain width on right side.

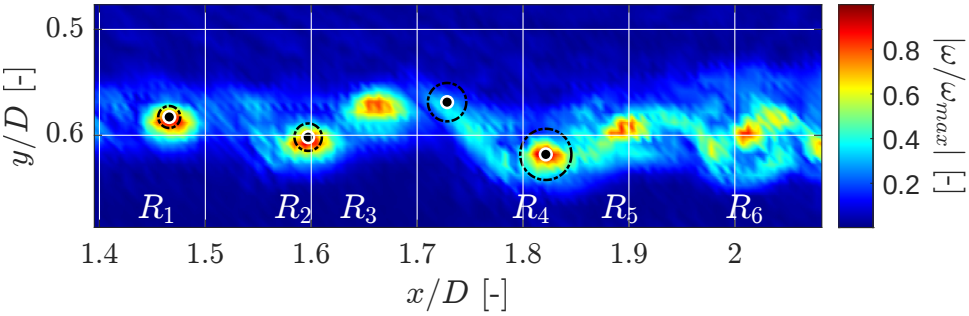

Figure 5.14: Detected vortex center and core size from spanwise scan on right side.

6

Conclusions and Recommendations

The objective of the research presented within this report was to investigate the possibility of extracting a greater level of information from the lidar measurement process, particularly in application to detecting flow structures. The following chapter provides the answers to the research questions and a general conclusion in section 6.1 and recommendations for future research work are suggested in section 6.2.

6.1 Conclusions

RQ1: ***Can a generalised approach or approaches within the numerical lidar measurement process be identified to detect turbulent flow structures?***

In order to answer this question, one should realise that turbulent flow structures cover a wide range of flow phenomena that cannot all be analysed under all possible conditions. It is however possible to answer this question for specific flow structures and under specific conditions, in the hope that a parallel can be made to more generalised cases. Several data sources can be extracted from within the lidar measurement process: the phase spectrum, the Doppler spectrum and the line-of-sight velocity. Although they all span from the same source, the backscattered light intensity time series, each provides different levels of processed information. For each lidar measurement, a 20 ms time series is obtained, repeating this over multiple measurement points therefore generates a lot of data and information. The processing of this time series therefore allows a way to condense this information whilst also lowering the noise in the measurements.

One of the main conclusions when attempting to detect vortices is that extracting information from a single measurement point is not effective. Measurements of line-of-sight velocities or Doppler spectrum are most useful when compared relative to another measurement point. When scanning through a vortex, several patterns were observed at different stages of the lidar processing chain. Starting from the final output, the line-of-sight velocity, one of the most noticeable and consistent pattern is the velocity envelope or the maximum and minimum velocity peaks that occur on either side of the vortex center. The key aspect for reliable detection of vortices using this feature, is how strong this

velocity envelope is, relative to the surrounding flow field. In ideal cases, the velocity envelope is most recognisable from two aspects of the velocity jump: how sharp it is and how localised it is in space. The sharpness of the velocity envelope can be associated to the proper measurement of the vortex. In the cases of line-of-sight, measurement volume (lidar beam focus) or signal noise effects, the velocity peaks are damped up to the point that no more of the vortex is detected. These effects are intrinsic properties of lidar operation and can be viewed as limiting factors for the detection process. For the locality of the velocity peaks, the largest factor is the surrounding flow field. In cases of high turbulence, the vortex's velocity envelope can be strongly distorted and the detection reliability is once again dependent on the relative strength of the vortex signal to the turbulent flow signal.

The next lidar output that was analysed is the Doppler spectrum, which was evaluated quantitatively by computing the first three statistical moments: mean, standard deviation and skewness. As the mean is typically used as the line-of-sight velocity estimate nothing more was concluded than before. The standard deviation's most striking feature was its increase in the vicinity to the core radius of the vortex and the local minimum reached at the vortex center. The skewness showed a trace of the vortex in the form of a change of sign as the vortex passes through. Under the effects of line-of-sight, measurement volume and signal noise, both standard deviation and skewness signals are damped but appear to conserve these features quite well. Similarly to the velocity signal, turbulence is most deteriorating to these patterns.

Finally, the analysis of the phase spectrum did not result in any useful outcome. Although some level of spatial information is contained in the phase signal, the applicability conditions are too limited to find useful, due firstly to the challenging retrieval of the correct phase and secondly to the unreliable processing to relate phase to range information.

In real flow fields, generalisation of this approach appears to be quite difficult as both the structure and motion of the vortex are idealised in the synthetic tests performed here. However, the patterns identified in the line-of-sight velocity and the Doppler spectrum appear to be quite reliable for the cases presented and could serve as a potential starting point for a more generalised approach.

RQ2: ***Which parameters of the turbulent flow structures can reliably be detected by the lidar model?***

As previously answered, vortex detection is only effective when making use of multiple measuring points. The variation of the lidar outputs are therefore necessary over a scan of the vortex. Three characterising parameters were investigated in this study: the vortex location, core radius and circulation. Three major indications of the core location are the midpoint of the velocity envelope, the local minima in the standard deviation and the zero-crossing of the skewness. These features were tested as methods of locating the vortex and compared under different conditions. The most consistent and accurate approach was found to be the standard deviation local minimum, however the use of the velocity envelope did prove to serve as a good starting guess for the location. In almost all conditions tested, the core location could be recovered. However, the effects of turbulence clearly induced the largest errors and core location retrieval becomes unsuccessful.

The suggested idea for recovering the vortex core radius and circulation was then to

apply a vortex model to the line-of-sight velocity signal. The line-of-sight velocity can be corrected for some of the measurement volume effects by making use of the information available in the Doppler spectrum. Using the maximum and minimum detected velocity bins of the Doppler spectrum, the velocity envelope can be redefined. The results of this approach under various conditions showed that the core radius is more accurately recovered than the circulation in almost all cases as the shape of the velocity profile remains quite constant but is strongly damped in most conditions. The reliability in detecting the three parameters is highest for the core location, followed by the core radius and the circulation.

RQ3: ***How is the uncertainty in the detection and characterisation of turbulent flow structures affected with increasing flow complexity?***

To answer this question, flow complexity was varied in two ways, one with adding a background turbulent wind field to the vortex and two by simulating vortices inside a wake. In both cases, it is clear that flow variations create the greatest distortion of the vortex signal amongst the tested conditions and in turn induce larger errors in both detection and characterisation of vortices. In the first case of adding turbulence to the Lamb-Oseen vortex, the effects are quite strong and clear, turbulence distorts the vortex's spatial structure randomly and the patterns identified to detect and characterise vortices become generic and arbitrary. There appears to be a trade-off between the relative magnitudes of the vortex signal, the noise from the surrounding flow field and the noise from the measurement process.

In the case of the wind turbine wake tip vortices, due to the low turbulence of the case, the vortices are not distorted in such arbitrary ways and are only partially stretched and deformed under their self-induction. The patterns identified in the Doppler spectrum are conserved but are far from being identical across different vortices. Deforming the shape of the vortex will translate to deforming the shape of the patterns (velocity envelope, standard deviation local minimum) across the scan. A generalised approach is therefore difficult to implement in such a case as identified patterns will slightly deviate from the norm. The recovery of the tip vortex parameters is also challenging here. This is a result of the unconventional shape and structure of the deformed tip vortices which are difficult to characterise using a single vortex model and may require the full velocity vector in space in order to accurately quantify.

Applicability of research

The research presented here was aimed at finding strategies of detecting certain flow structures, in the hope of possible applicability to lidar-assisted control (LAC) of wind turbines. Although much improvement and further research can follow from this work, it is possible to provide an initial judgement on the feasibility and value to real world wind turbine operation, in particular for load reduction and power optimisation as these are the two major tasks of the controller.

At this stage, conclusions can only be drawn on the detection of vortices, and not all different flow phenomena. One of the main barriers for use in real operation is the lack approximate knowledge of the vortex position within the lidar scanning volume. Unless the vortex coincidentally passes though the lidar beam or is sufficiently large compared to the scanning zone, it is unlikely to be well and reliably detected. If it is detected, the

question is then, does it value a controller response, in the form of blade pitching for example. As there are many other uncertainties: vortex strength, travelling path or rate of decay, there does not appear to be a suitable application in this form.

A potential relevance of the work shown here could be on the characterisation of the wake regions. The size and behaviour of each of these regions vary with atmospheric conditions as well as wind turbine operational settings. Measuring this through the breakdown of vortex structures may help in characterising the wake regions and provide input and feedback to the controller for better optimisation of wind farm AEP.

6.2 Recommendations

The proposals for future work span into two main directions, one being towards better definition and detection methods of different flow structures and two is towards the continued advancement of the lidar model to help characterising such structures in more realistic and varied setups.

The ideal and perhaps most logical step based on the work presented here would be to experimentally test if the patterns identified within the Doppler spectrum are still preserved in real conditions. This could be in the form of controlled experiments in a wind tunnel but should be feasible in field experiment setups provided a priori knowledge of the vortex characteristics such as in the cases of aircraft tip vortices during landing or wind turbine wake tip vortices.

As the aim was focused on the detection of vortices, and given the time constraint of this study, the accent was not placed on the accurate recovery of vortex parameters. This has however been a large source of study and research, particularly in the scope of aeronautics. There exist various techniques such as the more classical use of vortex models, but there also exist other approaches that employ statistical models [28, 30] or machine learning [82, 83] to solve the problem of detecting vortices and estimating its parameters. These studies typically make use of line-of-sight velocity only and could therefore be adapted to digest the additional lidar outputs such as the Doppler spectrum or even the direct time series.

The synthetic simulation setups can also be made more realistic. One feature is to include the temporal dimension into all simulations, adding quite some complexity to the setup but taking it closer to reality. This may lead to more difficult detection due to the evolution (motion and decay) of the flow and the coupling to the lidar scanning. However, the effects of the differences between the measurement rate of lidars and the rate at which the flow develops could be investigated.

Flow structures also do not only consist of line or tip vortices. A similar approach of searching for patterns or traces of flow structures and phenomenon within the various lidar outputs can for example be extended to larger ABL coherent structures, shear layers, gusts, etc.

This study has solely focused on continuous wave lidars. Developing the lidar emulator to incorporate pulsed lidars will allow investigation into their slightly different measurement process and possibly allow for other detection strategies to be tested. There also exists other type of lidars, such as modified versions of CW lidars [84] or lidar based on entirely different measurement principles like direct detection lidars. The latter method estimates velocity by tracking the motion of kernels or groups of aerosols with an iden-

tifiable pattern. The relationship between such kernels and flow structures could be an interesting study.

The scanning pattern configurations have remained quite simple in this work. There are however many possible variants that one could implement [46], both varying the number of beams and measurement point sequence.

Finally, a more detailed noise modelling component of the lidar model could be developed, both in terms of atmospheric as well as lidar hardware and software noise sources. The detector noise may for example be simulated with artificial white noise. An improvement can certainly be made in the direction of more physical aerosol modelling, such as including the effects of density or refractive index of the many types of aerosols that could be present in the atmosphere. One could add the attenuation of the signal due to other molecules, model the effects of cloud or ground returns and ultimately define specific atmospheric conditions such as rain, fog or clear conditions.

Bibliography

[1] UK Government, "COP26 Negotiations Explained," COP26, Tech. Rep., 2021. [Online]. Available: https://ukcop26.org/wp-content/uploads/2021/11/COP26-Negotiations-Explained.pdf

[2] D. Fraile, A. Vandenberghe, V. Klonari, L. Ramirez, I. Pineda, P. Tardieu, B. Malvault, and I. Komusanac, "Getting fit for 55 and set for 2050 -Electrifying Europe with wind energy," WindEurope, Tech. Rep., 6 2021.

[3] C. Dao, B. Kazemtabrizi, and C. Crabtree, "Wind turbine reliability data review and impacts on levelised cost of energy," *Wind Energy*, vol. 22, pp. 1848–1871, 2019. doi: 10.1002/we.2404. [Online]. Available: https://publons.com/publon/10.1002/we.2404

[4] L. Ziegler, E. Gonzalez, T. Rubert, U. Smolka, and J. J. Melero, "Lifetime extension of onshore wind turbines: A review covering Germany, Spain, Denmark, and the UK," pp. 1261–1271, 2 2018.

[5] P. Veers, "Fatigue loading of wind turbines," in *Wind Energy Systems*, J. D. Sørensen and J. N. Sørensen, Eds. Elsevier, 2011, pp. 130–158. [Online]. Available: https://linkinghub.elsevier.com/retrieve/pii/B9781845695804500053

[6] A. J. Brand, J. Peinke, and J. Mann, "Turbulence and wind turbines," in *Journal of Physics: Conference Series*, vol. 318, no. SECTION 7. Institute of Physics Publishing, 2011. doi: 10.1088/1742-6596/318/7/072005

[7] S. Frandsen and M. L. Thøgersen, "Integrated Fatigue Loading for Wind Turbines in Wind Farms by Combining Ambient Turbulence and Wakes," *Wind Engineering*, vol. 23, no. 6, pp. 327–339, 1999.

[8] A. . Peña, C. B. Hasager, M. . Badger, R. J. Barthelmie, F. . Bingöl, J.-P. . Cariou, S. . Emeis, S. T. Frandsen, M. . Harris, I. Karagali, S. E. Larsen, J. Mann, T. Mikkelsen, M. Pitter, S. Pryor, A. Sathe, D. Schlipf, C. Slinger, and R. Wagner, "Remote Sensing for Wind Energy," DTU Wind Energy, Tech. Rep., 2015.

[9] M. S. Courtney, I. Antoniou, H. E. Jørgensen, T. Mikkelsen, S. Von Hunerbein, S. Bradley, B. Piper, M. Harris, I. Marti, M. Aristu, D. Foussekis, and M. P. Nielsen, "Remote sensing the wind using Lidars and Sodars," DTU Wind Energy, Tech. Rep., 2007. [Online]. Available: https://www.researchgate.net/publication/228667199

[10] D. Kim, T. Kim, G. Oh, J. Huh, and K. Ko, "A comparison of ground-based LiDAR and met mast wind measurements for wind resource assessment over various terrain

conditions," *Journal of Wind Engineering and Industrial Aerodynamics*, vol. 158, pp. 109–121, 11 2016. doi: 10.1016/j.jweia.2016.09.011

[11] J. Mann, N. Angelou, J. Arnqvist, D. Callies, E. Cantero, R. Chávez Arroyo, M. Courtney, J. Cuxart, E. Dellwik, J. Gottschall, S. Ivanell, P. Kühn, G. Lea, J. C. Matos, J. M. Palma, L. Pauscher, A. Peña, J. Sanz Rodrigo, S. Söderberg, N. Vasiljevic, and C. Veiga Rodrigues, "Complex terrain experiments in the New EuropeanWind Atlas," *Philosophical Transactions of the Royal Society A: Mathematical, Physical and Engineering Sciences*, vol. 375, no. 2091, 4 2017. doi: 10.1098/rsta.2016.0101

[12] A. Sathe, "Estimating Turbulence Statistics and Parameters from Lidar Measurement," DTU Wind Energy, Roskilde, Tech. Rep., 6 2015. [Online]. Available: www.vindenergi.dtu.dk

[13] G. V. Iungo, Y. T. Wu, and F. Porté-Agel, "Field measurements of wind turbine wakes with lidars," *Journal of Atmospheric and Oceanic Technology*, vol. 30, no. 2, pp. 274–287, 2 2013. doi: 10.1175/JTECH-D-12-00051.1

[14] R. J. Barthelmie, S. C. Pryor, N. Wildmann, and R. Menke, "Wind turbine wake characterization in complex terrain via integrated Doppler lidar data from the Perdigao experiment," in *Journal of Physics: Conference Series*, vol. 1037, no. 5. Institute of Physics Publishing, 6 2018. doi: 10.1088/1742-6596/1037/5/052022. ISSN 17426596

[15] R. Menke, N. Vasiljević, K. S. Hansen, A. N. Hahmann, and J. Mann, "Does the wind turbine wake follow the topography? A multi-lidar study in complex terrain," *Wind Energy Science*, vol. 3, no. 2, pp. 681–691, 2018. doi: 10.5194/wes-3-681-2018

[16] D. P. Held and J. Mann, "Detection of wakes in the inflow of turbines using nacelle lidars," *Wind Energy Science*, vol. 4, no. 3, pp. 407–420, 7 2019. doi: 10.5194/wes-4-407-2019

[17] K. Träumner, T. Damian, C. Stawiarski, and A. Wieser, "Turbulent Structures and Coherence in the Atmospheric Surface Layer," *Boundary-Layer Meteorology*, vol. 154, no. 1, pp. 1–25, 1 2015. doi: 10.1007/s10546-014-9967-6

[18] I. Cheliotis, E. Dieudonné, H. Delbarre, A. Sokolov, E. Dmitriev, P. Augustin, and M. Fourmentin, "Detecting turbulent structures on single Doppler lidar large datasets: an automated classification method for horizontal scans," *Atmospheric Measurement Techniques Discussions*, pp. 1–16, 2020. doi: 10.5194/amt-2020-82

[19] A. Abraham and J. Hong, "Characterization of atmospheric coherent structures and their impact on a utility-scale wind turbine," *Flow*, vol. 2, p. E5, 2 2022. doi: 10.1017/flo.2021.20. [Online]. Available: https://www.cambridge.org/core/product/identifier/S2633425921000209/type/journal_article

[20] M. Mauz, A. Rautenberg, A. Platis, M. Cormier, and J. Bange, "First identification and quantification of detached-tip vortices behind a wind energy converter using fixed-wing unmanned aircraft system," *Wind Energy Science*, vol. 4, no. 3, pp. 451–463, 8 2019. doi: 10.5194/wes-4-451-2019

[21] L. Thobois, J. P. Cariou, and I. Gultepe, "Review of Lidar-Based Applications for Aviation Weather," *Pure and Applied Geophysics*, vol. 176, no. 5, pp. 1959–1976, 5 2019. doi: 10.1007/s00024-018-2058-8. [Online]. Available: http://link.springer.com/10.1007/s00024-018-2058-8

[22] S. Wu, X. Zhai, and B. Liu, "Aircraft wake vortex and turbulence measurement under near-ground effect using coherent Doppler lidar," *Optics Express*, vol. 27, no. 2, p. 1142, 1 2019. doi: 10.1364/oe.27.001142

[23] M. Harris, J. M. Vaughan, K. Huenecke, and C. Huenecke, "Aircraft wake vortices: a comparison of wind-tunnel data with field trial measurements by laser radar," *Aerospace Science and Technology*, vol. 4, pp. 363–370, 2000.

[24] M. Harris, R. I. Young, F. Köpp, A. Dolfi, and J.-P. Cariou, "Wake vortex detection and monitoring," *Aerospace Science and Technology*, vol. 6, no. 5, pp. 325–331, 2002. [Online]. Available: www.elsevier.com/locate/aescte

[25] D. T. Michel, M. Valla, D. Goular, L. Lombard, A. Dolfi-Bouteyre, and C. Besson, "Characterisation of Small-Scale Atmospheric Wind-Field Structures Using Coherent Wind Lidar With Short Pulses," *EPJ Web of Conferences*, vol. 237, p. 06002, 2020. doi: 10.1051/epjconf/202023706002

[26] F. Köpp, S. Rahm, and I. Smalikho, "Characterization of Aircraft Wake Vortices by 2-μm Pulsed Doppler Lidar," *Journal of Atmospheric and Oceanic Technology*, vol. 21, no. 2, pp. 194–206, 2 2004. doi: 10.1175/1520-0426(2004)021<0194:COAWVB>2.0.CO;2. [Online]. Available: http://journals.ametsoc.org/doi/10.1175/1520-0426(2004)021<0194:COAWVB>2.0.CO;2

[27] I. N. Smalikho and V. A. Banakh, "Estimation of aircraft wake vortex parameters from data measured with a 15-μm coherent Doppler lidar," *Optics Letters*, vol. 40, no. 14, p. 3408, 7 2015. doi: 10.1364/ol.40.003408

[28] R. Frehlich and R. Sharman, "Maximum Likelihood Estimates of Vortex Parameters from Simulated Coherent Doppler Lidar Data," *Journal of Atmospheric and Oceanic Technology*, vol. 22, pp. 117–130, 2005.

[29] I. Smalikho, V. Banakh, F. Holzäpfel, and S. Rahm, "Method of radial velocities for the estimation of aircraft wake vortex parameters from data measured by coherent Doppler lidar," *Optics Express*, vol. 23, no. 19, p. A1194, 9 2015. doi: 10.1364/oe.23.0a1194

[30] A. Hallermeyer, A. Dolfi-Bouteyre, M. Valla, L. Le Brusquet, G. Fleury, L. Thobois, J. P. Cariou, M. Duponcheel, and G. Winckelmans, "Development and assessment of a Wake Vortex characterization algorithm based on a hybrid LIDAR signal processing," in *8th AIAA Atmospheric and Space Environments Conference*, 2016. doi: 10.2514/6.2016-3272ï. [Online]. Available: https://hal-centralesupelec.archives-ouvertes.fr/hal-01377098

[31] C. Weitkamp, *Springer Series in OPTICAL SCIENCES*. Springer, 2005, vol. 1.

[32] Paul McManamon, *LiDAR technologies and systems*. SPIE, 2019.

[33] European Cooperation in Science and Technology, "Lidar fundamentals," 2014. [Online]. Available: http://cfa.aquila.infn.it/wiki.eg-climet.org/index.php5/Lidar_fundamentals

[34] Naval Air Warfare Center, *Electronic Warfare and Radar Systems Engineering Handbook*, 4th ed. Point Mugu, CA: Naval Air Warfare Center, 10 2013.

[35] R. Krishna, T. Unsworth, and R. Edge, "Raman Spectroscopy and Microscopy," in *Reference Module in Materials Science and Materials Engineering*. Elsevier, 2016.

[36] D. J. Lockwood, *Encyclopedia of Color Science and Technology*. Springer New York, 2016.

[37] R. M. Hardesty, "Environmental Measurements: Doppler Lidar," in *Encyclopedia of Modern Optics*. Elsevier, 2005. ISBN 978-0-12-369395-2

[38] C. R. Nave, "Mie Scattering." [Online]. Available: http://hyperphysics.phy-astr.gsu.edu/hbase/atmos/blusky.html

[39] N. Cézard, C. Besson, A. Dolfi-Bouteyre, and L. Lombard, "Optical Diagnostics of Flows Airflow Characterization by Rayleigh-Mie Lidars," Aerospace Lab, Tech. Rep., 2009. [Online]. Available: https://hal.archives-ouvertes.fr/hal-01180643

[40] R. Scheps, "Introduction to Laser Diode-Pumped Solid State Lasers: Basic Concepts," in *Introduction to Laser Diode-Pumped Solid State Lasers*. SPIE, 1 2002, vol. TT53, ch. Basic Concepts, pp. 7–22. [Online]. Available: https://www-spiedigitallibrary-org.tudelft.idm.oclc.org/ebooks/TT/Introduction-to-Laser-Diode-Pumped-Solid-State-Lasers/2/Basic-Concepts/10.1117/3.2279412.ch2

[41] R. Paschotta, *Field Guide to Lasers*. SPIE, 1 2008. ISBN 9780819478269

[42] D. C. Giancoli, *Physics for scientists & engineers with modern physics*. Pearson Educatioin Limited, 2014. ISBN 1292020768

[43] F. Scarano, "Experimental Aerodynamics," TU Delft, Tech. Rep., 2013.

[44] T. Mikkelsen, "On mean wind and turbulence profile measurements from ground-based wind lidars limitations in time and space resolution with continuous wave and pulsed lidar systems." DTU Wind Energy, Tech. Rep., 2021.

[45] ZX Lidars, "ZX TM - Turbine Mounted wind Lidar," 2022. [Online]. Available: https://www.zxlidars.com/wind-lidars/zx-tm/

[46] N. Dimitrov and A. Natarajan, "Application of simulated lidar scanning patterns to constrained Gaussian turbulence fields for load validation," *Wind Energy*, vol. 20, no. 1, pp. 79–95, 1 2017. doi: 10.1002/we.1992

[47] J. F. Newman, P. M. Klein, S. Wharton, A. Sathe, T. A. Bonin, P. B. Chilson, and A. Muschinski, "Evaluation of three lidar scanning strategies for turbulence measurements," *Atmospheric Measurement Techniques*, vol. 9, no. 5, pp. 1993–2013, 5 2016. doi: 10.5194/amt-9-1993-2016

[48] R. Frehlich, "Doppler lidar measurements of winds and turbulence in the boundary layer," *IOP Conference Series: Earth and Environmental Science*, vol. 1, p. 012017, 5 2008. doi: 10.1088/1755-1307/1/1/012017

[49] F. Dunne, E. Simley, and L. Y. Pao, "LIDAR Wind Speed Measurement Analysis and Feed-Forward Blade Pitch Control for Load Mitigation in Wind Turbines," NREL, Tech. Rep., 2010. [Online]. Available: http://www.osti.gov/bridge

[50] Vaisala, "WindCube," 2022. [Online]. Available: https://www.vaisala.com/en/wind-lidars/wind-energy/windcube

[51] P. Lindelöw-Marsden, "UpWind D1. Uncertainties in wind assessment with LIDAR." DTU Wind Energy, Tech. Rep., 2009.

[52] International Electrotechnical Commission (IEC), "IEC 61400-1: Wind energy generation systems - Part 1: Design requirements," International Electrotechnical Commission, Geneva, Tech. Rep., 2019. [Online]. Available: www.ds.dk

[53] J. F. Manwell, J. G. McGowan, and A. L. Rogers, *Wind Energy Explained.* Wiley, 12 2009. ISBN 9780470015001

[54] R. Stull, *Practical Meteorology An Algebra-based Survey of Atmospheric Science.* Vancouver: Sundog Publishing, 2017.

[55] J. v. d. Temple, *Design of support structures for offshore wind turbines.* Published and distributed by the author in cooperation with Offshore Engineering, 2006. ISBN 9076468117

[56] G. I. Taylor, "Statistical theory of turbulenc," *Proceedings of the Royal Society of London. Series A - Mathematical and Physical Sciences*, vol. 151, no. 873, pp. 421–444, 9 1935. doi: 10.1098/rspa.1935.0158

[57] A. N. Kolmogorov, "The local structure of turbulence in incompressible viscous fluid for very large Reynolds numbers," *Proceedings of the Royal Society of London. Series A: Mathematical and Physical Sciences*, vol. 434, no. 1890, pp. 9–13, 7 1991. doi: 10.1098/rspa.1991.0075

[58] J. Mann, "The Spatial Structure of Neutral Atmospheric Surface-Layer Turbulence," *Journal of Fluid Mechanics*, vol. 273, pp. 141–168, 1994. doi: 10.1017/S0022112094001886

[59] ——, "Atmospheric turbulence," Technical University of Denmark, Roskilde, Tech. Rep., 5 2012.

[60] H. Lamb, *Hydrodynamics*, 6th ed. New York: Cambridge University Press, 1932.

[61] P. G. Saffman, *Vortex Dynamics*. Cambridge University Press, 1 1993. ISBN 9780521477390. [Online]. Available: https://www.cambridge.org/core/product/identifier/9780511624063/type/book

[62] L. Vermeer, J. Sørensen, and A. Crespo, "Wind turbine wake aerodynamics," *Progress in Aerospace Sciences*, vol. 39, no. 6-7, pp. 467–510, 8 2003. doi: 10.1016/S0376-0421(03)00078-2

[63] F. Porté-Agel, M. Bastankhah, and S. Shamsoddin, "Wind-Turbine and Wind-Farm Flows: A Review," *Boundary-Layer Meteorology*, vol. 174, pp. 1–59, 2020. doi: 10.1007/s10546-019-00473-0. [Online]. Available: https://doi.org/10.1007/s10546-019-00473-0

[64] J. N. Sørensen, "Instability of helical tip vortices in rotor wakes," *Journal of Fluid Mechanics*, vol. 682, pp. 1–4, 9 2011. doi: 10.1017/jfm.2011.277

[65] I. Neunaber, M. Hölling, R. J. A. M. Stevens, G. Schepers, and J. Peinke, "Distinct Turbulent Regions in the Wake of a Wind Turbine and Their Inflow-Dependent Locations: The Creation of a Wake Map," *Energies*, vol. 13, no. 20, p. 5392, 10 2020. doi: 10.3390/en13205392

[66] J. Bartl, T. H. Hansen, W. Ludwig Kuhn, F. Mühle, and L. Sætran, "Vortex interaction in the wake of a two- and three-bladed wind turbine," *Journal of Physics: Conference Series*, vol. 1669, no. 1, p. 012027, 10 2020. doi: 10.1088/1742-6596/1669/1/012027

[67] M. Felli, R. Camussi, and F. Di Felice, "Mechanisms of evolution of the propeller wake in the transition and far fields," *Journal of Fluid Mechanics*, vol. 682, pp. 5–53, 9 2011. doi: 10.1017/jfm.2011.150

[68] P. Davidson, *Incompressible Fluid Dynamics*. Oxford University Press, 2022.

[69] D. Micallef and T. Sant, "A Review of Wind Turbine Yaw Aerodynamics," in *Wind Turbines - Design, Control and Applications*. InTech, 7 2016.

[70] W. H. Press, B. P. Flannery, S. A. Teukolsky, W. T. Vetterling, and H. Gould, *Numerical Recipes: The Art of Scientific Computing*, 3rd ed. Cambridge UK: Cambridge University Press, 2007, no. 1.

[71] R. G. Grainger, "Some Useful Formulae for Aerosol Size Distributions and Optical Properties," University of Oxford, Tech. Rep., 2020.

[72] M. Howard, A. Luttman, N. Operations, D. Frayer, D. Marks, M. Schauer, and P. Steele, "Mie Scattering Analysis," National Security Technologies, Tech. Rep., 2016.

[73] J. H. Seinfeld and S. Pandis, *Atmospheric Chemistry and Physics: From Air Pollution to Climate Change*. Wiley, 2016. ISBN 9781118947401

[74] F. Harris, "On the use of windows for harmonic analysis with the discrete Fourier transform," *Proceedings of the IEEE*, vol. 66, no. 1, pp. 51–83, 1978. doi: 10.1109/PROC.1978.10837

[75] A. Sathe and J. Mann, "A review of turbulence measurements using ground-based wind lidars," *Atmospheric Measurement Techniques*, vol. 6, no. 11, pp. 3147–3167, 11 2013. doi: 10.5194/amt-6-3147-2013

[76] V. A. Banakh, I. N. Smalikho, F. Köpp, and C. Werner, "Representativeness of wind measurements with a cw Doppler lidar in the atmospheric boundary layer," *Applied Optics*, vol. 34, no. 12, p. 2055, 4 1995. doi: 10.1364/AO.34.002055

[77] C. McLinden, "Atmospheric Aerosols," 7 1999. [Online]. Available: https://www.ess.uci.edu/~cmclinden/link/xx/node22.html

[78] V. Moureau, P. Domingo, and L. Vervisch, "Design of a massively parallel CFD code for complex geometries," *Comptes Rendus Mécanique*, vol. 339, no. 2-3, pp. 141–148, 2 2011. doi: 10.1016/j.crme.2010.12.001

[79] F. Houtin-Mongrolle, P. Benard, G. Lartigue, and V. Moureau, "A level-set framework for the wind turbine wake analysis: from high-fidelity unsteady simulations to 1D momentum theory," *Journal of Physics: Conference Series*, vol. 1934, no. 1, p. 012011, 5 2021. doi: 10.1088/1742-6596/1934/1/012011

[80] F. Houtin-Mongrolle, "Investigations of yawed offshore wind turbine interactions through aero-servo-elastic Large Eddy Simulations," Ph.D. dissertation, University of Rouen, Rouen, 2022.

[81] M. Liu, Z. Liang, and H. Liu, "Numerical Investigations of Wake Expansion in the Offshore Wind Farm Using a Large Eddy Simulation," *Energies*, vol. 15, no. 6, p. 2022, 3 2022. doi: 10.3390/en15062022

[82] N. Wartha, A. Stephan, F. Holzäpfel, and G. Rotshteyn, "Characterizing aircraft wake vortex position and strength using LiDAR measurements processed with artificial neural networks," *Optics Express*, vol. 30, no. 8, p. 13197, 4 2022. doi: 10.1364/OE.454525

[83] P. Weijun, D. Yingjie, Z. Qiang, T. Jiahao, and Z. Jun, "Deep Learning for Aircraft Wake Vortex Identification," *IOP Conference Series: Materials Science and Engineering*, vol. 685, no. 1, p. 012015, 11 2019. doi: 10.1088/1757-899X/685/1/012015

[84] E. Brinkmeyer, "CW Lidar for wind sensing featuring numerical range scanning and strong inherent suppression of disturbing reflections," in *Techniques, and Measurements for Atmospheric Remote Sensing XI*, U. N. Singh and D. N. Nicolae, Eds., 10 2015. doi: 10.1117/12.2191998 p. 96450C.

A

Appendix

A.1 Derivation of phase term

Equation A.1 shows the mixing of the local oscillator and backscattered signals with phase terms included. The backscattered signal is simply a combination of the Doppler signal (D) and the emitted signal, which is often identical to the local oscillator, unless an additional frequency shift is added such as in the case of heterodyne detection to obtain information on velocity direction.

$$\begin{aligned}
E^2 &= \left[E_0\cos(\omega_0 t+\phi_0)+E_{BS}\cos(\omega_{BS}t+\phi_{BS})\right]^2 \\
&= \left[E_0\cos(\omega_0 t+\phi_0)+E_{BS}\cos((\omega_0-\omega_D)t+\phi_0-\phi_D)\right]^2 \\
&= E_0^2\cos^2(\omega_0 t+\phi_0)+E_{BS}^2\cos^2((\omega_0-\omega_D)t+\phi_0-\phi_D) \\
&\qquad +2E_0E_{BS}\cos(\omega_0 t+\phi_0)\cos((\omega_0-\omega_D)t+\phi_0-\phi_D) \\
&= E_0^2\cos^2(\omega_0 t+\phi_0)+E_{BS}^2\cos^2((\omega_0-\omega_D)t+\phi_0-\phi_D) \\
&\quad +E_0E_{BS}\left[\cos((\omega_0+(\omega_0-\omega_D))t+\phi_0+\phi_0-\phi_D)\right. \\
&\quad \left.+\cos((\omega_0-(\omega_0-\omega_D))t+\phi_0-\phi_0+\phi_D)\right]
\end{aligned} \tag{A.1}$$

Simplifying the end result of Equation A.1 and taking only the low and detectable frequency component, Equation A.2 is left. The phase is simply a time shift relative to the period of the signal and is hence expressed as $\phi = 2\pi\frac{\Delta t}{T}$ with $T = \frac{1}{f}$ being the period of the signal. The time shift is then modelled as the time taken for the light wave to travel to a point and reflect back to the detector which is $\Delta t = \frac{2d}{c}$. Finally, the beats frequency can also be expressed as a function of the line-of-sight velocity.

$$
\begin{aligned}
&\cos((\omega_0 - (\omega_0 - \omega_D))t + \phi_0 - \phi_0 + \phi_D) \\
&\quad = \cos(\omega_D t + \phi_D) \\
&\quad = \cos\left(2\pi f_D t + 2\pi \frac{\Delta t}{T}\right) \\
&\quad = \cos\left(2\pi f_D t + 2\pi \Delta t f_D\right) \\
&\quad = \cos\left(2\pi f_D t + 2\pi \frac{2r}{c} f_D\right) \\
&\quad = \cos\left(2\pi \frac{2V_{LOS}}{\lambda} t + \frac{8\pi V_{LOS} r}{c\lambda}\right)
\end{aligned}
\tag{A.2}
$$

A.2 Spectral leakage

The effects of spectral leakage on the amplitude and phase spectra can be viewed on Figure A.1. Note that the orange peaks show the phase at the frequencies/velocities with peak amplitudes. In the amplitude spectrum, the energy is spread over multiple bins which are adjacent to the true frequency or V_{LOS}. In the phase spectrum, this creates large offsets in the phase magnitude which are related to the amount of the sampled signal that is cut off. It is important to remember that the FFT is performed on a finite sample and is assumed to be periodic across this sample. However, it is unlikely the sampled signal starts and ends at the same point in the period, particularly with a wide range of frequencies, therefore some discontinuities will be present.

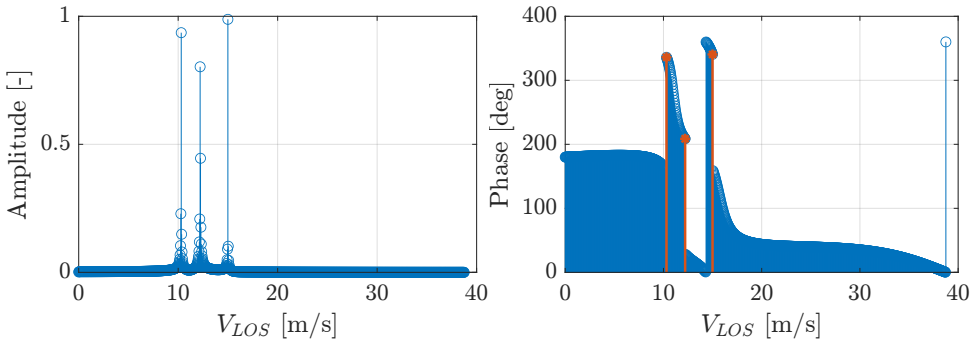

(a) Amplitude spectrum

(b) Phase spectrum

Figure A.1: FFT outputs with spectral leakage

Figure A.2 presents the FFT performed on the same original signal used for Figure A.1. Here, the frequency peak are much sharper and fall into one bin. The phase magnitudes that are obtained are now exact and no offsets are created from spectral leakage. This is done by rounding the frequencies to a certain level of significant figures such that no variations smaller than the bin width are detected.

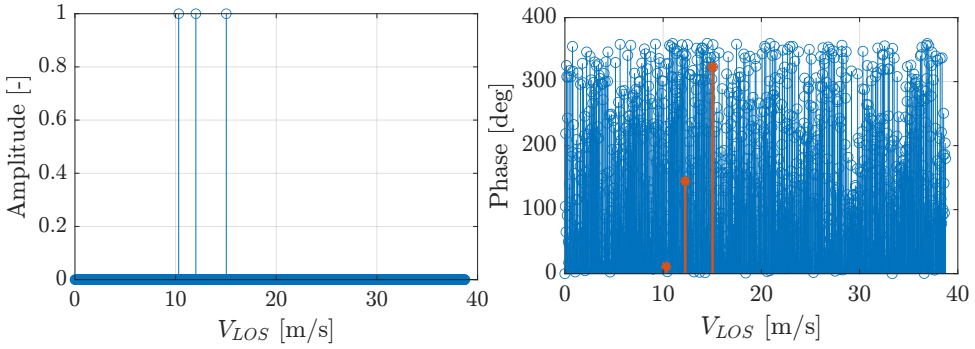

(a) Amplitude spectrum

(b) Phase spectrum

Figure A.2: FFT outputs without spectral leakage

Figure A.3 and Figure A.4 show respectively the reconstructed time series with and without spectral leakage. The differences are quite clear. On Figure A.3, the reconstructed signal matches the original signal at certain times and the frequency or period of oscillations is roughly respected. However the reconstructed signal shows shifts in both time and amplitude which is not the case for Figure A.4.

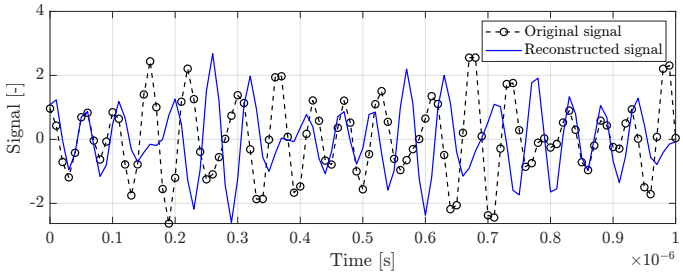

Figure A.3: Original and reconstructed signals with spectral leakage

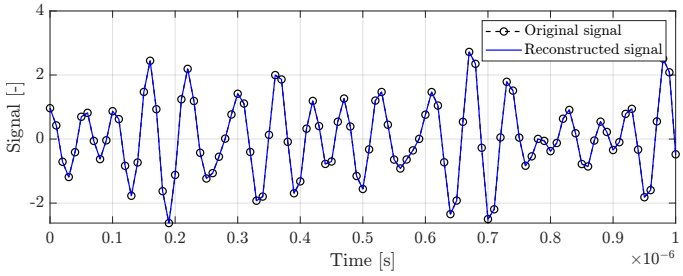

Figure A.4: Original and reconstructed signals without spectral leakage

A.3 Sum of equal frequency waves

Taking the sum of two waves with identical frequencies and different phase leads to a new single wave of same frequency but different phase and amplitude given below:

$$\begin{aligned} Ae^{j(\omega t+\phi_A)} + Be^{j(\omega t+\phi_B)} &= e^{j\omega t}\left(Ae^{j\phi_A} + Be^{j\phi_B}\right) \\ &= e^{j\omega t}[A\cos(\phi_A) + jA\sin(\phi_A) + B\cos(\phi_B) + jB\sin(\phi_B)] \\ &= e^{j\omega t}[A\cos(\phi_A) + B\cos(\phi_B) + j(A\sin(\phi_A) + B\sin(\phi_B))] \\ &= e^{j\omega t} \cdot \sqrt{[A\cos(\phi_A) + B\cos(\phi_B)]^2 + [A\sin(\phi_A) + B\sin(\phi_B)]^2} \\ &\cdot e^{j\cdot\tan^{-1}\left[\frac{A\sin(\phi_A)+B\sin(\phi_B)}{A\cos(\phi_A)+B\cos(\phi_B)}\right]} \\ &= \sqrt{[A\cos(\phi_A) + B\cos(\phi_B)]^2 + [A\sin(\phi_A) + B\sin(\phi_B)]^2} \\ &\cdot e^{j\left(\omega t+\tan^{-1}\left[\frac{A\sin(\phi_A)+B\sin(\phi_B)}{A\cos(\phi_A)+B\cos(\phi_B)}\right]\right)} \end{aligned} \tag{A.3}$$

Figure 3.13 shows the Doppler spectra for both modelling approaches when the phase of all waves for the 'low' level approach is set to zero. This results in a near perfect match of the spectra.

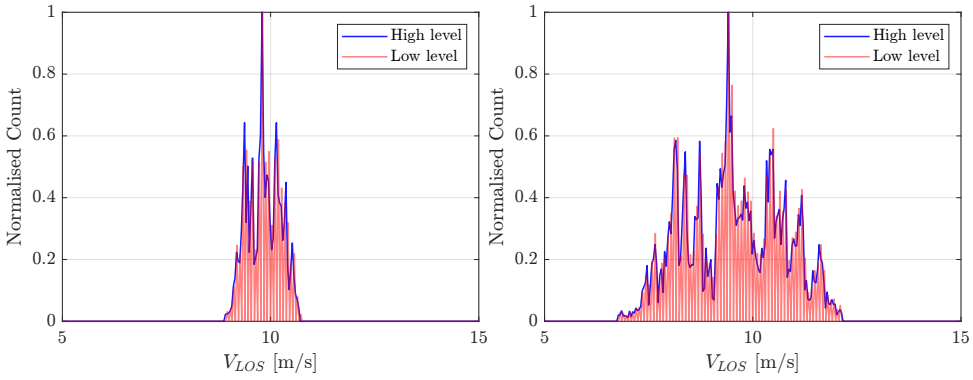

(a) TI = 0.1. (b) TI = 0.3.

Figure A.5: Doppler spectra comparison for turbulent wind fields (U_∞ = 10 m s^{-1}). No phase effects.

A.4 Distance measurement from phase

The algorithm below shows the procedure applied to recover useful information from the phase. First of all in line 3, the distance is obtained form the phase in radians and the line-of-sight velocity of a specific bin n. The distance corresponding to a phase of 2π is then computed in line 4. This corresponds to the ranges at which the phase repeats and can range from a few meters (3.3 m at V_{LOS} = 35 m s^{-1}) to just above a hundred meters (116.3 m at V_{LOS} = 1 m s^{-1}). Lines 5 and 6, show the criteria used to determine if the distance information is reliable or not. δ is the distance from the focal point that gives the measured

amplitude of the bin in question. The condition that $d > 2\delta$ ensures that the phase does not repeat too quickly. An example of this is shown on Figure A.6 where point p_1 is the original point. If the signal wavelength is such that $d < 2\delta$, the next point is p_2 and as it has a higher computed intensity, it will be incorrectly selected. However, if the signal wavelength is such that $d > 2\delta$, then next point is p_3, which has a lower computed intensity and p_1 will be correctly selected. Therefore, if the condition is met, the potential point locations are computed in line 7 and the correct point is selected line 9. The process is then repeated over all bins.

Algorithm 1 Phase Recovery

1: **Inputs:** Phase ϕ, Amplitude A, Line-of-sight velocities V_{LOS}, Weighting function $\mathbf{I}$
2: **for all** bins n **do**
3: Convert phase to distance estimate using $r_n = \phi_n \frac{c\lambda}{8\pi V_{LOS_n}}$
4: Compute distance corresponding to wavelength $d = r_n(\phi_n = 2\pi)$
5: Compute $\delta = \mathbf{I}^{-1}(A_n)$
6: **if** $d > 2\delta$ **then**
7: Compute potential distances with $r_n + Nd$ in relevant range around focal point.
8: Calculate value of intensity at $\mathbf{I}(r_n + Nd)$.
9: Find $N_{max} = \max \mathbf{I}(r_n + Nd)$
10: **return** $r_n + N_{max} d$
11: **end if**
12: **end for**

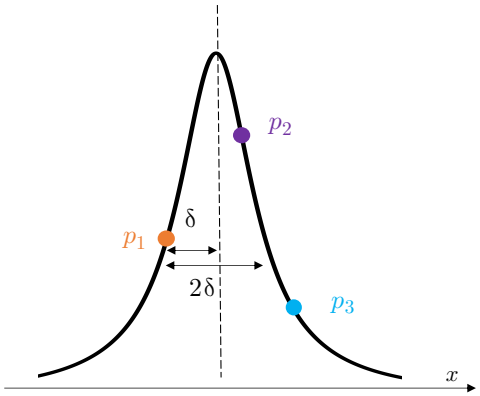

Figure A.6: Lorentzian and point spacing

B

Appendix

B.1 Streamwise scan additional plots

B.1.1 Example of focal point determination

Figure B.1 shows the line-of-sight velocity field measured by the lidar around vortex L_2. The lidar is placed at ($x = 1.38D, y = -0.59D$) and focus the beam downstream, in x direction. This image is then constructed by varying both beam focus range and lidar azimuth angle to obtain several measurements in both x and y. The x location of the vortex is estimated from the region where the velocity peaks of V_{LOS} are found to be the largest in magnitude. This is therefore found to be near $x = 1.52D$ for vortex L_2. The scanning is then continued in y direction only but for a fixed x location. The analysis of the vortex velocity profile can then be performed on the y direction scan measurements.

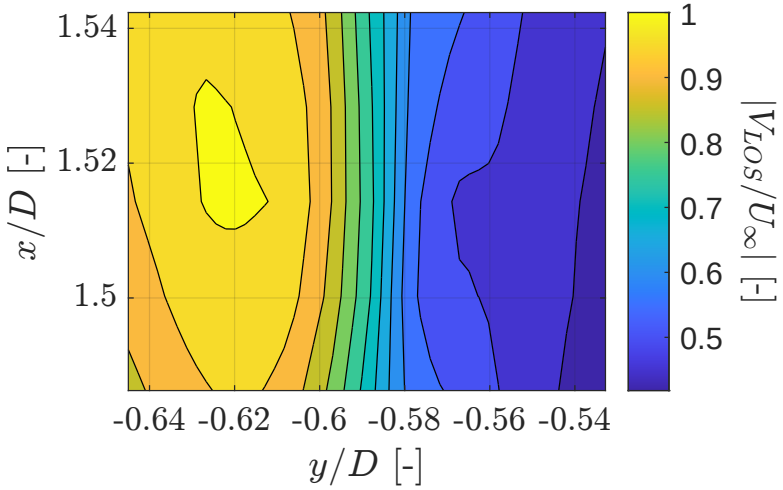

Figure B.1: 2D contour of V_{LOS} measurements around vortex L_2

B.1.2 LOS and measurement volume effects

Figure B.2 shows the differences in core location and radii estimates when incorporating measurement volume effects. The lidar is placed at ($x = 1.38D, y = -0.59D$) and scans in y at fixed distances x downstream. The Rayleigh length is varied base on $z_r(R) = \lambda R^2/(\pi a_0^2)$ (see Equation 2.16), estimated as 24 mm for the ZephIR CW lidar [44]. Differences in both core location and core radius estimates appear to be very small. However, it these discrepancies are most definitely higher for the last vortices, L_4 to L_6. This is expected as the Rayleigh length increases with the square of the measurement range and therefore creates a greater measurement volume damping effect at these locations.

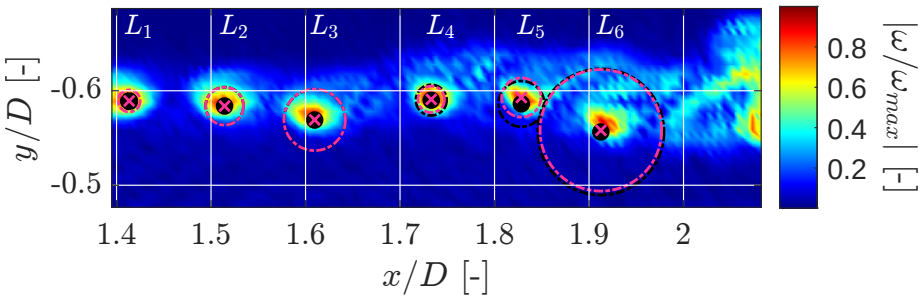

Figure B.2: Vortex detection on streamwise scan with range dependent Rayleigh length effects (pink). Standard case with fixed Rayleigh length shown as reference (black).

B.1.3 Streamwise scan: Doppler spectra outputs side

The Doppler spectrum outputs obtained from the scan of each vortex in the streamwise configuration setup are presented below, together with the estimate of the core location given by the black dashed line. This is shown below for the left and right sides of the wake.

Left side

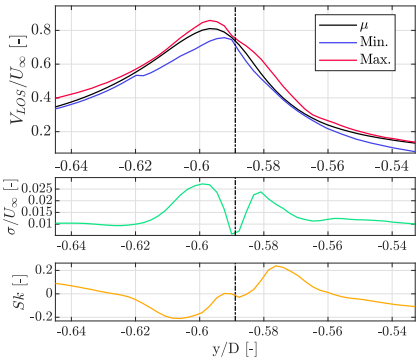

(a) Vortex L_1

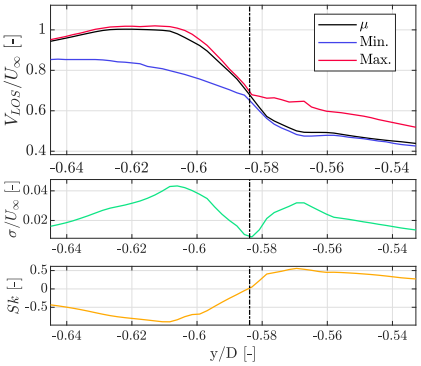

(b) Vortex L_2

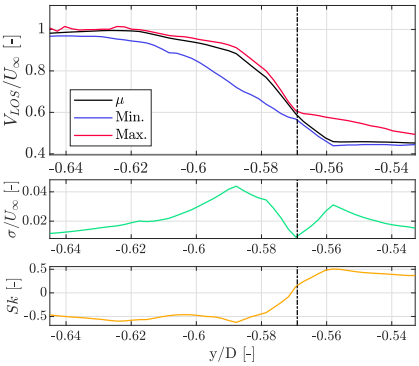

(c) Vortex L_3

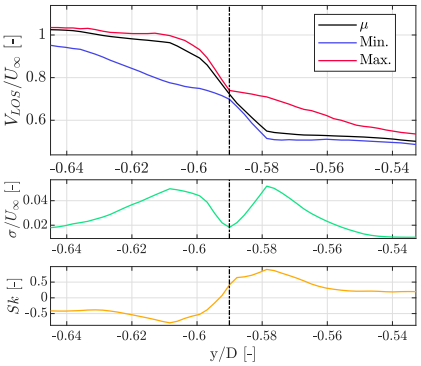

(d) Vortex L_4

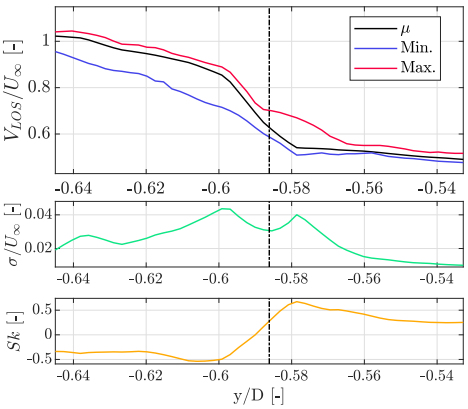

(e) Vortex L_5

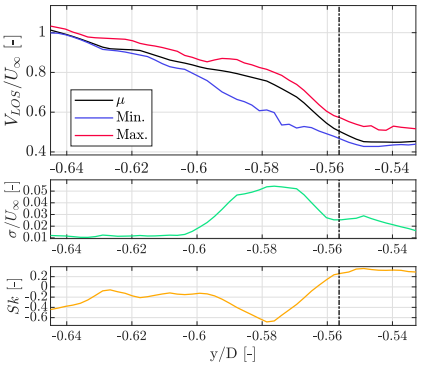

(f) Vortex L_6

Figure B.3: Doppler spectrum outputs for left side tip vortices. Dashed line shows estimated core location.

Right side

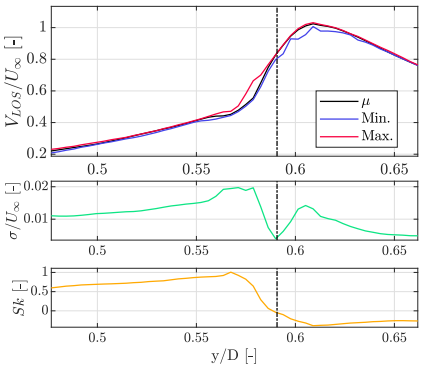

(a) Vortex R_1

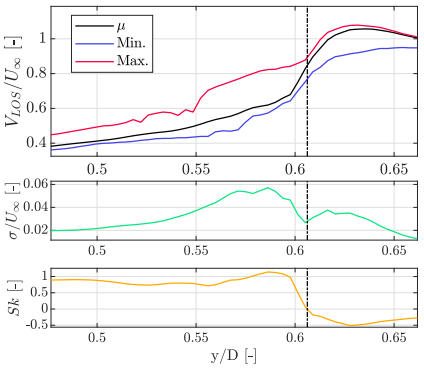

(b) Vortex R_2

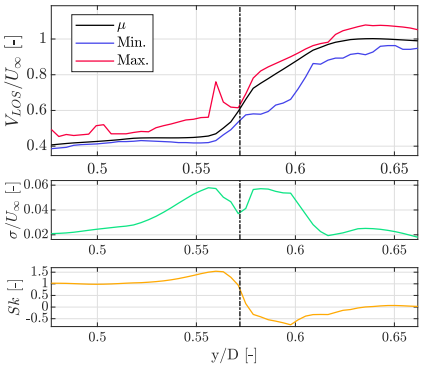

(c) Vortex R_3

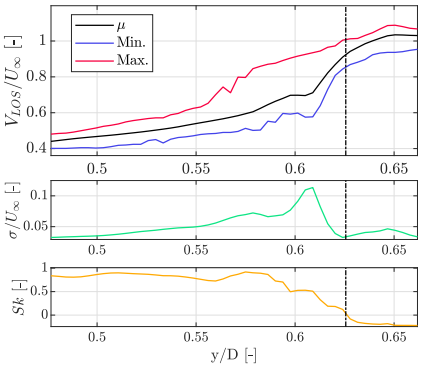

(d) Vortex R_4

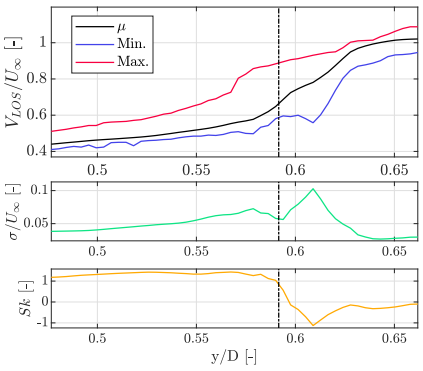

(e) Vortex R_5

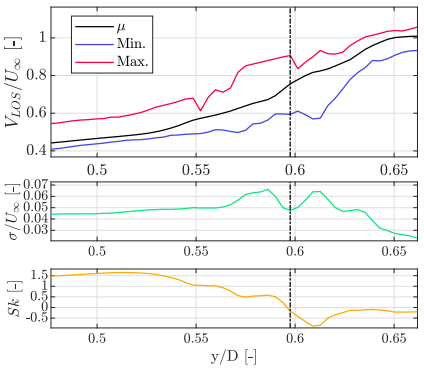

(f) Vortex R_6

Figure B.4: Doppler spectrum outputs for right side tip vortices. Dashed line shows estimated core location.